nature communications

Article

https://doi.org/10.1038/s41467-026-74248-w

# Bioresorbable electrochemical sensors for continuous deep-tissue lactate monitoring in critical care

Received: 23 March 2026

Accepted: 20 May 2026

Published online: 10 June 2026

Check for updates

A list of authors and their affiliations appears at the end of the paper

Lactate is a key metabolite and prognostic biomarker, reflecting oxygen delivery, cellular demand, and mitochondrial function. Current clinical lactate monitoring, however, relies on intermittent blood sampling, limiting localized interrogation, dynamic tracking and early intervention in critical care. Here, we report a bioresorbable and flexible electrochemical sensor for continuous deep-tissue lactate monitoring. By leveraging a previously unreported enzyme-assisted proton-intercalation mechanism, we establish a unique electrochemical sensing interface that enables high-performance lactate detection entirely with biodegradable materials. Integrated with a wireless module, the device enables in vivo real-time recording with excellent sensitivity and stable operation over clinically relevant timescales (> 10 days), without requiring secondary surgeries for device retrieval. The sensor robustly captures organ-specific lactate dynamics during hypoxia and epileptic seizures. Notably, we identify that increases in pericardial lactate precede systemic changes detected by conventional monitoring in septic shock, providing a prominent marker for early warning and timely intervention. Pericardial lactate-guided treatment markedly improves hemodynamic stability and prevents septic shock within the monitoring window. This work enables paradigm-shifting strategies for bioresorbable, implantable sensors that monitor vital metabolites in real time, supporting early diagnosis, guided intervention and improved outcomes in intensive care.

Lactate is a central metabolite that functions not only as a by-product of anaerobic glycolysis but also an indispensable energy substrate and versatile signaling molecule, playing critical roles in tumor proliferation, neural plasticity, immune regulation, and a range of other physiological processes[1–3]. Under pathophysiological conditions, elevated lactate levels are widely regarded as an early and robust indicator, with concentrations correlating closely with disease severity, trajectory, and clinical outcome[4,5]. Importantly, hyperlactatemia may arise not only from oxygen deficiency but also from impaired oxygen extraction and mitochondrial dysfunction, thus lactate serves as a clinically actionable biomarker that integrates information on oxygen supply, cellular demand, and mitochondrial competence, offering critical prognostic insights beyond the realm of simple oxygen debt[6].

The clinical value of lactate monitoring has been extensively documented in critical care, particularly for rapidly progressing and high-mortality conditions such as ischemia and sepsis[7,8]. Sepsis alone affects millions of individuals worldwide each year and is associated with mortality rates of approximately 17–33%, making early identification and prompt treatment in the initial hours after onset critical[9]. Blood lactate concentrations not only serve as a key diagnostic and prognostic biomarker but also guide therapeutic interventions[10], and even modest improvements in lactate clearance correlate with a significant reduction in adverse outcomes[11]. These findings have

e-mail: pengjiang301@126.com; shirley_star@163.com; xingzhelbt@163.com; lanyin@tsinghua.edu.cn

prompted international guidelines to incorporate routine blood lactate measurement as a core component of standard management protocols in perioperative monitoring and intensive care settings[9,12]. However, localized lactate elevations in major organs (e.g., heart, brain) could be more sensitive than systemic changes, even when hemodynamics remain stable[13,14]. Given the narrow window for effective intervention in critical care, the ability to rapidly detect and respond to these localized lactate levels can be decisive in preventing irreversible organ failure[15], highlighting the urgent need for direct, real-time monitoring in deep tissues, where the earliest and most prognostically relevant metabolic changes occur.

Current clinical lactate monitoring relies mainly on intermittent blood sampling, providing only discrete systemic measurements and failing to capture rapid lactate dynamics and organ-specific microcirculatory dysfunction[16]. Microdialysis can provide continuous and localized metabolic information at the implantation site, but its temporal resolution is limited by diffusion, and the technique requires complex device setup, calibration, and maintenance[17]. Optical approaches, including colorimetric and fluorescence-based methods, enable non-invasive continuous monitoring but are constrained by shallow tissue penetration and the high cost and complexity of advanced detection systems[16,18,19]. Recent progress in electrochemical biosensors has demonstrated great promise for real-time lactate detection with improved sensitivity and miniaturization[20,21]. Nevertheless, most existing platforms rely on wearable or microneedle-based systems that sample lactate from sweat or subcutaneous tissues[22,23]. These approaches do not provide direct access to deep tissues, limiting timely and accurate assessment of tissue perfusion and metabolic status in major organs, which is critical in intensive care. While a few studies have reported implantable sensors for short-term lactate monitoring in the brain and kidney[24–26], stable measurements over perioperative or critical care relevant timescales have yet to be achieved. Moreover, these sensors are constructed from non-degradable materials, necessitating surgical retrieval and thereby increasing the risk of infection, tissue damage, and procedural complications[27–29]. Although electrochemically triggered disintegration strategies have been proposed, these systems still rely on conventional non-degradable components (e.g., platinum (Pt), silver/silver chloride (Ag/AgCl), polyurethane, and poly(3,4-ethylenedioxythiophene): polystyrene sulfonate (PEDOT:PSS)), potentially leading to residual material retention[26]. In addition, the high overpotentials required to induce device breakdown may pose safety risks to electrically sensitive organs such as the brain and heart. Overall, developing high-performance electrochemical sensors composed entirely of bioresorbable materials remains a long-standing challenge. Innovative materials strategies are therefore critical, as existing devices remain constrained by non-degradable components, signal drift, limited operational lifetimes, and reliance on complex compensation circuitry[30,31]. These limitations highlight a critical gap in current lactate monitoring technologies and underscore the urgent need for robust implantable platforms based on fully bioresorbable materials that enable real-time lactate sensing in deep tissues. Such systems should operate over clinically relevant timeframes in intensive care settings, thereby supporting clinical decision-making, tracking disease progression, and enabling timely therapeutic intervention.

Here, we present a fully bioresorbable, flexible, electrochemical lactate sensor with a soft, wet-adhesive hydrogel substrate, designed for postoperative monitoring in critical care (Fig. 1a, b). Integrated with a Bluetooth module, the device enables wireless, real-time monitoring of lactate in deep tissues under critical pathological conditions, while its bioresorbable design eliminates the need for surgical retrieval, thereby reducing risks associated with secondary procedures. The primary advances of this work include: (1) the development of biodegradable sensing electrodes based on molybdenum/molybdenum oxide ($Mo/MoO_x$) that exploit a previously unreported enzyme-assisted proton-intercalation mechanism of $MoO_x$ for lactate signal transduction, addressing the major challenge of constructing electrochemical sensors based entirely on biodegradable components while maintaining long-term operational stability; (2) a biodegradable adhesive hydrogel substrate that forms a soft and durable tissue-device interface, enabling prolonged device immobilization on target organs and effective mitigating motion artifacts; (3) a fully bioresorbable materials platform with robust sensing performance, achieving excellent detection limits, sensitivity and dynamic range, as well as stable in vivo operation over clinically relevant timeframes (>10 days)—a capability rarely achieved even with non-biodegradable lactate sensors; (4) reliable capture dynamic lactate changes across multiple pathological conditions, including in a large-animal model. Notably, the sensor reveals pericardial lactate as a robust early marker of septic shock, preceding conventional parameters such as mean arterial pressure (MAP). We further show that this early-detection capability enables prompt lactate-guided fluid resuscitation (FR), significantly improving hemodynamic stability and clinical outcomes, highlighting the importance of early diagnosis in guiding timely intervention in sepsis management; and (5) material strategies that can be extended to other analytes (e.g., glucose, nitric oxide, sodium and potassium ions) through appropriate functionalization. Together, these features highlight the potential of biodegradable electrochemical platforms for real-time monitoring of vital biochemical signals, supporting early diagnosis and timely therapeutic intervention in critical care.

## Results

### Materials and design of the bioresorbable lactate sensor

The schematic illustration of the bioresorbable and flexible lactate sensor is given in Fig. 1a, b, with detailed fabrication procedures described in Supplementary Fig. 1. We first achieve a biodegradable, adhesive double-network hydrogel composed of poly (ethylene glycol) diacrylate (PEGDA) and peptide as the device substrate, enabling durable sensor-tissue immobilization for stable, long-term monitoring. The hydrogel is fabricated via drop-casting and crosslinking under UV light, enabling mechanical compliance and stable integration with soft tissues. Specifically, PEGDA forms the covalently crosslinked primary network via photoinitiation with Irgacure 2959, providing elasticity and toughness, whereas peptide form a secondary, low-modulus network through physical crosslinking. The Fourier transform infrared spectroscopy (FTIR) results suggest that hydrogen bonding and Michael addition reactions could have been involved in the PEGDA/peptide hydrogel (Supplementary Fig. 2). SEM images reveal that the double-network PEGDA/peptide hydrogel exhibits a denser and less porous structure compared to the single-network PEGDA hydrogel (Supplementary Fig. 3), resulting in a slightly lower swelling rate (Supplementary Fig. 4a), which helps maintain a more stable adhesive-tissue interface[32]. To further mitigate hydrogel swelling and its impact on sensing, the hydrogel thickness is limited to ~200 μm, and a chitosan/genipin bridging polymer can be applied to the backside of the hydrogel, which effectively reduces swelling (Supplementary Fig. 5). As peptide typically degrades rapidly[33], increasing the peptide content accelerates the overall biodegradation of the hydrogel (Supplementary Fig. 4b). Strong adhesion at the hydrogel/tissue interface can be achieved by the application of bridging agents, consisting of chitosan and genipin (Fig. 1c). The adhesion mechanism is mainly attributed to the tough dual network hydrogel matrix enabling energy dissipation, and interface bonding (non-covalent and covalent bonds) (Supplementary Fig. 6), similar to mechanisms proposed in previous reports[34–36]. Notably, the introduction of genipin in the bridging agent is expected to covalently crosslink amine groups on the hydrogel, chitosan, and tissue surfaces, thereby enhancing linkage stability in the presence of lysozyme which is abundant in biological systems[37], and ensuring a robust, intact adhesion interface in aqueous environments.

A key challenge in developing fully bioresorbable electrochemical sensors lies in simultaneously achieving electrochemical activity, operational stability and complete biodegradability. Here we introduce biodegradable electrodes based on Mo/$MoO_x$ that exploit a previously unreported enzyme-assisted proton-intercalation mechanism in $MoO_x$ for signal transduction (Fig. 1a and Supplementary Fig. 7a), establishing a unique electrochemical interface for high-performance lactate sensing in fully bioresorbable biosensors. Molybdenum (Mo) is selected for its favorable biocompatibility, high electrical conductivity and slower dissolution rate compared with more reactive biodegradable metals such as magnesium or zinc[38]. Surface modification to molybdenum oxide ($MoO_x$) further enhances electrochemical stability under physiological conditions by introducing a dynamic metal/oxide equilibrium, while simultaneously preserving biodegradability[30]. Building on these features, we propose a fully bioresorbable electrode configuration in which Mo/$MoO_x$ functions as the working (WE), counter (CE), and reference (RE) electrodes, enabling stable and continuous lactate sensing without relying on non-degradable components such as Ag/AgCl RE and Pt CE. Conventional lactate sensors typically employ amperometric detection based on non-degradable working electrodes, which lack intrinsic lactate sensitivity and therefore depend on enzymatic reactions with cofactors or electron mediators to generate a signal[39]. For example, carbon electrodes are not responsive to lactate (Supplementary Fig. 7b) and therefore rely on lactate dehydrogenase (LDH)-catalyzed reactions coupled with nicotinamide adenine dinucleotide ($NADH/NAD^+$) redox processes at oxidation potentials to enable lactate sensing (Supplementary Fig. 7c, d). In contrast, by leveraging the intrinsic proton-intercalation capability of $MoO_x$[40], we uncover its electrochemical responsiveness to lactate under reduction potentials without relying on $NADH/NAD^+$ redox reactions or an additional electron mediator layer (Supplementary Fig. 7e, f), thereby eliminating the need for high oxidation overpotentials and improving electrode stability while reducing susceptibility to interference from readily oxidizable species. Integration of LDH/$NAD^+$-loaded functionalization layer further amplifies the response current and enhances sensing selectivity by catalyzing lactate conversion to pyruvate with proton generation (Supplementary Fig. 7g, h), thereby conferring desirable anti-interference capability, including tolerance to pH variation (as shown later in Fig. 1l, m and Supplementary Fig. 25). It should be noted that $NAD^+$ is incorporated to catalyze the lactate-to-pyruvate reaction rather than for redox reaction. Raman analysis of the Mo/$MoO_x$ surface before and after amperometric measurements in the presence of lactate indicates proton intercalation, as evidenced by the increased signals associated with hydrogen molybdenum bronze ($H_xMoO_3$) (Supplementary Fig. 7i). Consistently, XPS analysis shows an increase in the relative proportion of $Mo^{5+}$ and $Mo^{4+}$ species compared with $Mo^{6+}$ components (Supplementary Fig. 7j), resulting from proton-intercalation induced valence transition. This unconventional sensing strategy enables sensitive and robust detection of lactate dynamics using entirely biodegradable materials, thereby overcoming key limitations of conventional electrochemical sensors that rely on non-degradable components.

Specifically, to fabricate Mo/$MoO_x$ electrodes, Mo foils (40 μm) are first patterned via precision laser ablation, then subjected to electroanodization and thermal annealing to produce a conformal $MoO_x$ surface layer (~5 μm) (Fig. 1d, and Supplementary Figs. 8–10). The resulting Mo/$MoO_x$ bilayer electrode exhibits low interfacial impedance comparable to pristine Mo (Supplementary Fig. 11), along with a stable open circuit potential showing minimal voltage drift (~ 11 mV) over a 6-day period (Supplementary Fig. 12). LDH and $NAD^+$-loaded polyvinyl alcohol (PVA)/chitosan hydrogel is applied to the silane-functionalized Mo/$MoO_x$ WE, with genipin serving as the crosslinker. Genipin effectively crosslinks amine groups, thereby enhancing the immobilization of LDH and $NAD^+$ and promoting a stable connection between the enzyme and the electrode surface. Compared with hydrogels without genipin, PVA/chitosan hydrogels with genipin crosslinker show substantially reduced $NAD^+$ release after immersion in PBS at 37 °C for 5 days (Supplementary Fig. 13). Integrating Mo/$MoO_x$ electrodes with the biodegradable adhesive hydrogel substrate confers the sensor excellent mechanical compliance and flexibility (Fig. 1e). Mo/$MoO_x$ electrodes are embedded within the hydrogel matrix, with the CE and RE encapsulated by a top hydrogel layer to prevent direct contact with target tissues, thereby enhancing electrode stability and minimizing potential effects of the applied electric field on surrounding tissues during lactate sensing.

## Characterization of the bioresorbable lactate sensor

We first assess the mechanical properties of PEGDA/peptide hydrogels. The incorporation of peptide (5 g/L) and genipin enables the formation of a cross-linked PEGDA/peptide double-network hydrogel, enhancing tensile strength (1100 ± 64 kPa) and toughness (5.8 ± 0.5 $MJ/m^3$) compared to the single-network PEGDA hydrogel (Fig. 1f, Supplementary Figs. 14, 15). The adhesion capability of PEGDA/peptide hydrogels is evaluated by applying them to either hydrogel or wet tissue surfaces, using 180° peeling and lap shear tests (Supplementary Fig. 16). Bridging polymer (chitosan) and genipin are introduced at the interface to enhance adhesion (Supplementary Fig. 17). In comparison, genipin or chitosan alone yields adhesion energies far lower than when used together (234.3 ± 30.0 $J/m^2$) (Supplementary Fig. 18). Adhesion energy is also sensitive to the concentration and molecular weight of chitosan, with 2.0 g/L of medium-viscosity chitosan (190–310 kDa) achieving the highest adhesion (Supplementary Fig. 19). Moreover, increasing peptide concentration from 0 to 5 g/L enhances adhesion energy between two hydrogels (Fig. 1g). However, further increases in peptide content reduce adhesion performance, likely due to competing effects: while peptide enhance interfacial bonding by improving cohesive energy and increasing the availability of active bonding sites, excessive loading may limit the diffusion of bridging polymer, ultimately diminishing overall adhesion energy, a phenomenon observed in other hydrogel-based adhesive systems[41]. Furthermore, the PEGDA/peptide hydrogel exhibits desirable adhesion to wet tissues such as porcine skin, heart, intestine and liver (Fig. 1h). Prolonged adhesion in wet environments is also achieved using the PEGDA/peptide hydrogel. For example, adhesion to another hydrogel layer or heart tissue is sustained for up to 30 and 15 days when soaked in deionized (DI) water at 25 °C, respectively, with adhesion energy gradually decreasing over time (Supplementary Fig. 20, Fig. 1i). Adhesion to porcine intestine even persists for up to 6 months when soaked in simulated human intestinal fluid (SIF) (Supplementary Movie 1), indicating desirable wet adhesion characteristics of PEGDA/peptide hydrogels with biological tissues (Supplementary Table 1). PEGDA/peptide hydrogels also exhibit excellent bursting pressure, comparable to that of commercial biomedical adhesives (Supplementary Fig. 21), and can effectively seal perforated porcine stomach tissue under water injection (Supplementary Movie 2). These results collectively demonstrate that the PEGDA/peptide hydrogel substrate establishes robust adhesion to tissues in aqueous environments, enabling stable immobilization of the lactate sensor on target tissues for long-term monitoring.

Lactate detection is based on amperometry using a three-electrodes configuration, with the bioresorbable Mo/$MoO_x$ electrodes serving as the WE, CE, and RE. The sensor demonstrates linear response at physiologically relevant concentrations up to 30 mM, with a sensitivity of 0.78 ± 0.10 μA/mM in the range of 0–8 mM, a detection limit of 0.1 mM (Fig. 1j, k, Supplementary Fig. 22, 23). This favorable detection limit and linear range enable sensitive lactate detection across concentration ranges relevant to pathological conditions[42]. Moreover, the sensor can detect as little as 0.5 μL of a 1 mM lactate solution (Supplementary Fig. 24). At this volume, the solution only partially contacts the electrode surface, yet a current response is observed. Increasing the solution volume enlarges the electrode

https://doi.org/10.1038/s41467-026-74248-w

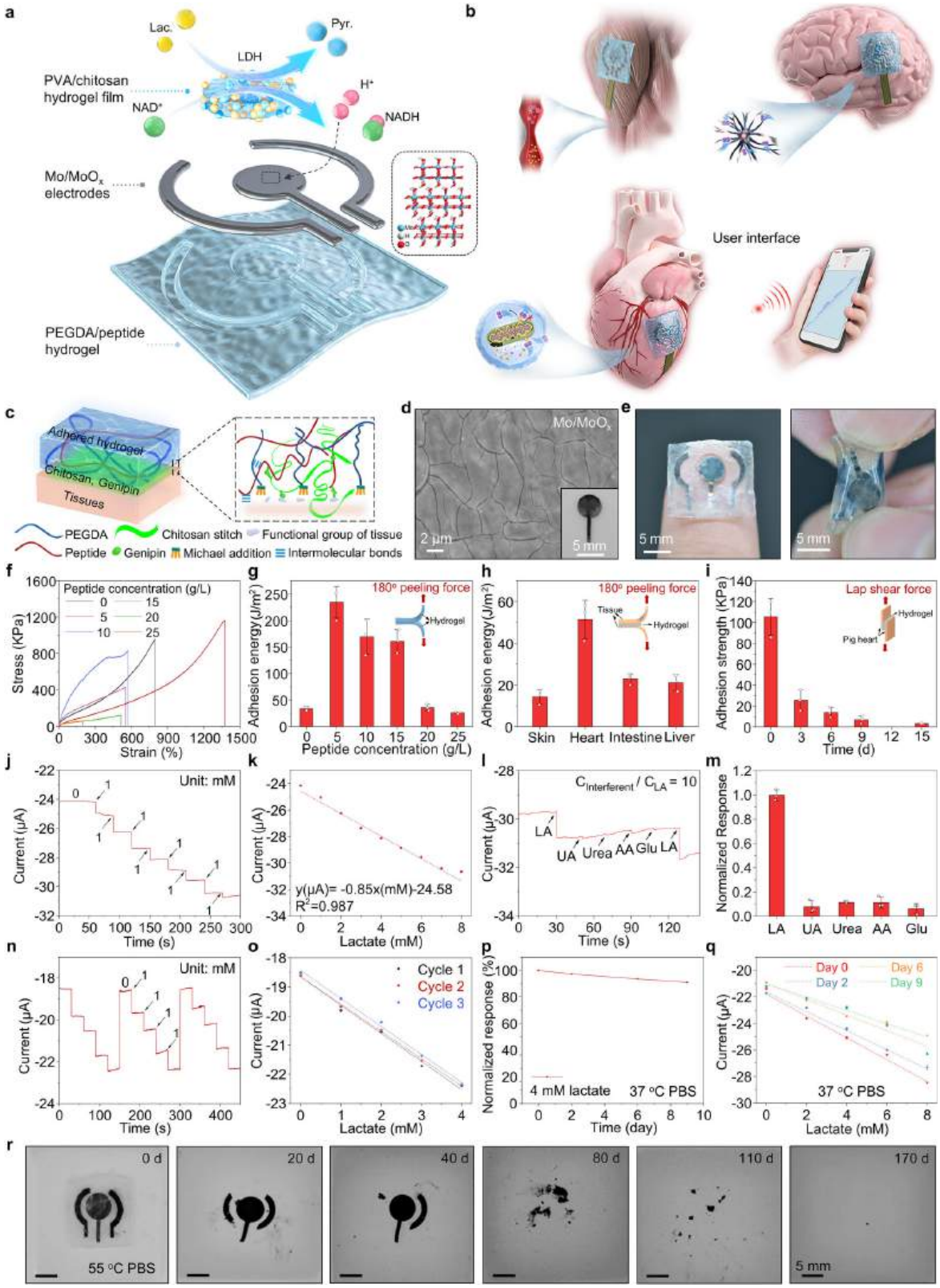


contact area, resulting in a higher current response. A solution volume of 10 μL achieves complete wetting of the electrode surface, while further increases in volume do not produce additional enhancement of the current response. During in vivo monitoring, the surrounding tissue fluids are generally sufficient to fully cover the entire sensing electrode. Furthermore, the selectivity of the lactate sensor is evaluated against common interfering species in biological systems, including uric acid (UA), urea, ascorbic acid (AA), and glucose (Glu) (Fig. 1l). Upon the addition of potential interfering species at concentrations tenfold higher (10 mM) than that of lactate (1 mM), the sensor's response to lactate remains at least 83.6% greater than to interferent chemicals (Fig. 1m). Under physiological conditions, the concentrations of glucose, uric acid, urea, and ascorbic acid generally remain below 10 mM (Supplementary Table 2). Accordingly, the

**Fig. 1 | Bioresorbable lactate sensor with adhesive hydrogel for wireless deep-tissue monitoring during hypoxia, epilepsy, and septic shock. a** Schematic of the sensor composed of a PEGDA/peptide hydrogel, Mo/$MoO_x$ electrodes, and a LDH/$NAD^+$-loaded PVA/chitosan film for lactate detection via enzyme-assisted proton-intercalation. **b** The sensor, implanted at the limb, brain or heart, continuously detects localized lactate under impaired perfusion, excessive oxygen consumption and mitochondrial dysfunction, with wireless data transmission. **c** Adhesion mechanism involves dual-network dissipation, chitosan bridging, intermolecular interactions, Michael addition, and genipin-mediated crosslinking. **d** SEM image of the surface $MoO_x$ layer of the working electrode (WE). Inset: optical image of the Mo/$MoO_x$ WE. **e** Photograph of the bioresorbable sensor. **f** Tensile stress-strain curves of PEGDA/peptide hydrogels with different peptide concentrations. **g** Adhesion energy between hydrogels with different peptide concentrations, with chitosan and genipin as the bridging agents. **h** Adhesion energy of hydrogels adhered to tissues, with bridging agents. **i** Adhesion strength of hydrogels adhered to pig heart over varying soaking time in deionized (DI) water at 25 °C, with bridging agents. **j** Time-dependent current response of the bioresorbable sensor at different lactate concentrations (0–8 mM, −0.65 V.) **k** Calibration curve: linear relationship between currents and lactate concentrations (0–8 mM). **l** Selectivity measurement: response with the additions of interfering chemicals (10 mM) and lactate (1 mM). LA lactate, UA uric acid, AA ascorbic acid, Glu glucose. **m** Normalized current responses of the bioresorbable sensor, with the addition of lactate and interfering chemicals. **n** Cyclic tests of the currents of the bioresorbable sensor. **o** Linear relationship between currents and lactate concentrations from 0 to 4 mM for three consecutive cycles. **p** Chronic stability of the sensor in response to 4 mM lactate in PBS at 37 °C. **q** Stability of the sensor: linear relationship between currents and lactate concentrations from day 0 to day 9 in PBS at 37 °C. **r** Accelerated dissolution process of the bioresorbable sensor after soaking in PBS at 55 °C. In (**d**, **f**–**q**), $n = 3$ independent samples. In (**g**–**i**, **m**, **q**), data are presented as mean ± SD.

concentrations of potential interfering species used in the selectivity tests are selected to match or exceed their physiological levels. The sensor also exhibits a small current response to $H^+$ concentration changes (Supplementary Fig. 25a), with the current response to $H^+$ (1 mM) being less than 20% of that to lactate (1 mM) (Supplementary Fig. 25b). Under pathological conditions such as hypoxia, epilepsy and sepsis, reported pH deviation in the brain tissue and blood, from physiological conditions (pH 7.4) are relatively modest (0.03–1.2 units) and are often associated with lactate accumulation[43–45]. These results indicate that limited pH changes encountered during in vivo monitoring do not significantly interfere with lactate measurements. In addition, the cyclic tests of the current response of the sensor show stable and fast responses to varying lactate concentrations, with comparable detection sensitivity (Fig. 1n, o). The mechanical robustness of the bioresorbable sensor is further evaluated by monitoring the current response after repeated bending. Following 300 bending cycles, the detection sensitivity shows negligible reduction (Supplementary Fig. 26).

We also investigate the effects of temperature. As shown in Supplementary Fig. 27, varying the temperature from 30 °C to 40 °C does not result in significant changes in the measured lactate signal (1 mM), and the detection sensitivity of the sensors remains comparable at 30 °C and 40 °C. As shown later, temperature variations during in vivo measurements remain within a narrow range (32–34 °C), indicating that the limited temperature fluctuations encountered during in vivo monitoring contribute negligibly to the recorded signals. As mechanical motion such as the heartbeat, can affect recorded signals, noise levels induced by motion are also evaluated using an in vitro heart-motion simulator. Compared with adhesive hydrogels incorporating chitosan/genipin bridging polymers, non-adhesive hydrogel interfaces exhibit greater motion artifacts (Supplementary Fig. 28a). These results indicate that the adhesive hydrogel interface plays an important role in achieving an intimate device-tissue interface and mitigating motion-induced signal artifacts. Supplementary Fig. 28b demonstrates that the current response of the sensor remains essentially unchanged after 10,000 cycles of vibration, indicating that the genipin-crosslinked PVA/chitosan layer provides stable coupling to the electrode and effective enzyme immobilization, thereby minimizing potential motion-induced detachment of the functional layer and supporting robust lactate sensing. Moreover, motion artifacts may also be further reduced to improve signal specificity in future studies by referencing the recorded signals to those obtained from an additional sensor without LDH/$NAD^+$ functionalization (Supplementary Fig. 28c, d).

Furthermore, sensing stability is also investigated. We examine the potential detachment of the sensor due to gradual degradation of the adhesive hydrogel. Although adhesion energy decreases over time, the sensor remains attached to heart tissue for up to 10 days when soaked in deionized water at 25 °C (Supplementary Fig. 29a). These findings are consistent with the measured adhesion strength between the hydrogel and heart tissue over the soaking period (Fig. 1i), suggesting that slow hydrogel degradation does not appreciably compromise sensor attachment during the monitoring period (~10 days), thereby enabling an intimate device-tissue interface for prolonged sensing on target organs. In PBS at 37 °C, the bioresorbable sensor retains over 90% of its initial lactate response (4 mM) after 9 days (Fig. 1p), indicating stable sensing performance with minimal signal drift. Although the detection sensitivity gradually decreases overtime, a desirable linear relationship between lactate concentration and response current is maintained throughout this period (Fig. 1q). Upon exposure to hypothetically high concentrations of interfering chemicals (tenfold that of lactate), the sensor's anti-interference properties remain relatively stable over 6 days, while responses to UA and AA gradually increase by day 9, likely due to progressive degradation of the enzyme-containing PVA/chitosan hydrogel film (Supplementary Fig. 29b). These results demonstrate desirable operational stability and robustness, indicating the device is suitable for long-term lactate monitoring over clinically relevant time frames (~7 days)[46–48]. Strategies to further extend the functional lifetime include engineering the enzyme to enhance intrinsic stability and prolong catalytic activity; optimizing surface modifications to increase electrode hydrophilicity and strengthen interfacial adhesion between the LDH/$NAD^+$-loaded PVA/chitosan hydrogel and the electrode, thereby mitigating potential delamination and activity loss over the long term; and incorporating zwitterionic hydrogels to stabilize enzyme molecules through multiple non-covalent interactions, reducing denaturation and biofouling in vivo[49–51]. After soaking the sensor in phosphate-buffered saline (PBS) (pH 7.4) solution at 55 °C, the sensor gradually disintegrated into small fragments and completely degrades within 170 days (Fig. 1r). Additional experiments are performed to evaluate potential impact of tissue depth on sensor sensitivity by using pork samples of varying thickness to simulate different tissue depths. As shown in Supplementary Fig. 30, the detection sensitivity remains comparable across tissue depths ranging from 0 to 10 mm. Because the sensor is designed to electrically connected percutaneously to external circuitry, the implantation depth does not significantly influence sensor performance.

Collectively, the identification of a previously unreported LDH-assisted proton-intercalation mechanism in Mo/$MoO_x$ electrodes establishes a unique electrochemical interface, enabling high-performance lactate sensing using entirely biodegradable materials. Compared with reported implantable lactate sensors involve non-degradable materials, the bioresorbable device offers an excellent detection limit (0.1 mM) and sensitivity (0.78 μA/mM), a broad detection range (0–30 mM), and an extended in vivo operational lifetime (> 10 days) as demonstrated below—a capability rarely achieved even

by non-bioresorbable sensors—while its full biodegradability eliminates the need for retrieval surgery (Supplementary Table 3). As lactate concentrations may exceed 10 mM under pathological conditions[42], and the first 7 days after surgery represents a critical window marked by the peak risk of infection and the onset of early sepsis[46–48], the characteristics of the bioresorbable lactate sensor allow robust and continuous deep-tissue monitoring over clinically relevant timescales in critical care.

In contrast to conventional electrochemical sensing electrodes such as carbon-based materials, Mo/$MoO_x$ electrodes uniquely combine robust lactate sensing capability with intrinsic bioresorbability. These advantages arise from two key features. First, surface oxidation of Mo forms a $MoO_x$ layer that establishes a dynamic metal/oxide equilibrium, enhancing electrochemical stability while maintaining biodegradability, and thereby eliminating the reliance of nondegradable electrode materials. Second, the layered structure and multiple oxidation states of $MoO_x$ enable interactions with lactate through a proton-intercalation pathway. Carbon-based electrodes, although chemically stable and widely used for electrochemical sensing due to their large effective surface area and facile chemical functionalization, are intrinsically insensitive to lactate and therefore require signal transduction through enzymatic reactions together with electron mediators or redox cofactors such as Prussian Blue and NADH/$NAD^+$[39]. In contrast, Mo/$MoO_x$ directly transduces lactate signals through LDH/$NAD^+$ assisted proton-coupled processes, enabling sensitive detection without relying on additional electron mediator layers. Despite being biodegradable, Mo/$MoO_x$ electrodes maintain sufficient electrochemical stability for in vivo operation over prolonged timeframes (> 10 days) as shown below. Nevertheless, Mo/$MoO_x$ electrodes exhibit a narrower stable potential window than carbon electrodes owing to their degradable nature, and exposure to high oxidation potentials can compromise electrode stability, necessitating the incorporation of an additional coating layer. Moreover, the baseline noise characteristics of Mo/$MoO_x$ electrodes remain comparable to those of carbon electrodes (< 1%). Furthermore, beyond lactate sensing, this materials platform can be readily extended to other analytes with appropriate functionalization— including alternative metabolites such as glucose, gasotransmitters such as nitric oxide via amperometric detection, and ions such as sodium and potassium via potentiometric sensing (Supplementary Fig. 31)—highlighting the versatility of Mo/$MoO_x$ as a prominent class of biodegradable electrochemical electrodes.

## Lactate monitoring under hypoxic conditions

Hypoxic conditions, such as those resulting from cardiac or cerebral ischemia, are clinically critical as they can rapidly induce tissue injury and organ dysfunction. Lactate represents an essential metabolite of anaerobic metabolism, which can serve as a timely indicator of impaired oxygen delivery[1]. We first evaluate the sensing performance of the bioresorbable lactate sensor implanted in the pericardial cavity of New Zealand rabbits under systemic hypoxia, induced by varying the ratio of inspired $O_2$ using an $O_2/N_2$ gas mixture (Fig. 2a). Owing to the beating motion of the heart, cardiac measurements are subject to more pronounced motion artifacts than those from the dura mater or thigh muscle. The noise characteristics of cardiac measurements are therefore examined. Although high-frequency noise is present due to heart motion and the level of motion artifacts depends on the intimacy of the device-tissue interface and the beating amplitude (Supplementary Fig. 32a), combined low-pass filtering and LOWESS smoothing effectively attenuate motion artifacts and reveal the underlying lactate dynamics (Supplementary Fig. 32b). The filtered signal also shows that signal drift due to heart motion is not significant within the 40-min window. As the inspired $O_2$ ratio decreases, the recorded current exhibits a rapid increase, suggesting elevated pericardial lactate levels consistent with hypoxic conditions (Fig. 2b). In contrast, standard clinical monitoring parameters such as pulse rate (PR) and blood oxygen saturation ($SpO_2$) obtained by a commercial pulse oximeter (Berry BM1000A) remain unchanged over the short observation period (Fig. 2b), indicating delayed response. The variation in lactate levels upon reducing inspired $O_2$ ratios is calculated using the device's calibration curve (Fig. 1k), which agrees well with simultaneous intermittent measurements of pericardial effusion by a commercial lactate sensor (YST-1) (Fig. 2c, Supplementary Fig. 33). Similarly, real-time tracking of pericardial lactate dynamics during varying respiration rates (RR) via a ventilator is achieved (Fig. 2d). A decrease in RR induces systemic hypoxia, reflected by an increase in lactate current that subsequently declines upon RR recovery (Fig. 2e). Over this longer monitoring window compared to the varying $O_2$ ratio experiments, systemic hypoxia is also evident from reductions in PR and $SpO_2$ (Fig. 2e). Lactate variations measured by the bioresorbable sensor during varying RR closely align with those obtained using a commercial lactate sensor (Fig. 2f), while providing the added advantage of continuous monitoring. Blood lactate sampled from the auricular artery and measured with a conventional blood gas analyzer (300-G) shows negligible increase with decreasing RR, indicating that systemic blood lactate variations are less pronounced than those detected directly at the heart by the sensor (Supplementary Fig. 34a). Together, these results demonstrate that the bioresorbable electrochemical sensor can rapidly and reliably detect systemic hypoxic conditions in deep tissues in real time.

We then investigate continuous lactate monitoring under conditions of local hypoxia, which are commonly encountered in cerebral infarction, limb ischemia, and myocardial infarction. We develop a customized wireless control circuit to enable remote data recording. As shown in Fig. 3a, the wireless module integrates a potentiostat, a Bluetooth system-on-chip and a rechargeable battery. The circuit module measures 2.23 × 1.76 × 0.83 $cm^3$, and weights 1.2 g (Fig. 3b), and connects percutaneously to the implantable lactate sensor, secured to the external surface of the animal with surgical tape (Fig. 3c). In practice, the connection can be routed through drains, which are commonly placed temporarily after brain or cardiac procedures to evacuate blood and effusion[52]. The input current of the wireless module ranges from 200 nA to 200 μA. Supplementary Table 4 shows that the received signal strength indication (RSSI) decreases with increasing transmission distance. No packet loss is observed within a distance range of 5 m, indicating stable and reliable communication. We further perform a power budget analysis of the wireless module. With sensing and Bluetooth communication fully active, the sensing board consumes approximately 17 mW, whereas power consumption is near 0.9 mW when the system is inactive. The resulting daily energy consumption is ~0.408 Wh under continuous operation, or ~0.056 Wh for intermittent measurements (2 h of sensing per day), corresponding to approximately 0.9 and 6.6 days of operation, respectively, from a 100 mAh lithium battery with a nominal voltage of 3.7 V. Together, these evaluations demonstrate a robust and deployable wireless system.

We perform real-time lactate sensing on the dura matter, limb and heart under acute local hypoxic conditions. Specifically, intracranial epidural lactate is monitored using the bioresorbable sensor placed on the dura mater of pigs during cerebral ischemia induced by clamping of common carotid arteries (Fig. 3d). Following unilateral and bilateral clamping, the evolution of the lactate current response is successfully captured in real time, indicating increases in lactate levels from baseline to mild and severe ischemia (Fig. 3e, f). Transient current spikes are observed upon artery clamping, likely arising from local vessel movements; nevertheless, the current returns to stable levels shortly thereafter. In contrast, PR and $SpO_2$ remain unchanged during the monitoring window (Fig. 3e), as these systemic parameters are less sensitive to early microcirculatory dysfunction than direct lactate measurements on the dura matter (Fig. 3g). In addition, tissue fluids are sampled from the dura mater and analyzed using a commercial

https://doi.org/10.1038/s41467-026-74248-w

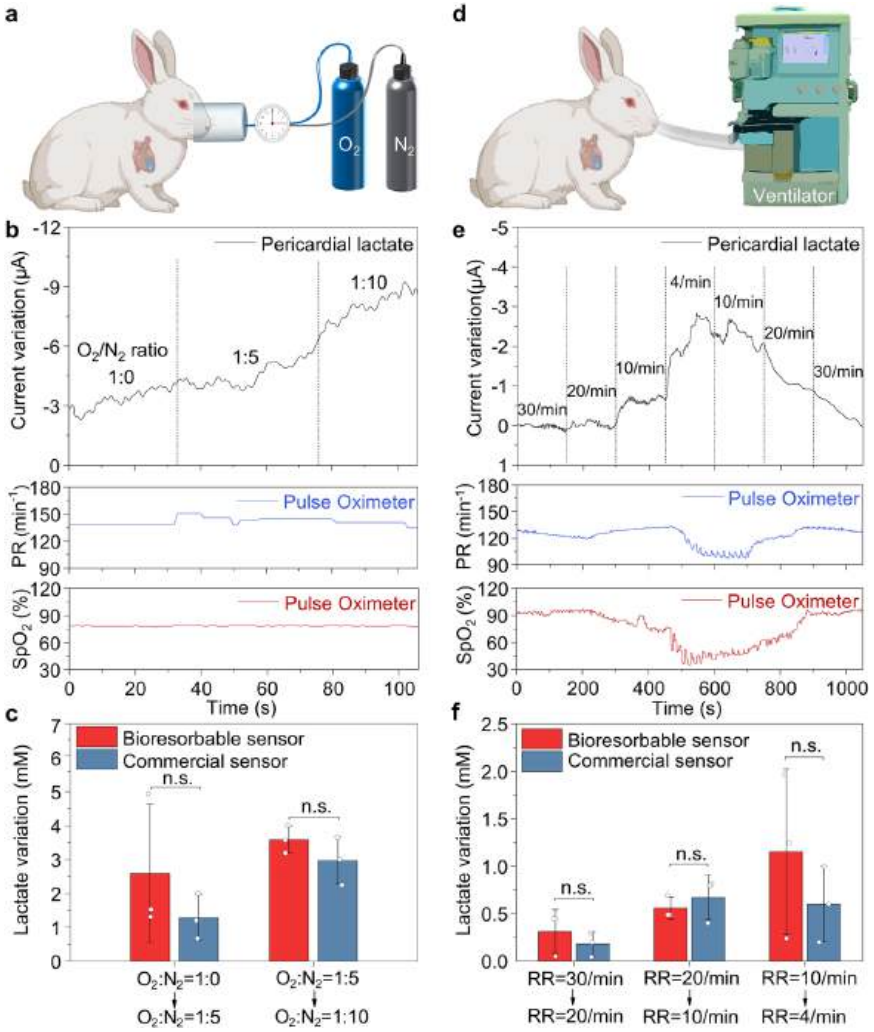


**Fig. 2 | Real-time monitoring of pericardial lactate concentration using the bioresorbable sensor at the heart of New Zealand rabbits under conditions of systemic hypoxia. a** Schematic illustration of continuous detection of pericardial lactate of rabbits exposed to varying ratios of inspired $O_2$ using a mixture of $O_2$ and $N_2$ gas. **b** Real-time current response of pericardial lactate and corresponding recorded pulse rate (PR) and blood oxygenation ($SpO_2$) measured by the commercial pulse oximeter (Berry BM1000A) under different ratios of inspired $O_2$. **c** Comparison of lactate variation measured by the bioresorbable lactate sensor and the commercial lactate sensor (YST-1) under different ratios of inspired $O_2$. **d** Schematic illustration of continuous detection of pericardial lactate of rabbits with varying respiration rates (RR). **e** Real-time current response of pericardial lactate and corresponding recorded PR and $SpO_2$ of rabbits with varying RR. **f** Comparison of lactate variation measured by the bioresorbable lactate sensor and the commercial lactate sensor (YST-1) with varying RR. In (**b**, **c**, **e**–**f**), $n = 3$ independent experiments. In (**c**, **f**), the statistical analysis is based on the t-test of independent samples (two-sided). n.s. (not significant). Data are presented as mean ± SD. Part of (**a**, **b**) are created in BioRender. Sheng, X. (2026) https://BioRender.com/xd1lxc5.

lactate sensor, yielding results consistent with those obtained using the biodegradable sensors (Supplementary Fig. 35a).

A similar trend in lactate dynamics is observed when measuring muscle lactate with the bioresorbable sensor in the hind limb muscles of New Zealand rabbits during local ischemia induced by thigh ligation (Fig. 3h). The results indicate that lactate levels rise under both mild and severe ischemia but decline following ligation release and reperfusion (Fig. 3i, j). It is noted that transient current spikes present in the figure are associated with the thigh ligation procedure. The signal rapidly returns to a stable level thereafter, revealing the underlying lactate dynamics across different stages of ischemia. Meanwhile, recorded PR and $SpO_2$ stay unchanged throughout the procedure (Fig. 3i), and lactate changes during ischemia and reperfusion are significantly more pronounced than changes in PR and $SpO_2$ (Fig. 3k). Tissue fluids of the thigh muscles are analyzed using a commercial lactate sensor, yielding results consistent with those obtained using the biodegradable sensors (Supplementary Fig. 35b).

Moreover, real-time lactate levels are monitored during myocardial ischemia induced by clamping the anterior descending artery and second diagonal branch (Fig. 3l). The data shows that signal drift from motion is not significant, whereas a pronounced increase in lactate signal is observed upon the onset of myocardial ischemia (Fig. 3m, n), with changes much more pronounced than those in PR and $SpO_2$ (Fig. 3o). An additional real-time measurement is shown in Supplementary Fig. 36. Although motion-related effects and the magnitude of lactate elevation vary across animals and with ischemia severity, both measurements show a consistent trend of markedly increased lactate signals during myocardial ischemia (Fig. 3m, n and Supplementary Fig. 36). In addition, tissue fluids are sampled from the heart and analyzed using a commercial lactate sensor, yielding results consistent with those obtained using the biodegradable sensors (Supplementary Fig. 35c). Such elevation in blood lactate in the auricular artery is also confirmed by conventional intermittent measurement using a blood gas analyzer during ischemia (Supplementary Fig. 34b).

Furthermore, we evaluate the sensor's long-term performance in limb muscle to assess its feasibility for continuous monitoring over clinically relevant timeframes for intensive care (Fig. 3p). Owing to the adhesive hydrogel and robust performance of Mo/$MoO_x$ electrodes, the sensor remains securely immobilized in the tissue and maintains a consistent current response to hindlimb ischemia, thereby enabling reliable lactate tracking on days 0, 4, 7, and 10 (Fig. 3q, Supplementary Fig. 37a). We also evaluate the calibration curve of the lactate sensor after 11 days of implantation (Fig. 3r). Although the sensitivity of the sensor within the 0–8 mM range decreases by ~30%, likely owing to gradual degradation of the enzyme components, the sensor retains a desirable linear response. Notably, this level of in vivo stability surpasses that of previously reported implantable lactate sensors and has rarely been achieved even in non-degradable systems. Nevertheless, absolute in vivo quantification would benefit from periodic recalibration. These results indicate robust monitoring performance over a clinically relevant time frame. Furthermore, we quantitatively assess in vivo signal drift and performance degradation after multi-day implantation in the thigh muscle. These results indicate that baseline drift is not significant, remaining within ~0.1 μA over a 12-min period (Supplementary Fig. 37b) and within ~1 μA and ~4 μA over 7 and 11 days, respectively (Supplementary Fig. 37c). This demonstrates that baseline drift manifests as slow and minor variations. By contrast, lactate changes under pathological conditions, such as hypoxia, produce rapid and substantially larger current responses over short timescales (tens of seconds)—for example, ~0.7–2.1 μA for rabbit hindlimb ischemia, ~1.4–4.6 μA for rabbit myocardial ischemia and ~0.3 μA for rat hindlimb ischemia (Fig. 3j, n, q). The pronounced difference in magnitude and timescale enables differentiation of pathological lactate signals from baseline drift. Collectively, these results demonstrate that the bioresorbable lactate sensor enables real-time lactate monitoring in deep tissues during hypoxic conditions. Notably, under localized hypoxia, lactate levels provide a more sensitive and clinically actionable biomarker for early hypoxia detection compared to conventional systemic parameters like PR and $SpO_2$. The sensor's stable functionality permits continuous lactate monitoring over timeframes relevant to critical care, offering valuable data for postoperative surveillance and treatment optimization, without requiring additional surgical removal.

## Lactate monitoring during epilepsy

In addition to reduced oxygen perfusion, excessive oxygen consumption is another factor that can lead to anaerobic metabolism and therefore elevated lactate levels. Epilepsy is one such scenario, where intense neural activity drives substantial oxygen demand[53]. We investigate lactate dynamics on the cortical surface to track changes throughout the progression of epilepsy. As shown schematically in Fig. 4a, penicillin G is injected via syringe into the hippocampus of New Zealand rabbits to induce motor epilepsy by increasing neuronal excitability[54], while tungsten wires are inserted for electrophysiological recording. The lactate sensor is placed on the cortical surface to continuously monitor cerebrospinal fluid (CSF) lactate dynamics (Supplementary Fig. 38). Interestingly, lactate levels rise continuously following penicillin G injection, progressing through to epileptoid tremor (Fig. 4b). This increase is likely driven by excessive neural activity that consumes substantial glucose and oxygen[55], thereby elevating lactate. By contrast, $SpO_2$ remains unchanged and PR shows only a slight decrease, reflecting their markedly lower sensitivity compared with localized CSF lactate measurements (Fig. 4b, c). In addition, tissue fluids are sampled from the cortical surface and analyzed using a commercial lactate sensor, yielding results consistent with those obtained using the biodegradable sensors (Supplementary Fig. 35d). Fig. 4d displays simultaneous recorded data of local field potentials (LFPs) in the hippocampus, power spectral density (PSD) and lactate concentrations. These data indicate that penicillin G injection elicits intensified LFP oscillations, followed by a marked increase in CSF lactate recorded by the sensor. Statistically, lactate levels in the hippocampal region significantly rise ~6 s after the onset of LFP oscillations (Fig. 4e), suggesting neural activity triggers elevated lactate. These results indicate that the bioresorbable sensor enables real-time interrogation of CSF lactate under conditions of high oxygen consumption, offering critical insights into the largely unexplored metabolic dynamics of pathological states such as epilepsy.

## Lactate monitoring during septic shock

Although post-surgical patients are at high risk of sepsis, a life-threatening condition arising from infection, timely recognition and intervention can substantially improve outcomes[56]. Mitochondrial dysfunction often occurs during sepsis even under normal perfusion, impairing aerobic respiration and causing elevated lactate levels[57–59]. Consequently, lactate serves as a critical marker for sepsis management[59]. However, current clinical lactate measurements rely on discrete blood sampling, which prevents real-time monitoring of lactate dynamics and limits early diagnosis. Continuous monitoring of lactate in deep tissues under sepsis-related pathological conditions has not yet been explored. Using the bioresorbable lactate sensor, we investigate lactate dynamics on the heart, muscle, and subcutaneous tissue during septic shock. As shown schematically in Fig. 5a, lipopolysaccharide (LPS) is injected via syringe into the auricular vein of New Zealand rabbits to induce septic shock. By 35 min, MAP decreases by more than 25% (Fig. 5b), and blood lactate exceeds 2 mM (Supplementary Fig. 39a) by 40 min, indicating the occurrence of septic shock[60,61]. Three lactate sensors are placed in the pericardial cavity, thigh muscle, and subcutaneous tissue respectively to continuously monitor tissue lactate levels and identify the sites with the greatest variation. Interestingly, the results indicate that lactate rises markedly and consistently in the pericardial cavity than in muscle or subcutaneous tissue following LPS injection (Fig. 5b, c). This is likely due to the higher metabolic demand of the heart, which may render it more susceptible to pathological conditions. Continuous monitoring also demonstrates that pericardial lactate rises are more pronounced than blood lactate measured by intermittent sampling at the early stage (20 min) (Fig. 5b, Supplementary Fig. 39a). By contrast, conventional clinical parameters, such as heart rate (HR), $SpO_2$, and temperature, remain almost unchanged during progression, highlighting their lower sensitivity compared with localized pericardial lactate measurements (Fig. 5b, c). Although response time to LPS injection varies among animals, significant drops in MAP ( < 75% of baseline) consistently lag behind significant rises in pericardial lactate (> 125% of baseline, Fig. 5d). Moreover, we investigate sepsis experiments with more frequent blood lactate sampling to assess the potential correlation between sensor current and blood lactate levels. As shown in Supplementary Fig. 40a, although the magnitude of lactate elevation varies across animals, the trend is consistent: pericardial lactate rises rapidly and markedly following LPS administration, whereas blood lactate increases more slowly and with less pronounced changes. Pericardial lactate can therefore be leveraged for early diagnosis, as blood lactate measurements are typically obtained at much lower temporal resolution. Furthermore, a linear correlation is observed between the normalized variation of lactate current and blood lactate concentration, with a Pearson coefficient of 0.82 (Supplementary Fig. 40b). These findings indicate that localized pericardial lactate changes precede significant systemic alterations, and can serve as a sensitive marker for sepsis monitoring, offering a critical window for timely intervention to substantially reduce complications and improve prognosis.

To demonstrate the importance of early diagnosis enabled by continuous lactate monitoring, treatment is administered at either the early sign of rising pericardial lactate (lactate >125% of baseline) or upon a significant decrease of MAP (MAP < 75% of baseline), using FR via the auricular vein with normal saline, a standard clinical

https://doi.org/10.1038/s41467-026-74248-w

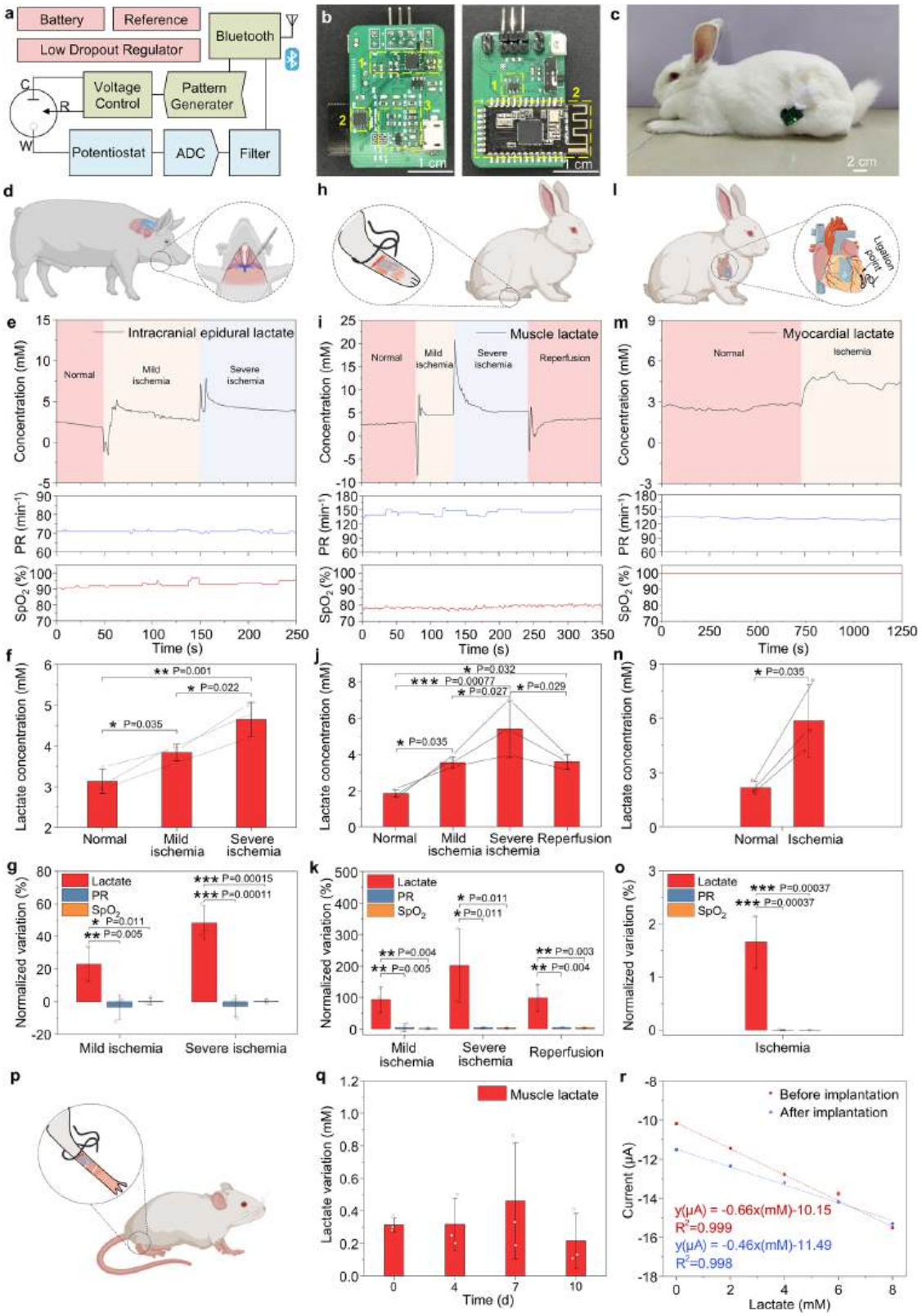


intervention. Untreated septic shock serves as a reference, with MAP remaining low in the absence of FR (Fig. 5b, g). When FR is initiated upon a marked drop in MAP, blood lactate has already exceeded 2 mM (Supplementary Fig. 39b), indicating the onset of septic shock, and restoration of normal MAP takes 7 ± 3 min (Fig. 5e, g). In contrast, early FR guided by a > 25% increase in pericardial lactate stabilizes MAP and prevents the occurrence of septic shock within the monitoring window (Fig. 5f, g). Correspondingly, the lowest MAP during progression is significantly greater with pericardial lactate-guided FR than with MAP-guided FR or no FR (Fig. 5h), indicating significantly improved hemodynamics. These results suggest that continuous pericardial lactate monitoring enables early detection of pathological changes and timely

**Fig. 3 | Real-time lactate monitoring using the wireless bioresorbable lactate sensor on the dura mater of Landrace pig, in the thigh muscles and at the heart of New Zealand rabbits, and in the thigh muscles of Sprague Dawley (SD) rats under local hypoxia. a** Schematic of wireless transmission system (ADC, analog-to-digital converter). **b** Back side of the module: 1-Potentiostat; 2-Digital to Analog Converter (DAC); 3-Low Dropout Regulator. Front side: 1-Reference; 2-Voltage Control, ADC, Filter and Bluetooth. **c** Photograph of the rabbit with sensor implanted in the thigh. **d** Lactate detection on the dura mater of pigs during cerebral ischemia. **e** Intracranial epidural lactate, PR and $SpO_2$ during cerebral ischemia. **f** Lactate under normal, mild and severe ischemia. **g** Normalized variations of lactate, PR and $SpO_2$ under mild and severe ischemia. **h**, Schematic of lactate detection in rabbit thigh muscles during the hind limb ischemia. **i** Thigh muscle lactate, PR and $SpO_2$ during hind limb ischemia. **j** Lactate concentration in the thigh muscles under normal, mild, severe ischemia and reperfusion. **k** Normalized variations of lactate, PR and $SpO_2$ under mild, severe ischemia and reperfusion. **l** Schematic of lactate detection at the heart of rabbits during myocardial ischemia. **m** Pericardial lactate, PR and $SpO_2$ during myocardial ischemia. **n** Lactate concentration at the heart of rabbits under normal and ischemia conditions. **o** Normalized variations of lactate, PR and $SpO_2$ under myocardial ischemia. **p** Schematic of continuous detection of lactate in the thigh muscle of SD rats during hind limb ischemia induced by ligating the thigh. **q** Comparison of lactate variation from normal to ischemia on days 0, 4, 7, and 10. **r** Calibration curve: linear relationship between the current and lactate concentration before and after implantation of 11 days. In (**e**–**g**, **i**–**k**, **m**–**o**, **q**, **r**), $n = 3$ independent experiments. In (**f**, **g**, **j**, **k**, **o**), the statistical analysis is based on the one-way ANOVA and LSD (least significant difference) post-hoc comparison (two-sided). In (**n**), the statistical analysis is based on the t-test of independent samples (two-sided). $^{*}P < 0.05$, $^{**}P < 0.01$, $^{***}P < 0.001$. Data are presented as mean ± SD. Part of (**d**, **h**, **l**, **p**) are created in BioRender. Sheng, X. (2026) https://BioRender.com/xd1lxc5.

intervention, thereby preventing progression to severe outcomes such as septic shock, which is expected to significantly improve prognosis[62]. Moreover, we also evaluate sensor performance to detect delayed septic shock. Following sensor implantation at the heart of rabbits, septic shock is induced via LPS injection on day 3, corresponding to the potential timeframe of post-surgical inflammation[48]. A significant increase in lactate levels is captured (Fig. 5i), consistent with the LPS-induced lactate rise observed in acute experiments, demonstrating the bioresorbable sensor's capability for continuous pericardial lactate monitoring to guide early detection and treatment of septic shock.

### In vivo bioresorbability and biocompatibility

The lactate sensor is implanted onto the myocardial surface of SD rats, and its bioresorption is monitored using high resolution digital radiography (DR). Although the hydrogel substrate has low visibility in DR images, the results reveal gradual degradation of the Mo/$MoO_x$ electrodes over 32 weeks (Fig. 6a). Optical images confirm the degradation process of the sensor (Fig. 6b), showing that the Mo/$MoO_x$ electrodes dissolves and reduces shapes over 32 weeks, while the hydrogel substrate is fully degraded by 16 weeks. Interestingly, the hydrogel substrate remains adhesive 4 weeks postoperatively, which enables long-term immobilization of the sensor at the target site (Supplementary Fig. 41). Hematoxylin–eosin (HE) staining of myocardial tissues near the sensor implantation site at 16 and 32 weeks postimplantation is comparable to that of the control group, indicating no obvious signs of inflammation (Fig. 6c). Hematology and blood chemistry analyses at 4, 16, and 32 weeks postoperatively show minimal differences compared with controls (Fig. 6d, e). Inductively coupled plasma mass spectrometry (ICP-MS) reveals normal Mo levels in the heart, liver, spleen, lung, and kidney[63], suggesting no appreciable accumulation relative to controls (Fig. 6f). Moreover, surface biofouling can arise from protein adsorption, cell adhesion, or microbial colonization associated with the foreign body response, potentially compromising sensor sensitivity and operational lifetime. In our experiments, following appropriate sterilization of devices prior to surgical procedure, biofouling is not significant during long-term implantation, likely attributable to the biocompatible and hydrophilic properties of the adhesive hydrogel interface, as evidenced by the photographs shown in Fig. 6b and Supplementary Fig. 41 at 4, 16, and 32 weeks post-implantation. These results, together with low signal drift and stable sensor performance observed over a 10-day period (Fig. 3q, r and Supplementary Fig. 37), indicate that biofouling does not significantly affect the functionality of the bioresorbable sensors. This result is also consistent with previous reports showing that adhesive hydrogel interfaces can alleviate fibrous encapsulation by reducing inflammatory cell infiltration at the device-tissue interface[64]. Taken together, these results demonstrate that the bioresorbable lactate sensor exhibits desirable biodegradability and biocompatibility.

## Discussion

We report a fully bioresorbable, flexible, electrochemical lactate sensor capable of continuous deep-tissue monitoring under critical pathological conditions. By leveraging a previously unexplored proton-intercalation mechanism in Mo/$MoO_x$ electrodes, we establish robust lactate sensing using entirely biodegradable materials, thereby overcoming a key limitation of conventional sensors based on non-degradable components. Integrated with a biodegradable adhesive hydrogel, the sensors achieve stable, high-performance lactate detection in deep tissues over clinically relevant timescales (> 10 days), while their bioresorbability eliminates the need for device retrieval. The sensors reliably detect early lactate changes during hypoxia and track lactate dynamics during epileptic seizures. Importantly, continuous pericardial lactate monitoring reveals early lactate elevations that precede systemic hemodynamic changes, providing a prominent marker for timely lactate-guided intervention to avert severe outcomes such as septic shock. These findings demonstrate a transformative approach to real-time, metabolite-guided diagnosis and treatment in critical care. The materials and device strategies are broadly generalizable to other analytes, highlighting the potential of fully bioresorbable electrochemical platforms to advance both biosensing technology and intensive patient care. Future endeavor can focus on interface engineering to further ensure minimal biofouling, including surface functionalization to tune hydrophilicity and charge, incorporation of biomolecular coatings, or drug-eluting layers. For instance, nanoporous electrodes modified with polyethylene glycol (PEG) can reduce biomolecule adhesion and enhance device longevity, while zwitterionic polymer coatings have been shown to decrease biofouling and attenuate immune responses[65–68]. More versatile functionalization strategies for Mo/$MoO_x$ electrodes, enabling expanded potential windows and the interrogation of multiple cytokines, hormones, and neurotransmitters, could further broaden the functional scope. Integration with therapeutic systems, such as microfluidics or electrical stimulation, can enable closed-loop interventions. Together, these advances establish a foundation for biodegradable electrochemical platforms that monitor critical metabolites, providing a powerful tool for early diagnosis, guided therapy, and prognostic assessment in critical care.

## Methods

### Materials

The starting materials included polyethylene glycol diacrylate (PEGDA, weight-averaged molecular mass, MW, 20 kDa) purchased from GuangZhou Tanshtech Co., Ltd., 2-hydroxy-4′-(2-hydroxyethoxy)-2-methyl-propiophe (Irgacure 2959) purchased from Beijing Mreda Technology Co., Ltd., peptide (RADA16, AC-RADARADARADARADA-$NH_2$) purchased from BioAct Peptide Biotechnology LLC., chitosan (medium molecular weight) purchased from Sigma-Aldrich, genipin purchased from Shanghai Meryer Technologies Co., Ltd., bovine

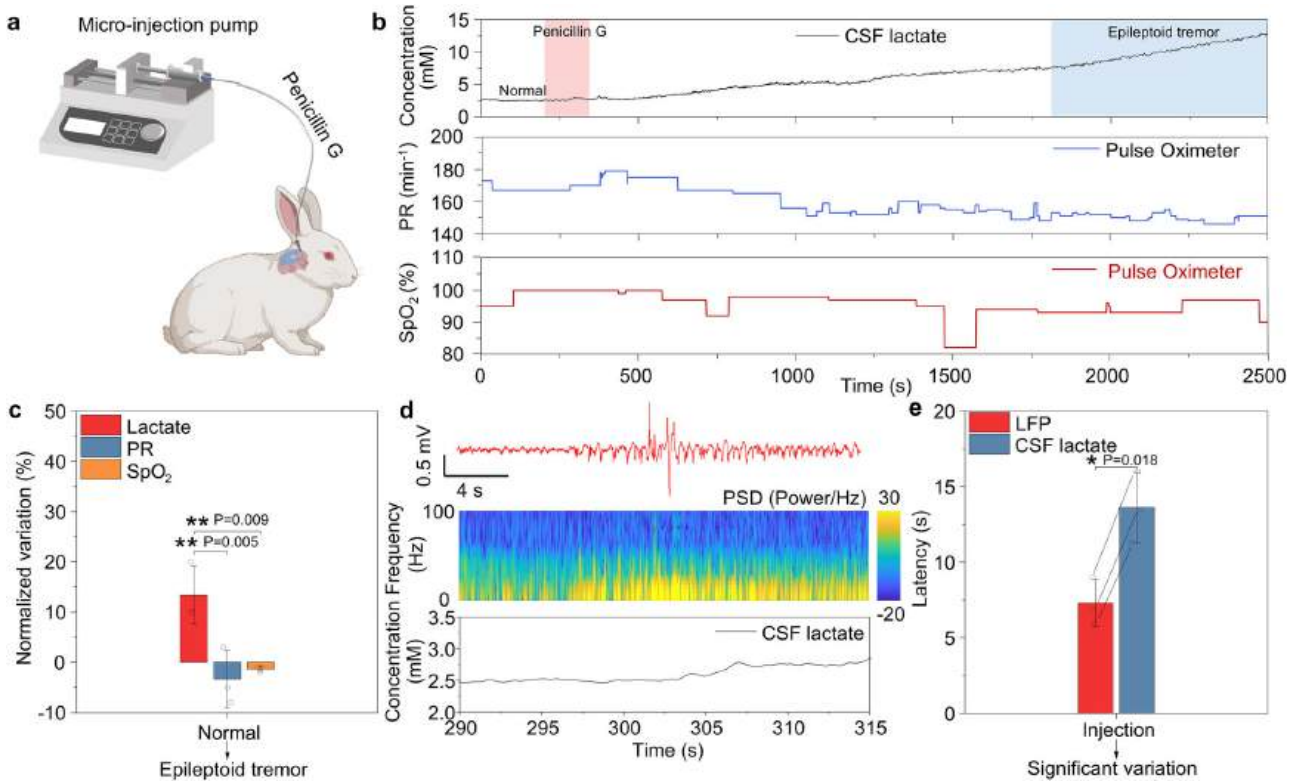


**Fig. 4 | Real-time monitoring of lactate concentration using the bioresorbable sensor on the cortical surface of New Zealand rabbits during epilepsy.** **a** Schematic illustration of continuous detection of cerebrospinal fluid (CSF) lactate on the cortical surface of the rabbit during epilepsy induced by injecting penicillin G. **b** Real-time monitoring of CSF lactate and corresponding recorded PR and $SpO_2$ during epilepsy. **c** Normalized variation of lactate, PR and $SpO_2$ in an epileptoid tremor state relative to the normal conditions. **d** Recorded electrophysiological activities in hippocampus: local field potentials (LFP) trace (top); power spectral density (PSD) of the LFP (middle), and corresponding CSF lactate evolution (bottom). **e** Comparison of the latency time of LFP and CSF lactate between penicillin G injection and symptom onset. Significant variation denotes the transition from the latent to the ictal phase of epilepsy. **b**–**e** $n = 3$ independent experiments. In (**c**), the statistical analysis is based on the one-way ANOVA and LSD (least significant difference) post-hoc comparison (two-sided). In (**e**), the statistical analysis is based on the t-test of independent samples (two-sided). $^{*}P < 0.05$, $^{**}P < 0.01$. Data are presented as mean ± SD. Part of (**a**) is created in BioRender. Sheng, X. (2026) https://BioRender.com/xd1lxc5.

serum albumin (BSA) purchased from Beijing Biodee Biotechnology Co., Ltd., polyvinyl alcohol (PVA, MW, 44.05) purchased from Shanghai Aladdin Biochemical Technology Co., Ltd., lactic dehydrogenase (LDH, from rabbit muscle) purchased from Shanghai yuanye Bio-Technology Co., Ltd., nicotinamide adenine dinucleotide ($NAD^+$) and uric acid (UA) purchased from Tianjin Zancheng Technology, lactate (LA) and glucose (GLU) purchased from Shanghai Titan Scientific Co., Ltd., ascorbic acid (AA) purchased from Sinopharm Chemical Reagent, urea and sodium chloride (NaCl) purchased from Beijing Tongguang Fine Chemicals Co., Ltd., phosphate buffer solution (PBS) (0.01 M, pH 7.2–7.4) purchased from Beijing Solarbio® Life Science Co., Ltd., and MES (pH 4.7) purchased from Hefei BioBomei Biotechnology Co., Ltd. All chemicals were used as received. Commercial materials, including N-butyl-2-cyanoacrylate adhesive (Compont Medical Devices), N-ethyl-2-cyanoacrylate adhesive (Shenzhen Borayer Biotech Co., Ltd.), and Porcine Fibrin Sealant Kit (Guangzhou Bioseal Biotech Co., Ltd.), were used for comparison. Mo foil (30 μm for electrochemical, dissolution and implantation experiments) purchased from Haoxuan Metal Materials.

### Synthesis of PEGDA/peptide bioresorbable hydrogel substrate

PEGDA/peptide hydrogels were synthesized to serve as the adhesive substrate. Specifically, PEGDA-20k (40 wt%), peptide (0–25 g/L), and photo-initiator IRGACURE 2959 (I-2959, 0.036 wt%) were dissolved in PBS, and stirred for 20 min till a clean solution was obtained. After degassing, the precursor solution was placed in a Teflon mold for UV curing (365 nm, 8 mW $cm^{-2}$, 20 min). The bridging polymer chitosan and the coupling reagents genipin were dissolved into MES buffer at 0.02 mg $mL^{-1}$ and 0.01 mg $mL^{-1}$, respectively. The mixture of the bridging polymer and coupling reagents (~500 μL) was applied to the surface of the adhesive hydrogel to promote strong adhesion.

### Fabrication of lactate sensors

The molybdenum (Mo) sheet was laser-cut (LPKF ProtoLaser U4) into the shape of electrodes. Then, the Mo electrodes were polished on SiC (1000 mesh) paper and cleaned with 1 M HCl, followed by ultrasonication for 15 min in ethanol, acetone and deionized (DI) water. The cleaned Mo electrodes were then anodized in a threeelectrode setup: Mo electrode as the working electrode (WE), platinum (Pt) plate as the counter electrode (CE), Ag/AgCl as the reference electrode (RE), and 1 M NaCl as the electrolyte solution. The $Mo/MoO_x$ WE was achieved by cyclic voltammetry (CV) at a scan rate (0.1 V $s^{-1}$) within a potential window (0 to 0.8 V) for 5 cycles. The $Mo/MoO_x$ counter electrode (or reference electrode) was prepared via cyclic voltammetry (CV) over 50 cycles, followed by annealing in air at 500 °C for 3 hours with a heating rate of 5 °C $min^{-1}$. PVA (2 wt%) was dissolved in deionized water and chitosan (0.5 wt%) was dissolved in acetic acid (1 M) with vigorous stirring at 80 °C for 12 hours. To modify the $Mo/MoO_x$ WE, BSA (10 mg $mL^{-1}$), LDH (1 mg $mL^{-1}$), $NAD^+$ (10 mg $mL^{-1}$) and genipin (0.01 mg $mL^{-1}$) were dissolved in PVA solution, which was mixed with the chitosan solution. The mixture was stored in a desiccator to

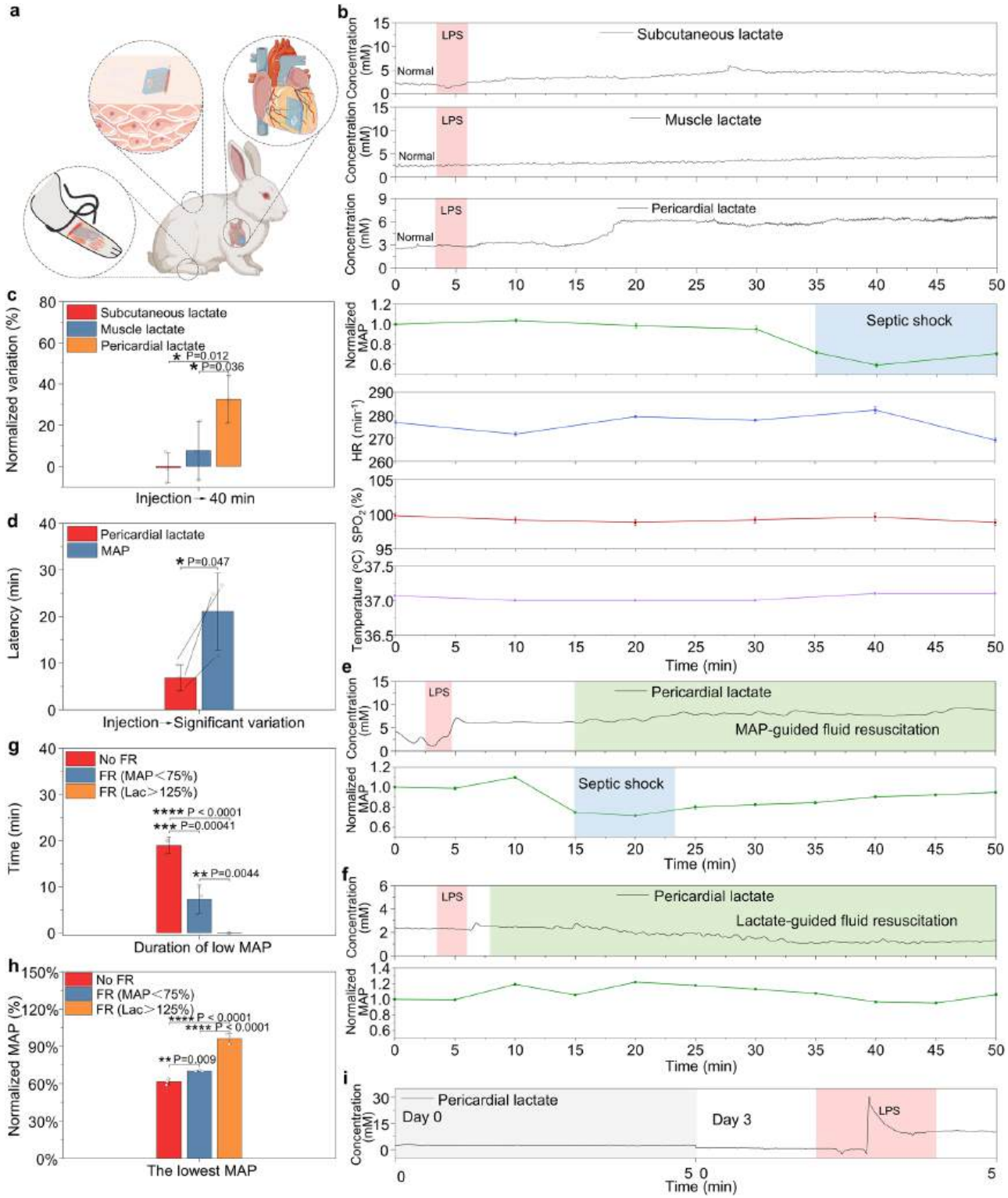


remove bubbles. The Mo/$MoO_x$ WE was treated with UV in the presence of ozone for 30 min, followed by immersion in the 3-aminopropyltriethoxysilane (APTES) for an additional 30 minutes. $MoO_x$ layer react to hydrophilic hydroxyl groups by oxygen radicals produced by the UV. These hydroxyl groups readily form hydrogen bonds with APTES containing amino groups[69]. Finally, the enzyme was immobilized by drop-casting the LDH mixture solution onto the working electrode (WE) and allowing it to dry slowly at 4 °C in a refrigerator. The electrodes were then integrated with the bioresorbable adhesive hydrogel substrate to complete the fabrication of the lactate sensor.

### Wireless control and data transmission system

The wireless miniaturized interface circuit system consists of a current readout link, a biasing link, a power management module, and a wireless Bluetooth module. In the current readout link, the Potentiostat circuit measures the current and converts it into a voltage, which is then digitized by an analog-to-digital converter (ADC). After filtering in

**Fig. 5 | Real-time monitoring of lactate concentration using the bioresorbable sensor during septic shock. a** Schematic illustration of continuous detection of pericardial, muscle, subcutaneous lactate of rabbits during septic shock induced by injecting lipopolysaccharide (LPS). **b** Real-time monitoring results of subcutaneous, muscle, pericardial lactate and corresponding recorded mean arterial pressure (MAP), heart rate (HR), $SpO_2$, temperature of rabbits during septic shock. **c** Normalized variations of subcutaneous, muscle and pericardial lactate at 40 min post-injection relative to the initial state. **d** Comparison of the latency time of pericardial lactate and MAP between LPS injection and significant variation. Significant variation denotes the onset of septic shock, characterized by a marked increase in pericardial lactate (> 25%) or decrease in MAP ( > 25%). **e** Real-time monitoring results of pericardial lactate and corresponding recorded MAP of rabbits during septic shock, with fluid resuscitation (FR) initiated once MAP falls below 75% of baseline. **f** Real-time monitoring results of pericardial lactate and corresponding recorded MAP of rabbits during septic shock, with FR initiated once pericardial lactate exceeds 125% of baseline. **g** Durations of low MAP under no FR, FR (MAP < 75%) and FR (Lac > 125%) conditions during septic shock. **h** The lowest MAP under no FR, FR (MAP < 75%) and FR (Lac > 125%) conditions during septic shock. **i** Recorded pericardial lactate of rabbits on day 0 and day 3 with LPS-induced delayed septic shock. In (**b**–**i**), $n = 3$ independent experiments. In (**c**, **g**, **h**), the statistical analysis is based on the one-way ANOVA (analysis of variance) and LSD (least significant difference) post-hoc comparison (two-sided). In (**d**) the statistical analysis is based on the t-test of independent samples (two-sided). $^{*}P < 0.05$, $^{**}P < 0.01$, $^{***}P < 0.001$, $^{****}P < 0.0001$. Data are presented as mean ± SD. Part of (**a**) is created in BioRender. Sheng, X. (2026) https://BioRender.com/xd1lxc5.

the digital domain, the data is transmitted to the Bluetooth module for wireless signal transmission. Conversely, the biasing link functions in the opposite direction: upon receiving specific commands from the host computer, the Bluetooth module processes the signal and controls the Pattern Generator to produce the designated waveform. The Voltage Control module enables electrochemical measurements such as cyclic voltammetry (CV) and chronoamperometry (I-t). The interface circuit system is powered by a Li-battery, with a Reference circuit and a low-dropout regulator (LDO) providing a stable reference voltage and power supply to other circuit components. The proposed system has a compact form factor of $2.23 \times 1.76 \times 0.83\ cm^3$, weighs approximately 1.2 g, and operates with a power consumption of less than 20 mW.

### Characterization of the PEGDA/peptide hydrogel

The Fourier-transform infrared spectroscopy (FTIR, Nicolet iS50) was used to analyze the chemical composition of the hydrogel materials. The microstructure of the hydrogels was examined using a scanning electron microscope (SEM, Merlin, Zeiss). The morphology of hydrogel was characterized after lyophilization, and the cross-sectional microstructure was observed following rapid quenching in liquid nitrogen. Additionally, the adhered hydrogel/hydrogel and hydrogel/tissue interfaces were also investigated by the SEM. The adhesion performance was quantified as the adhesion energy, namely the amount of energy required to increase a unit area of interfacial crack. The adhesion energy was determined by either 180° peeling adhesion tests (ASTM F2256), or lap shear adhesion tests (ASTM F2255) with a mechanical testing machine (EZ-LX HS, Shimadzu, 100 N load-cell), similar to previously reported methods[70,71]. PET films served as the stiff backing for adhesion measurement. Specifically, for 180° peeling tests, two pieces of as-prepared hydrogels (15 mm × 8 mm × 1 mm) were brought in contact and stored at 37 °C with 90% RH overnight before the measurement. The adhesion energy was determined by two times the plateau force divided by the width. The tests were performed with a constant tensile speed ($5\ mm\ min^{-1}$). Adhesion between hydrogels and biological tissues was also investigated. Animal tissues, including skin, heart, intestine and liver, were collected from a sacrificed Landrace pig, then cleaned with ethanol and DI water prior to measurement. Two porcine tissues were bonded using PEGDA/peptide hydrogel, creating a sandwich structure, with an adhesion area of 10 mm × 8 mm. Each side of the bonded tissues was stretched. Moreover, wet adhesion between hydrogels and between hydrogels and porcine tissues were measured through lap shear test. The adhesion area is 3 mm × 3 mm and the tensile speed is $5\ mm\ min^{-1}$. The hydrogel-hydrogel or hydrogel-tissue-hydrogel sandwich structures were immersed in PBS at 37 °C, and their adhesion was measured at various time points. Adhesion strength was calculated by dividing the maximum force by the adhesion area. The effects of varying concentration (1.0–3.0 g/L) and molecular weight (0.8–1, 50, 190–310, 500 to 1000 kDa) of chitosan on adhesion were evaluated using peeling adhesion tests. Influence of adhesion strength of PEGDA/peptide hydrogels modified with genipin or bridging polymer chitosan was also evaluated through peel tests. ASTM F2392 standard protocol was adopted for measuring burst pressure similar to previous reports[34]. Briefly, 2 cm-diameter pieces of porcine tissues (heart, intestine and stomach) were cut and cleaned with PBS to remove excessive fat, and fixed to the chamber connected to a syringe pump. The pressure was applied by pumping PBS using the syringe pump at a rate of 2 mL/min from the bottom of the specimen. A 5 mm-diameter hole was punched at the center of the tissue, and a small amount of PBS was applied on tissue surface to keep it moist. The PEGDA/peptide hydrogel film and surgical sealants (N-butyl-2-cyanoacrylate and N-ethyl-2-cyanoacrylate) were applied over the perforated tissue. Burst pressure was measured after adhesives were in contact with the tissue for 1 h at 37 °C. The maximum pressure reached before any pressure loss due to rupture was recorded as the burst pressure. Different hydrogel samples were cut into dumbbell shapes (ISO 527-3 sample 5B, $L_0 = 10$ mm, b = 2 mm, h = 1 mm) and the strain-stress curves were obtained with a mechanical testing machine (EZ-LX HS, Shimadzu) at a constant stretching rate ($5\ mm\ min^{-1}$). Toughness was determined as the area under the stress-strain curve up to fracture. To assess the water uptake capacity of the hydrogels, swelling behaviors were evaluated for hydrogels with different peptide concentrations (0, 5, 10, 15, 20, and 25 g/L). Prior to the experiment, the hydrogels were dried with a dryer, and their initial dry weight ($W_O$) was recorded. Then, the hydrogels were soaked in PBS, and the weight of the hydrogels was sampled at different stages, denoted as $W_s$. The swelling percentage was calculated as $(W_s - W_O)/W_O \times 100\%$. In vitro biodegradation of PEGDA/peptide hydrogel with varying peptide concentrations was evaluated in PBS. Hydrogel samples were cut into square specimens (15 mm × 15 mm × 2 mm), and their dry weights were measured after oven drying. The samples were then immersed in PBS at 37 °C. The hydrogels were removed from PBS at different stages, gently rinsed with fresh PBS, and dried completely before weight measurement. The remaining mass percentage was calculated as the ratio of the final dry weight to the initial dry weight.

### Characterization of the lactate sensor

The electrode morphology was characterized using an SEM (SEM, Merlin, Zeiss), while elemental distribution was analyzed by energy-dispersive X-ray spectroscopy (EDS) mapping. The crystal structure was determined by X-ray diffraction (XRD, D/max-2550) and Raman spectroscopy (Horiba LabRAM HR Evolution) with a 532 nm yttrium aluminum garnet (YAG) laser. Chemical composition at the surface was assessed via X-ray photoelectron spectroscopy (XPS, 250XI). All electrochemical tests were conducted in a three-electrode setup with 1 M PBS using a CHI 650E electrochemical workstation (Shanghai Chenhua Co., Ltd., China) at 37 °C. For the electrical connection, copper (Cu) wires were connected to one side of the $Mo/MoO_x$ electrodes with the assistance of silver paste. The connection area was encapsulated by 3140 adhesives (Dow Coming Corp. USA) to alleviate the corrosion of PBS, guaranteeing the operational stability of tests in liquid environment. EIS was conducted at the open circuit potential with frequencies

https://doi.org/10.1038/s41467-026-74248-w

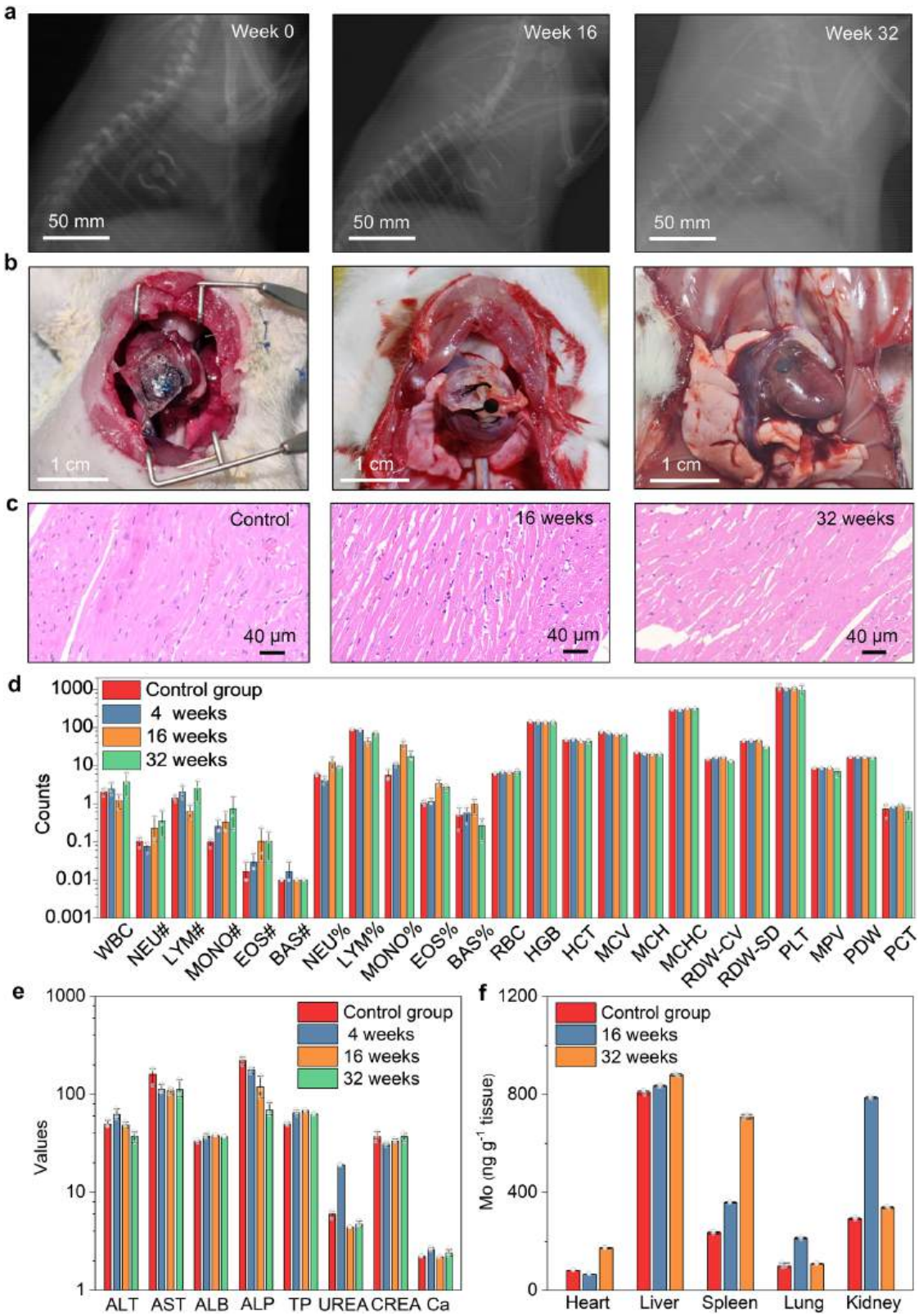


ranging from 0.1 Hz to 1 MHz, with an amplitude of 5 mV. The stability of Mo/$MoO_x$ electrodes (used as WE, CE or RE) were investigated by monitoring the open circuit voltage over time. Amperometry was employed for lactate detection. CV was performed at a scan rate of 0.01–0.1 V over a potential range of −0.8 to 0.4 V to determine the amperometry potential. CV characteristics of WE with and without enzyme immobilization were investigated. Amperometry was performed with a constant voltage of −0.65 V applied between the WE and RE, and the current between WE and CE was recorded for lactate detection. To ensure accurate and stable current signals for the lactate calibration curve (particularly at low concentrations), mechanical stirring was applied to homogenize lactate concentration prior to measurement, followed by a brief stabilization period without stirring during data acquisition. Sensor selectivity was evaluated by

**Fig. 6 | Bioresorbability and biocompatibility of the bioresorbable lactate sensor at the heart of SD rats. a** Digital Radiography (DR) images of rats collected over 32 weeks after the implantation of lactate sensor. **b** Images of sensors implanted onto the myocardial surface of rats at different stages of bioresorption over the course of 32 weeks. **c** Hematoxylin-eosin (HE) staining images of heart tissues at the implantation site: (left) control group without sensor implantation, (middle) 16 weeks postimplantation, and (right) 32 weeks postimplantation. **d**, **e** Analysis of complete blood counts and blood chemistry of SD rats with and without sensor implantation. **f** Inductively coupled plasma-mass spectrometry (ICP-MS) results showing Mo concentrations of the tissues at major organs of SD rats with and without sensor implantation. WBC: white blood cell (×1000 $\mu L^{-1}$); NEU# neutrophils (×1000 $\mu L^{-1}$), LYM#: lymphocytes (×1000 $\mu L^{-1}$); MONO#: monocytes (×1000 $\mu L^{-1}$), EOS# eosinophils (×1000 $\mu L^{-1}$), BAS# basophils (×1000 $\mu L^{-1}$), NEU% percentage of neutrophils (%), LYM% percentage of lymphocytes (%), MONO %: percentage of monocytes (%); EOS% percentage of eosinophils (%), BAS% percentage of basophils%, RBC red blood cell (×1,000,000 $\mu L^{-1}$), HGB blood hemoglobin level (g $L^{-1}$), HCT hematocrit level (%), MCV mean corpuscular volume (fL), MCH mean corpuscular hemoglobin (pg), MCHC mean corpuscular hemoglobin concentration (g $L^{-1}$), RDW-CV: coefficient of variation of red cell distribution width (%); RDW-SD: standard deviation of red cell distribution width (fL), PLT platelet count in blood (×1000 $\mu L^{-1}$), MPV mean platelet volume (fL), PDW platelet distribution width, PCT plateletcrit (%), ALT alanine aminotransferase (U $L^{-1}$), AST aspartate transaminase (U $L^{-1}$); ALB: albumin (g $L^{-1}$); ALP: alkaline phosphatase (U $L^{-1}$), TP total protein (g $L^{-1}$), UREA blood urea nitrogen (mmol $L^{-1}$); CREA: creatinine (μmol $L^{-1}$); Ca: calcium (mmol $L^{-1}$). In (**a**–**f**), $n = 3$ independent experiments. In (**d**–**f**), data are presented as mean ± SD.

sequentially adding interferent chemicals (10 mM UA, 10 mM urea, 10 mM AA, and 10 mM glucose) to PBS under stirring, with current responses recorded. Selectivity was quantified as the ratio of the interferent response current to the lactate response current. Bridging agents are applied carefully to the surface of the hydrogel substrate, while avoiding direct contact with the working electrode to prevent interference with sensing performance. In its viscous state and applied in small quantities, the bridging agent does not spread onto the working electrode surface. The sensor is then placed onto the target tissue, and gentle pressure is applied for 30 s to 3 min to promote immobilization. Over time, the bridging agents gradually diffuse into both the tissue and the hydrogel, achieving intimate and stable device–tissue interface. To evaluate the influence of motion on recorded signals, the bioresorbable sensor was deployed on an ex vivo porcine heart mounted on a heart-motion simulator (XW0928, Beijing Shengxi Medical Technology Co., Ltd.) operating at a beating rate of 75 beats per minute. The sensor was soaked in PBS at 37 °C, with calibration curves and selectivity assessed on days 0, 2, 6, and 9. For signals affected by motion artifacts, the recorded data are processed using low-pass filtering (0.5–2 Hz) followed by LOWESS smoothing to effectively attenuate motion-induced noise and reveal the underlying lactate dynamics.

### Animal models with systemic hypoxia

The New Zealand rabbits (age 6–9 years, weight 3–5 kg) were maintained according to the institutional guidelines of Tsinghua University. For hypoxia models induced by $N_2/O_2$ gas mixture delivery, anesthesia of rabbits was induced with Sutai liquid (0.8–1.3 mL $kg^{-1}$), and adequacy was assessed by toe pinch and palpebral reflex. The heart was exposed through a left thoracotomy, and the lactate sensor was implanted within the pericardial cavity. The sensor's connecting wires, anchored subcutaneously and secured with 6-0 polypropylene sutures, were exteriorized through the chest wall for electrical connection. Rabbits were subjected to dynamic adjustments of inspired $O_2$ levels using a custom $N_2/O_2$ gas mixture controlled by dual flowmeters. The gas blend was delivered via a manual resuscitator (Beijing Shenlu Tengfei Medical Technology Co., Ltd). Hypoxia was induced by modulating the $N_2/O_2$ ratio to achieve target arterial $O_2$ pressures. For hypoxia models induced by RR variation, anesthesia was induced via intravenous injection of propofol, followed by endotracheal intubation. Anesthesia maintenance was sustained with isoflurane delivered through a ventilator (Drager Evita, Primus Apparatus). Hypoxia was induced by adjusting the RR on the ventilator, with oxygen concentration at 21% and gas flow at 2 L/min. Blood lactate levels were monitored in the auricular artery simultaneously using a blood gas analyzer (I-STAT300-G, Abbott Point of Care Inc.) at varying RRs.

### Animal models with local hypoxia models

For the thigh hypoxia model, ligation was performed on anesthetized rabbits using a surgical string. After an initial monitoring period, the ligature was tightened to induce severe ischemia and subsequently released to restore blood flow. Changes in lactate levels were monitored by the sensor implanted in the thigh muscle, which was connected to a wireless circuit affixed to the thigh.

For the heart hypoxia model, the lactate sensor was implanted within the pericardial space of anesthetized rabbits. Myocardial ischemia was induced by ligating the anterior descending and second diagonal coronary branches using polypropylene sutures. After lactate monitoring, the sutures were cut to restore blood flow to the heart.

For cerebral hypoxia models, Landrace pigs (3 months old, ~30 kg) were anesthetized via intramuscular injection of a Zoletil 50 and xylazine mixture (0.03 mL $kg^{-1}$). After shaving the scalp and exposing the skull, ~2 cm cranial openings were drilled using a portable electric sander (KRK1806, Keruika Trading Co., Ltd.). The lactate sensor was implanted on the dural surface through these openings, which were sealed with medical gauze, and the sensor's connecting wires were secured with medical tape and connected to external wireless circuit. To induce cerebral hypoxia, the right common carotid artery was ligated using a 2-0 surgical mousse suture. After a monitoring period, the left common carotid artery was subsequently ligated to induce severe ischemia for an extended duration.

### Animal models with epilepsy

For an epilepsy model, anesthetized rabbits were placed in a standard stereotaxic instrument for surgical implantation. After shaving the scalp and exposing the skull, small holes (~0.5 mm) were drilled in the skull using a micromotor drill (STRONG 90, Shanghai Puxin Instrument Technology Co., Ltd.). Local field potentials (LFP) electrodes, made of twisted Teflon-coated tungsten wires (catalogue no. 796000, A-M Systems), were targeted at the hippocampal region. A stainless-steel screw acted as the reference electrode and was implanted in the skull. The lactate sensor was implanted on the cerebral cortex surface. Connecting wires were secured to the stereotaxic instrument with medical tape and connected to a wireless circuit. To induce epilepsy, 0.1 g/mL penicillin G was injected into the hippocampus at a rate of 1 μL/30 s using a micro-injection pump (LSP01-1A, Baoding Ditron Electronic Technology Co., Ltd). LFP recordings were obtained using an electrophysiological recording system (alphaRS Pro, Alpha Omega Engineering).

### Animal models with septic shock

For the sepsis model, the body temperature of anesthetized rabbits was maintained using a heating pad throughout the experiment. Three lactate sensors were implanted: one within the pericardial space, one in the dorsal subcutaneous tissue, and one in the thigh muscle. The connecting wires from the heart, back, and thigh sensors were connected to a wireless circuit. A catheter was inserted into the auricular vein for LPS administration, and another into the right femoral artery to monitor mean arterial pressure (MAP) using a patient monitor (IntelliVue MP60, Philips) and to blood sample collection. Heart rate

(HR), blood oxygen saturation ($SpO_2$) and temperature were also recorded. 2 mg/kg lipopolysaccharide (LPS) was slowly injected into the rabbits through the intravenous catheter at a rate of 100 μL/min to induce septic shock. Normal saline was administered intravenously at either the early sign of rising pericardial lactate (lactate >125% of baseline) or the onset of septic shock (MAP < 75% of baseline). Blood lactate levels were measured from the femoral artery using a blood gas analyzer at defined surgical time points.

### Evaluation of Long-term lactate sensing

The SD rats (age 6–9 weeks, weight 250–300 g) were used for long-term lactate monitoring. Rats were anesthetized using an isoflurane anesthesia machine (R500IP, RWD Life Science Co., Ltd). The lactate sensor was implanted in the thigh muscles, with the connecting wires of the sensor being secured by medical tapes. Lactate levels in the thigh muscle were monitored at day 0, 2, 4, 7, and 10 post-implantations during acute ischemia induced by thigh ligation as described earlier. In addition, baseline currents were monitored prior to thigh ligation on days 0, 4, 7, 10, and 11 post-implantation.

### Biodegradation and biocompatibility tests

The in vivo degradation of the lactate sensor was investigated using SD rats. With isoflurane gas anesthesia, a thoracotomy was performed on the anesthetized animal, and the lactate sensor was implanted within the pericardial space. A Mobile Digital X-ray Diagnostic System was used to track the degradation process at various stages. At week 4, 16, and 32, blood samples were collected from animals via the cardiac vein into K-EDTA and gel tubes for blood counts and blood chemistry tests, respectively. Servicebio Co., Ltd. conducted the assays. Hematoxylin and eosin (H&E) staining was performed on surrounding tissues at the implantation sites at 16 and 32 weeks postoperatively. The tissues were cut into small pieces and fixed in formalin for one week. Subsequently, the tissues were embedded in paraffin wax and cut into 4-μm slices. The sections were incubated with hematoxylin and eosin at room temperature and examined under an optical microscope. Moreover, surrounding heart tissues near the implanted sensor, as well as liver, kidney, spleen and kidney from the rats, were obtained for inductively coupled plasma mass spectrometry (ICP-MS) to assess the residual concentration of Mo.

### Ethics

All animal experiments were conducted in accordance with protocols approved by the institutional ethics committee, including the Institutional Animal Care and Use Committee (IACUC) of Tsinghua University (approval number: 18-SX-1), the Institutional Animal Care and Use Committee (IACUC) of Fuwai Hospital (approval number: 0108-4-7-ZX(X)-44 and 0108-7-18-2X(X)-1), and the Experimental Animal Ethics Committee of PLA General Hospital (approval number: 2016-x9-07).

### Statistical analysis

Statistical analysis was performed using SPSS software (version 27.0) for two-group comparisons with an unpaired t-test and for multi-group comparisons using one-way ANOVA followed by Turkey test or Dunnett's T3. Significance levels were set at $^{*}P < 0.05$, $^{**}P < 0.01$, $^{***}P < 0.001$, $^{****}P < 0.0001$, pairwise comparisons not shown on graphs were $p > 0.05$ (not significant). Data are presented as mean ± standard devi.

## Data availability

All data needed to evaluate the conclusions in the paper are present in the paper and/or the Supplementary Materials. Additional data related to this paper may be requested from the authors. Source data are provided with this paper.

## References


1. Li, X. et al. Lactate metabolism in human health and disease. *Signal Transduct. Tar.* **7**, 305 (2022).
2. Magistretti, P. J. & Allaman, I. Lactate in the brain: from metabolic end-product to signalling molecule. *Nat. Rev. Neurosci.* **19**, 235–249 (2018).
3. Llibre, A. et al. Lactate: A key regulator of the immune response. *Immunity* **58**, 535–554 (2025).
4. Janotka, M. & Ostadal, P. Biochemical markers for clinical monitoring of tissue perfusion. *Mol. Cell Biochem* **476**, 1313–1326 (2021).
5. Lim, H. S. Cardiogenic shock: failure of oxygen delivery and oxygen utilization. *Clin. Cardiol.* **39**, 477–483 (2016).
6. Haas, S. A. et al. Severe hyperlactatemia, lactate clearance and mortality in unselected critically ill patients. *Intensive Care Med.* **42**, 202–210 (2016).
7. Rudd, K. E. et al. Global, regional, and national sepsis incidence and mortality, 1990–2017: analysis for the Global Burden of Disease Study. *Lancet* **395**, 200–211 (2020).
8. Sharma, A. et al. Global awareness of myocardial infarction symptoms in general population: a systematic review and meta-analysis. *Korean Circ. J.* **51**, 983–996 (2021).
9. Evans, L. et al. Surviving sepsis campaign: international guidelines for management of sepsis and septic shock 2021. *Crit. Care Med.* **49**, e1063–e1143 (2021).
10. Singer, M. et al. The third international consensus definitions for sepsis and septic shock (Sepsis-3). *JAMA* **315**, 801–810 (2016).
11. Dettmer, M., Holthaus, C. V. & Fuller, B. M. The impact of serial lactate monitoring on emergency department resuscitation interventions and clinical outcomes in severe sepsis and septic shock: an observational cohort study. *Shock* **43**, 55–61 (2015).
12. Gorgis, N. et al. Evaluation of the association of early elevated lactate with outcomes in children with severe sepsis or septic shock. *Pediatr. Emerg. Care* **35**, 661–665 (2019).
13. Gauer, R., Forbes, D. & Boyer, N. Sepsis: diagnosis and management. *Am. Fam. Physician* **101**, 409–418 (2020).
14. Wang, G. et al. Microcirculation and mitochondria: the critical unit. *J. Clin. Med* **12**, 6453 (2023).
15. Bakker, J. Lactate levels and hemodynamic coherence in acute circulatory failure. *Best. Pract. Res. Clin. Anaesthesiol.* **30**, 523–530 (2016).
16. Lafuente, J.-L. et al. Continuous and non-invasive lactate monitoring techniques in critical care patients. *Biosensors* **14**, 148 (2024).
17. Robinson, T. E. & Justice, J. B. *Microdialysis in the neurosciences: techniques in the behavioral and neural sciences*, vol. 7. Elsevier, 2013.
18. Cho, S. et al. A skin-interfaced microfluidic platform supports dynamic sweat biochemical analysis during human exercise. *Sci. Transl. Med.* **16**, eado5366 (2024).
19. Ruggeri, E. et al. Paper-Based Wearable Patches for Real-Time, Quantitative Lactate Monitoring. *Adv. Sens. Res.* **3**, 2300141 (2024).
20. Sempionatto, J. R. et al. Wearable chemical sensors for biomarker discovery in the omics era. *Nat. Rev. Chem.* **6**, 899–915 (2022).
21. Hu, C. et al. Recent development of implantable chemical sensors utilizing flexible and biodegradable materials for biomedical applications. *ACS Nano* **18**, 3969–3995 (2024).
22. Arwani, R. T. et al. Stretchable ionic–electronic bilayer hydrogel electronics enable in situ detection of solid-state epidermal biomarkers. *Nat. Mater.* **23**, 1115–1122 (2024).
23. Chang A.-Y., et al. Integration of chemical and physical inputs for monitoring metabolites and cardiac signals in diabetes. *Nat Biomed Eng*, 1–16 (2025).
24. Booth, M. A. et al. Fiber-based electrochemical biosensors for monitoring pH and transient neurometabolic lactate. *Anal. Chem.* **93**, 6646–6655 (2021).

25. Sardesai, N. P. et al. Platinum-doped ceria based biosensor for in vitro and in vivo monitoring of lactate during hypoxia. *Anal. Chem.* **87**, 2996–3003 (2015).
26. Li, X. et al. A programmable bioresorbable electrochemical microneedle sensor array for perioperative monitoring of organ health. *Nat. Biomed. Eng*. 1–18 (2026).
27. Zhang, Y. et al. Advances in bioresorbable materials and electronics. *Chem. Rev.* **123**, 11722–11773 (2023).
28. Koh, L. M. & Khor, S. M. Current state and future prospects of sensors for evaluating polymer biodegradability and sensors made from biodegradable polymers: A review. *Anal. Chim. Acta* **1217**, 339989 (2022).
29. Corsi, M. et al. Implantable bioresorbable electronic systems for sustainable precision medicine. *Nat. Rev. Electrical Eng.* **2**, 1–12 (2025).
30. Fernandes, C. et al. A Fully-Bioresorbable Nanostructured Molybdenum Oxide-Based Electrode for Continuous Multi-Analyte Electrochemical Sensing. *Adv. Mater. Interfaces* **11**, 2400054 (2024).
31. Li, J. et al. Fully printed and self-compensated bioresorbable electrochemical devices based on galvanic coupling for continuous glucose monitoring. *Sci. Adv.* **9**, eadi3839 (2023).
32. Liang, M. et al. A high-strength double network polydopamine nanocomposite hydrogel for adhesion under seawater. *J. Mater. Chem. B* **8**, 8232–8241 (2020).
33. Zhai, H. et al. Mechanically strengthened hybrid peptide-polyester hydrogel and potential applications in spinal cord injury repair. *Biomed. Mater.* **15**, 055031 (2020).
34. Li, J. et al. Tough adhesives for diverse wet surfaces. *Science* **357**, 378–381 (2017).
35. Liu, S. et al. A biodegradable, adhesive, and stretchable hydrogel and potential applications for allergic rhinitis and epistaxis. *Adv. Healthc. Mater.* **12**, 2302059 (2023).
36. Butler, M. F., Ng, Y. F. & Pudney, P. D. Mechanism and kinetics of the crosslinking reaction between biopolymers containing primary amine groups and genipin. *J. Polym. Sci., Part A: Polym. Chem.* **41**, 3941–3953 (2003).
37. Reay, S. L. et al. In vitro evaluation of the biodegradability of chitosan–genipin hydrogels. *Mater. Adv.* **3**, 7946–7959 (2022).
38. Yin, L. et al. Dissolvable metals for transient electronics. *Adv. Funct. Mater.* **24**, 645–658 (2014).
39. Yang, H. & Yan, S. A comprehensive review of electrochemical lactate biosensors: Principles, innovations, and future perspectives. *Int. J. Electrochem. Sci*. **20**, 101132 (2025).
40. Zhang, B. Y. et al. Degenerately hydrogen doped molybdenum oxide nanodisks for ultrasensitive plasmonic biosensing. *Adv. Funct. Mater.* **28**, 1706006 (2018).
41. Xu, J. et al. Ultrastretchable wearable strain and pressure sensors based on adhesive, tough, and self-healing hydrogels for human motion monitoring. *ACS Appl Mater. Interfaces* **11**, 25613–25623 (2019).
42. Andersen, L. W. et al. Etiology and Therapeutic Approach to Elevated Lactate Levels. *Mayo Clin. Proc.* **88**, 1127–1140 (2013).
43. Yao, H. & Haddad, G. G. Calcium and pH homeostasis in neurons during hypoxia and ischemia. *Cell Calcium* **36**, 247–255 (2004).
44. Siesjö, B. K. et al. Extra-and intracellular pH in the brain during seizures and in the recovery period following the arrest of seizure activity. *J. Cereb. Blood Flow. Metab.* **5**, 47–57 (1985).
45. Park, M. et al. Physicochemical characterization of metabolic acidosis induced by normal saline resuscitation of patients with severe sepsis and septic shock. *Rev. Brasileira de. Ter. Intensiv.* **23**, 176–182 (2011).
46. Cohen, N. S., Bock, J. M. & May, A. K. Sepsis and postoperative surgical site infections. *Surgery* **174**, 403–405 (2023).
47. Staff, N. P. et al. Post-surgical inflammatory neuropathy. *Brain* **133**, 2866–2880 (2010).
48. Paruk, F. & Chausse, J. M. Monitoring the post surgery inflammatory host response. *J. Emerg. Crit. Care Med.* **3**, 47 (2019).
49. Zhang, P. et al. Zwitterionic gel encapsulation promotes protein stability, enhances pharmacokinetics, and reduces immunogenicity. *Proc. Natl. Acad. Sci.* **112**, 12046–12051 (2015).
50. Keefe, A. J. & Jiang, S. Poly (zwitterionic) protein conjugates offer increased stability without sacrificing binding affinity or bioactivity. *Nat. Chem.* **4**, 59–63 (2012).
51. GhavamiNejad, A. et al. Continuous insulin monitoring using an antibody-protecting zwitterionic microneedle patch. *Nat. Biomed. Eng.* **10**, 445–457 (2026).
52. Lele, A. V. et al. Perioperative management of adult patients with external ventricular and lumbar drains: guidelines from the Society for Neuroscience in Anesthesiology and Critical Care. *J. Neurosurg. Anesthesiol.* **29**, 191–210 (2017).
53. Ingvar, M. & Siesjö, B. K. Local blood flow and glucose consumption in the rat brain during sustained bicuculline-induced seizures. *Acta Neurol. Scand.* **85**, 129–144 (1992).
54. Wanleenuwat, P., Suntharampillai, N. & Iwanowski, P. Antibiotic-induced epileptic seizures: mechanisms of action and clinical considerations. *Seizure* **81**, 167–174 (2020).
55. Fernandes, E. et al. Amperometric bio-sensing of lactate and oxygen concurrently with local field potentials during status epilepticus. *Talanta* **268**, 125302 (2024).
56. Kamade, S. B. The Role of Medical-Surgical Nurses in Managing Chronic and Acute Conditions: A Comprehensive Review. *Spectr. J.* **1**, 49–55 (2025).
57. Lin, Y., Xu, Y. & Zhang, Z. Sepsis-induced myocardial dysfunction (SIMD): the pathophysiological mechanisms and therapeutic strategies targeting mitochondria. *Inflammation* **43**, 1184–1200 (2020).
58. Wasyluk, W. & Zwolak, A. Metabolic alterations in sepsis. *J. Clin. Med* **10**, 2412 (2021).
59. Kawaguchi, S. & Okada, M. Cardiac metabolism in sepsis. *Metabolites* **11**, 846 (2021).
60. Wiel, E. et al. Effects of the angiotensin-converting enzyme inhibitor perindopril on endothelial injury and hemostasis in rabbit endotoxic shock. *Intensive Care Med.* **30**, 1652–1659 (2004).
61. Shankar-Hari, M. et al. Developing a new definition and assessing new clinical criteria for septic shock: for the third international consensus definitions for sepsis and septic shock (Sepsis-3). *JAMA* **315**, 775–787 (2016).
62. Falter, F. et al. Serial Lactate in Clinical Medicine-A Narrative Review. *J. Intens. Care Med.* **41**, 175–185 (2026).
63. Zaksas, N. P., Soboleva, S. E. & Nevinsky, G. A. Twenty Element Concentrations in Human Organs Determined by Two-Jet Plasma Atomic Emission Spectrometry. *Sci. World J.* **2019**, 9782635 (2019).
64. Wu, J. et al. Adhesive anti-fibrotic interfaces on diverse organs. *Nature* **630**, 360–367 (2024).
65. Harding, J. L. & Reynolds, M. M. Combating medical device fouling. *Trends Biotechnol.* **32**, 140–146 (2014).
66. Chen, Y. et al. A biochemical sensor with continuous extended stability in vivo. *Nat Biomed Eng.* **9**, 1–14 (2025).
67. Saxena, S. et al. Zwitter-repel: An anti-fouling coating promoting electrochemical biosensing in biological fluids. *Chem. Eng. J.* **495**, 153522 (2024).
68. Xie, X. et al. Reduction of measurement noise in a continuous glucose monitor by coating the sensor with a zwitterionic polymer. *Nat. Biomed. Eng.* **2**, 894–906 (2018).
69. Yuk, H. et al. Tough bonding of hydrogels to diverse non-porous surfaces. *Nat. Mater.* **15**, 190–196 (2016).
70. Rivlin, R. S. & Thomas, A. G. Rupture of rubber. I. Characteristic energy for tearing. *J. Polym. Sci.* **10**, 291–318 (1953).
71. Yuk, H. et al. Dry double-sided tape for adhesion of wet tissues and devices. *Nature* **575**, 169–174 (2019).

## Author contributions

C.H., B.L. and L.Y. conceived the idea. C.H., Ruizhang L., Rongfeng L., Shengnan L., Zhenyu W. and L.Y. performed material design, fabrication, and characterization. Y.M., L.W., X.R., H.D. and M.Z. performed wireless circuit design and fabrication. C.H., R.L., P.L., Y.X., L.W., M.P., B.S, Shen L, Z.M., X.P., S.W., Y.D., Z.J., W.X., M. X., L.L., H.Q., L.T., J.P. and W.S. performed biological experiments. C.H., Zheyao W., S.W., W.F., X.S., X.J., B.L., and L.Y. participated data analysis discussion. C.H. and L.Y. wrote the paper in consultation with the rest of the authors.

## Funding

The project was supported by Tsinghua-Toyota Joint Research Fund, the National Natural Science Foundation of China (32571534 to L.Y., T2425003 and 52272277 to X.S., 32571556 to L.W.), Tsinghua University Initiative Scientific Research Program (2024Z02ORD001, to X.S.), Beijing Natural Science Foundation (Z220015 and L254019 to L.Y., L244088 to L.W.), Beijing Nova Program (20230484254 and 20240484742 to H.D.).

## Competing interests

The authors declare no competing interests.

## Additional information

**Supplementary information** The online version contains supplementary material available at https://doi.org/10.1038/s41467-026-74248-w.

**Correspondence** and requests for materials should be addressed to Jiang Peng, Xin Jin, Baotong Li or Lan Yin.

**Peer review information** *Nature Communications* thanks Jiaqi Liu, and the other, anonymous, reviewer(s) for their contribution to the peer review of this work. A peer review file is available.



**Chen Hu[1,2,3,31], Ruizhang Liang[1,2,3,31], Pengkai Li[4,5,6,7,31], Yuan Ma[8], Yang Xie[9], Shengnan Liu[1,2,3], Liu Wang[10,11,12], Manqi Peng[13], Boyu Shen[1,2,3], Xuechun Ren[14,15], Zhenyu Wang[1,2,3], Lingfeng Wu[8], Shen Li[4,5,6,16], Zhaodi Mi[4,5,6,16], Xiwei Peng[4,5,6], Sice Wang[4,5,6], Yanghui Dong[4,5,6], Zhibo Jia[4,5,6], Wenjing Xu[17], Moling Xiao[4,5,6], Limei Liu[18], Zheyao Wang[8], Hui Qi[19], Lei Tian[20], He Ding[14,15,21], Rongfeng Li[22], Shirong Wang[23], Wangyang Fu[1,2,3], Xing Sheng[3,24,25,26,27], Wei Su[28], Milin Zhang[8], Jiang Peng[4,5,6] ✉, Xin Jin[29] ✉, Baotong Li[30] ✉ & Lan Yin[1,2,3] ✉**

[1]School of Materials Science and Engineering, Tsinghua University, Beijing, P. R. China. [2]The Key Laboratory of Advanced Materials of Ministry of Education, Tsinghua University, Beijing, P. R. China. [3]State Key Laboratory of Flexible Electronics Technology, Tsinghua University, Beijing, P. R. China. [4]Beijing Key Lab of Regenerative Medicine in Orthopedics, Chinese PLA General Hospital, Beijing, China. [5]Key Laboratory of Musculoskeletal Trauma and Injuries PLA, Chinese PLA General Hospital, Beijing, China. [6]Department of Orthopedics, The Fourth Medical Center, Chinese PLA General Hospital, Beijing, China. [7]Dalian Rehabilitation and Recuperation Center of the Chinese PLA, Dalian, China. [8]Department of Electronic Engineering, Tsinghua University, Beijing, China. [9]Nanjing Research Institute of Electronics Technology, China Electronics Technology Group Corporation, Nanjing, China. [10]School of Biological Science and Medical Engineering, Beihang University, Beijing, P. R. China. [11]Key Laboratory of Biomechanics and Mechanobiology of Ministry of Education, Beihang University, Beijing, P. R. China. [12]Beijing Advanced Innovation Center for Biomedical Engineering, Beihang University, Beijing, P. R. China. [13]School of Integrated Circuit, Tsinghua University, Beijing, China. [14]School of Optics and Photonics, Beijing Institute of Technology, Beijing, China. [15]Beijing Engineering Research Center of Mixed Reality and Advanced Display, Beijing, China. [16]Hebei North University, Graduate School, Zhangjiakou, China. [17]Department of Orthopedics, The First Medical Center, Chinese PLA General Hospital, Beijing, China. [18]School of Clinical Medicine, Qinghai University, Xining, China. [19]Laboratory of Musculoskeletal Regenerative Medicine, Beijing Institute of Traumatology and Orthopaedics, Beijing, China. [20]Department of Cardiovascular Surgery, The Ninth Medical Center, Chinese PLA General Hospital, Beijing, China. [21]Frontier Interdisciplinary Domain, Beijing Institute of Technology, Zhuhai, Guangdong, China. [22]Institute of Optics and Electronics, Jingjinji National Center of Technology Innovation, Beijing, China. [23]TRANSVISTA, Transcend Vivoscope Biotech Co. Ltd, Beijing, P. R. China. [24]Department of Electronic Engineering, Tsinghua University, Beijing, P. R. China. [25]Beijing National Research Center for Information Science and Technology, Tsinghua University, Beijing, P. R. China. [26]Institute for Precision Medicine, Tsinghua University, Beijing, P. R. China. [27]IDG/McGovern Institute for Brain Research, Tsinghua University, Beijing, P. R. China. [28]School of Clinical Medicine, Beijing Tsinghua Chang Gung Hospital, Tsinghua University, Beijing, China. [29]Department of Intensive Care Medicine, The Third Xiangya Hospital of Central South University, Changsha, China. [30]National Clinical Research Center of Cardiovascular Diseases, Fuwai Hospital, Chinese Academy of Medical Sciences and Peking Union Medical College, Beijing, China. [31]These authors contributed equally: Chen Hu, Ruizhang Liang, Pengkai Li. ✉e-mail: pengjiang301@126.com; shirley_star@163.com; xingzhelbt@163.com; lanyin@tsinghua.edu.cn

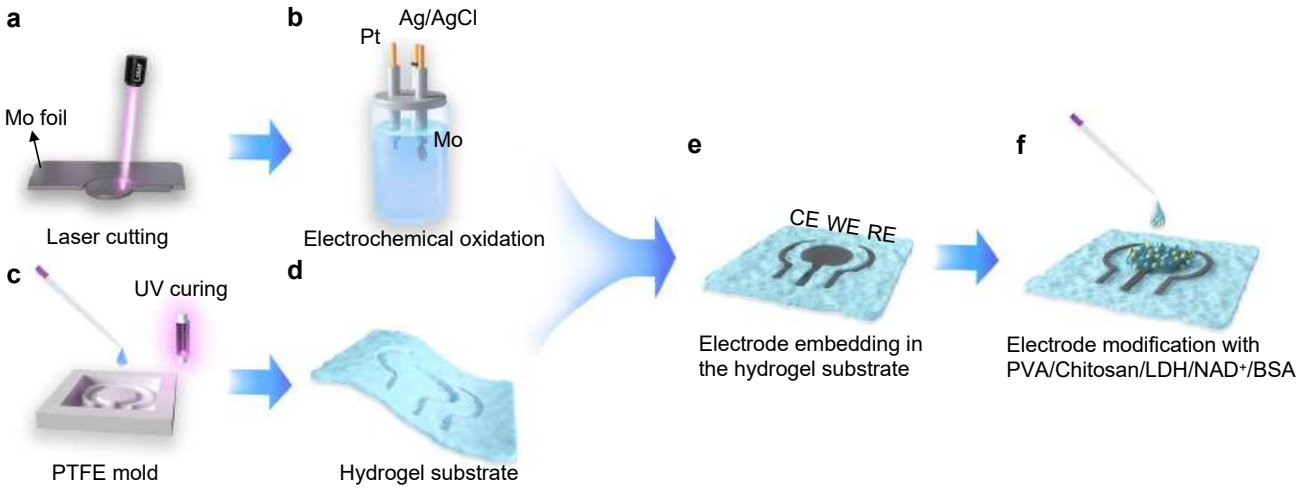


**Supplementary Fig. 1 | Fabrication process of the bioresorbable and flexible lactate sensor with an adhesive hydrogel substrate.** **a**, Electrodes is laser-cut from a molybdenum sheet. **b**, Electrochemical oxidation of Mo to form Mo/$MoO_x$ electrodes as the working electrode (WE), counter electrode (CE), and reference electrode (RE) for lactate sensing. **c**, UV curing of the hydrogel substrate within the polytetrafluoroethylene (PTEF) mold. **d**, Patterned bioresorbable, flexible and adhesive hydrogel substrate. **e**, Integration of the Mo/$MoO_x$ electrodes with the hydrogel substrate. **f**, Coating of the WE with a mixture of lactate dehydrogenase (LDH), nicotinamide adenine dinucleotide ($NAD^+$), bovine serum albumin (BSA), poly(vinyl alcohol) (PVA), and chitosan.

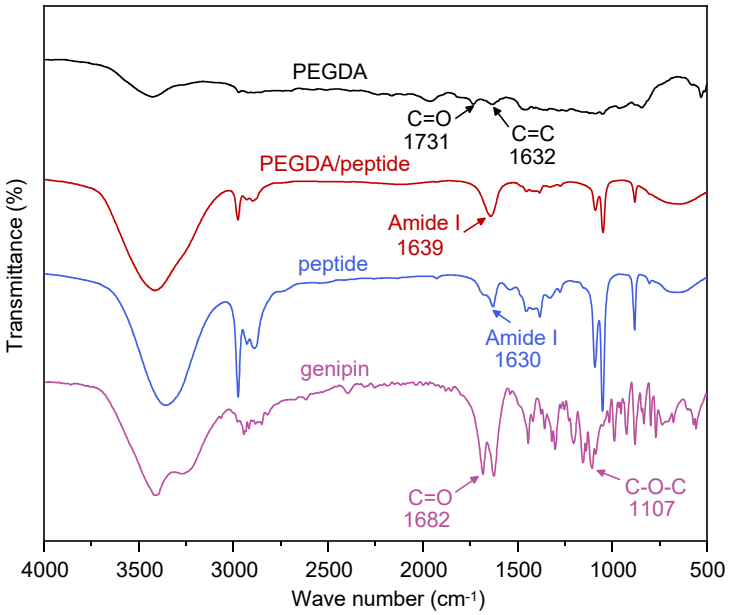


**Supplementary Fig. 2 | FTIR results of the PEGDA monomer, peptide, PEGDA/peptide hydrogel and genipin.** The peaks of C=C bonds (1632 $cm^{-1}$) and C=O bonds (1731 $cm^{-1}$) represent the characteristic absorption bands in PEGDA, and both the peaks become invisible in the PEGDA/peptide hydrogel, due to the UV-induced cross-linking and Michael addition reaction with peptide. Peptide exhibits characteristic absorption peaks of Amide I (C=O stretching vibration, 1630 $cm^{-1}$), which shift to 1639 $cm^{-1}$ in the PEGDA/peptide hydrogel probably due to hydrogen bonding between PEGDA and peptide.

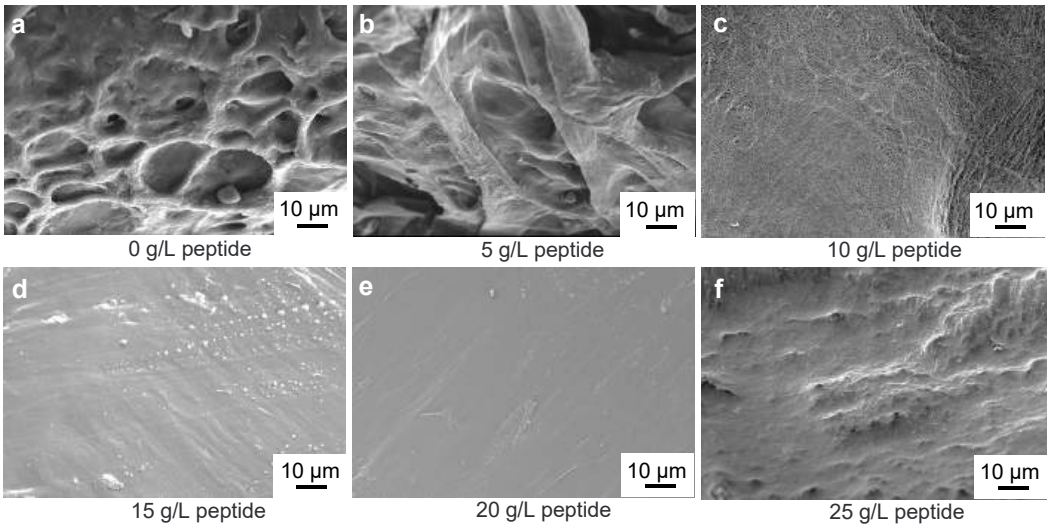


**Supplementary Fig. 3 | Scanning electron microscopy (SEM) images of cross-sections of PEGDA/peptide hydrogel with different peptide concentration.**

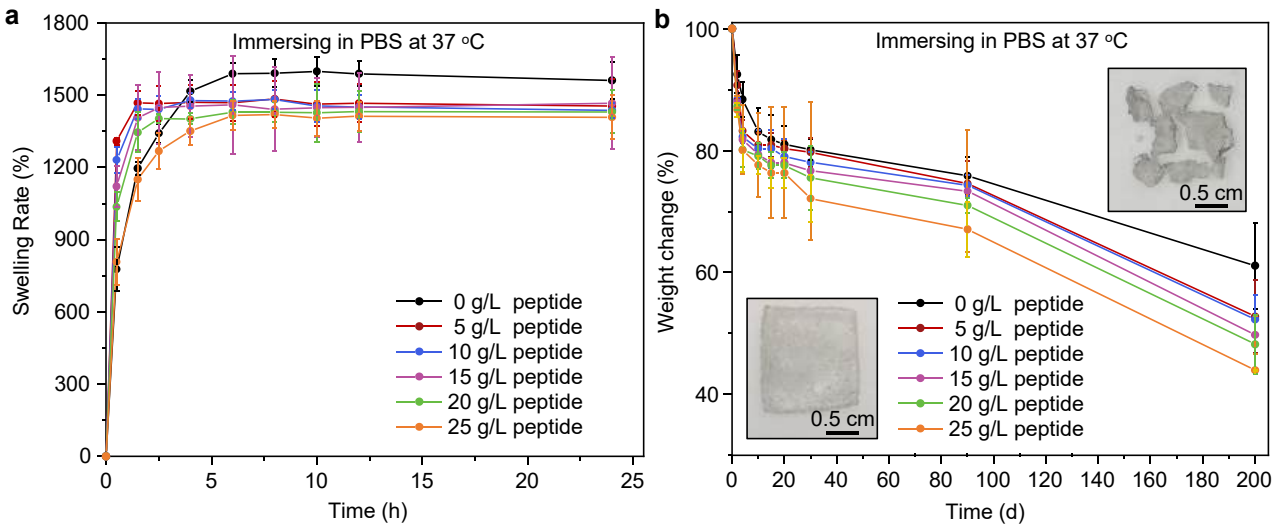


**Supplementary Fig. 4 | Swelling and degradation behavior of the PEGDA/peptide hydrogels with different peptide concentrations as a function of time.** Compared to single-network PEGDA, PEGDA/peptide hydrogels with compact network structure exhibit a lower swelling rate. Moreover, incorporating peptide accelerates overall biodegradation. In **a** and **b**, n = 3 independent samples and data are presented as mean ± SD.

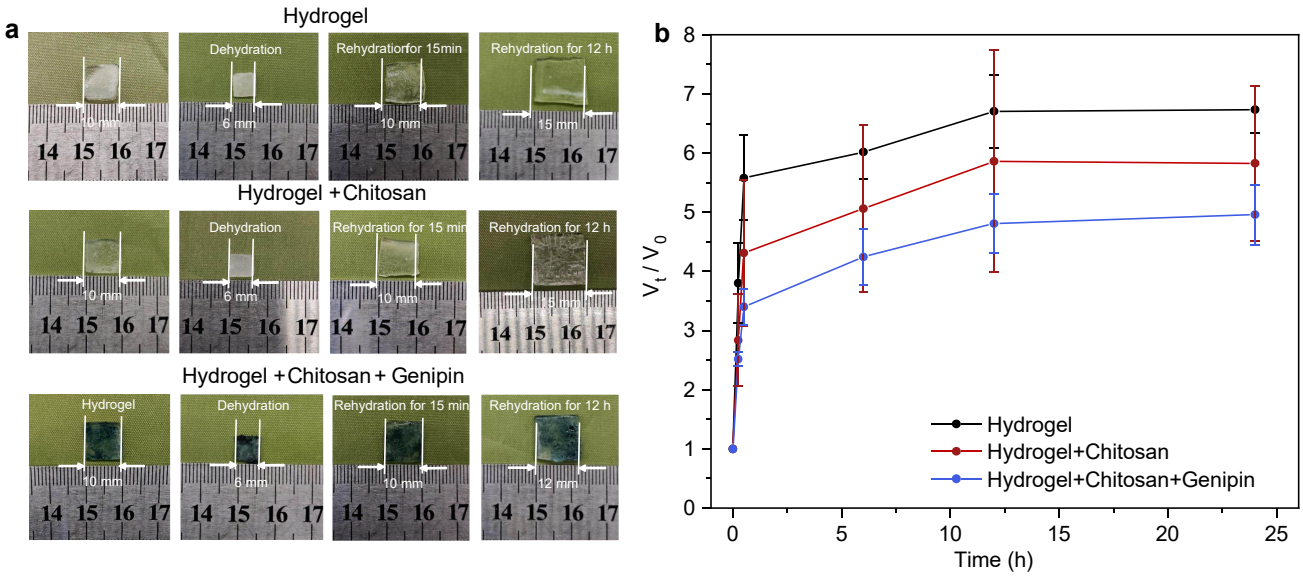


**Supplementary Fig. 5 | Swelling of hydrogels with different surface coating in vitro. a**, Photographs of hydrogel after dehydration and rehydration. **b**, The volume variation of hydrogel with different immersion time in PBS at 25 °C.

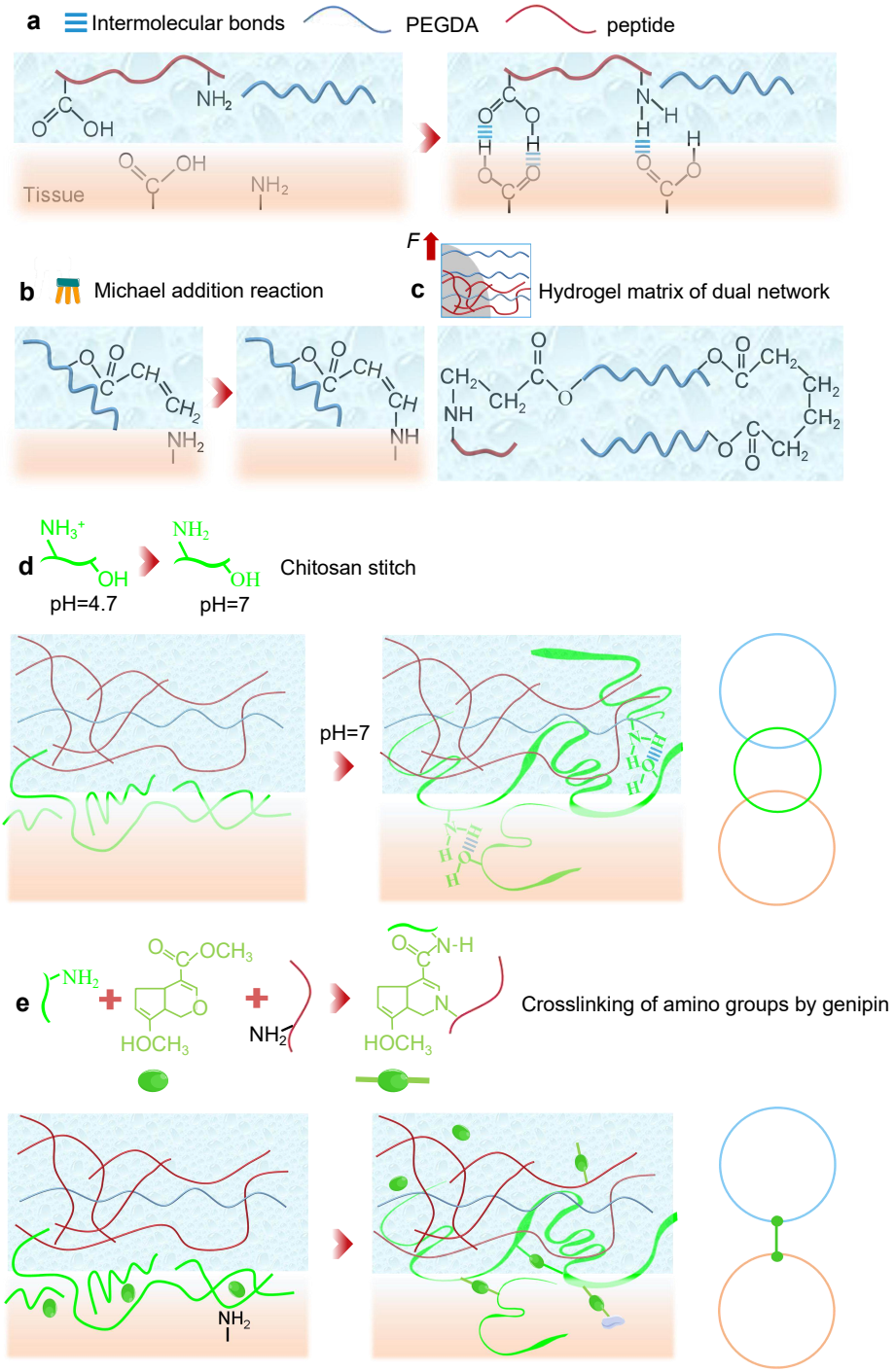


**Supplementary Fig. 6 | Schematic diagrams illustrating the adhesion mechanism of PEGDA/peptide hydrogel.** **a**, Temporary physical crosslinking (intermolecular hydrogen bonds between the amino groups and carboxylic acid groups). **b**, The formation of covalent bonds associated with Michael addition reaction between PEGDA/peptide hydrogels and amine groups on tissues. **c**, Double network of PEGDA/peptide hydrogel matrix enables the dissipation of enormous amount of mechanical energy upon stress. **d**, Bond-stitch topological entanglement at the interface arises from the diffusion of bridging polymer chains (chitosan) into the hydrogel and tissues, and the subsequent formation of the chitosan network. **e**, The crosslinking of amino groups on chitosan chains, peptide chains, and tissues by genipin.

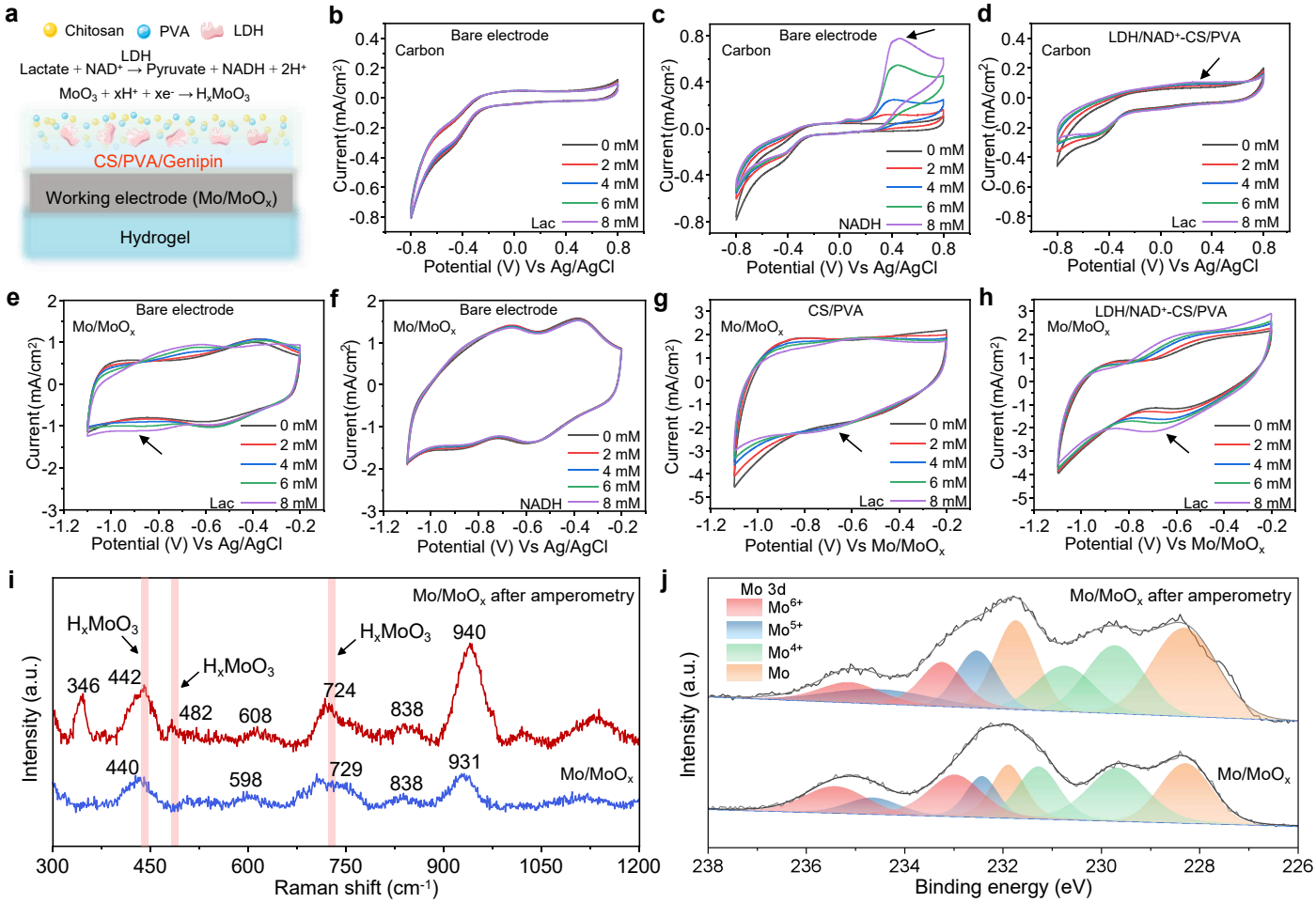


**Supplementary Fig. 7 | Lactate sensing through enzyme-assisted proton-intercalation mechanism based on the Mo/MoO$_x$ electrode. a**, The illustration of the lactate sensing mechanism of Mo/MoO$_x$. **b**–**d**, CV characteristics of conventional carbon electrodes tested in PBS. **b**, Bare carbon electrodes are not responsive to lactate. **c**, NADH oxidation using bare carbon electrodes. **d**, Lactate sensing using LDH/NAD$^+$-CS/PVA modified carbon electrodes, in which signal generation relies on LDH-catalyzed NADH/NAD$^+$ redox reactions. **e**–**h**, CV characteristics of bioresorbable Mo/MoO$_x$ electrodes tested in PBS. **e**, Bare Mo/MoO$_x$ electrodes are intrinsically responsive to lactate through proton-intercalation. **f**, Bare Mo/MoO$_x$ electrodes are not responsive to NADH under reductive potentials. **g**, CS/PVA modified Mo/MoO$_x$ electrodes are weakly responsive to lactate given the passive coating layer. **h**, LDH/NAD$^+$-CS/PVA modified Mo/MoO$_x$ electrodes achieve sensitive lactate response, through enzyme-assisted proton-intercalation. **i**, Raman spectra of Mo/MoO$_x$ electrode surface before and after amperometry for 15 min with lactate additions (2 mM): relative enhanced intensity of bands at 442, 482 and 724 cm$^{-1}$ are associated with H$_x$MoO$_3$, suggesting proton intercalation in MoO$_x$. The bands at 346 and 940 cm$^{-1}$ are associated with $Na_2MoO_4 \cdot 2H_2O$. The bands at 608 and 838 cm$^{-1}$ are ascribed to MoO$_3$. **j**, XPS Mo 3d spectra of Mo/MoO$_x$ electrode surface before and after amperometry for 15 min with lactate additions (2 mM), indicating an increase in the relative proportion of Mo$^{5+}$ and Mo$^{4+}$ species compared with Mo$^{6+}$ components after proton intercalation.

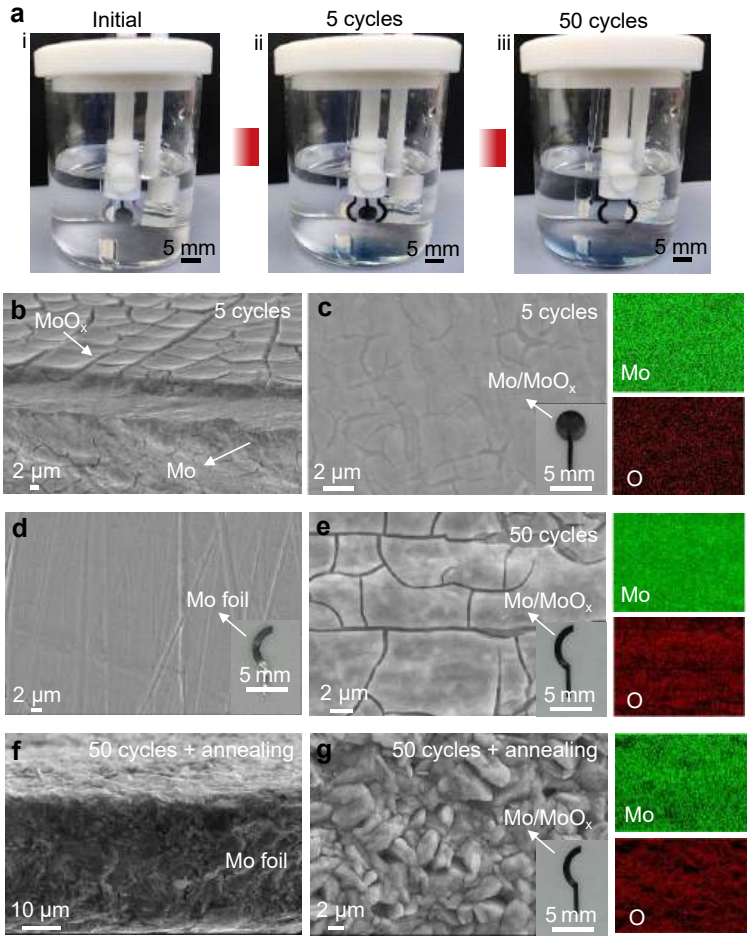


**Supplementary Fig. 8 | Electro-anodization process and the morphological characterization of Mo/$MoO_x$ electrodes. a**, Electro-anodization is achieved by cyclic voltammetry (CV) from 0 V to 0.8 V. 5 cycles of CV is conducted for WE, while 50 cycles of CV is conducted for the CE and RE followed by thermal annealing at 350 $^{o}$C for 3 h to further improve stability. A sufficient oxide layer minimizes potential fluctuations, yielding a more stable reference potential for prolonged sensing. **b**, Cross-sectional SEM image of the Mo/$MoO_x$ WE following 5 CV cycles. **c**, SEM image of the surface morphology of Mo/$MoO_x$ WE following 5 CV cycles, along with energy-dispersive spectroscopy (EDS) elemental mapping. **d**, SEM image of the surface morphology of the polished Mo foil. **e**, SEM image of the surface morphology of Mo/$MoO_x$ electrode after 50 CV cycles, along with EDS elemental mapping. **f**, Cross-sectional SEM image of the Mo/$MoO_x$ electrodes (CE and RE) following 50 CV cycles and subsequent annealing. **g**, SEM image of the surface morphology of the Mo/$MoO_x$ electrodes (CE and RE) following 50 CV cycles and subsequent annealing, along with EDS elemental mapping.

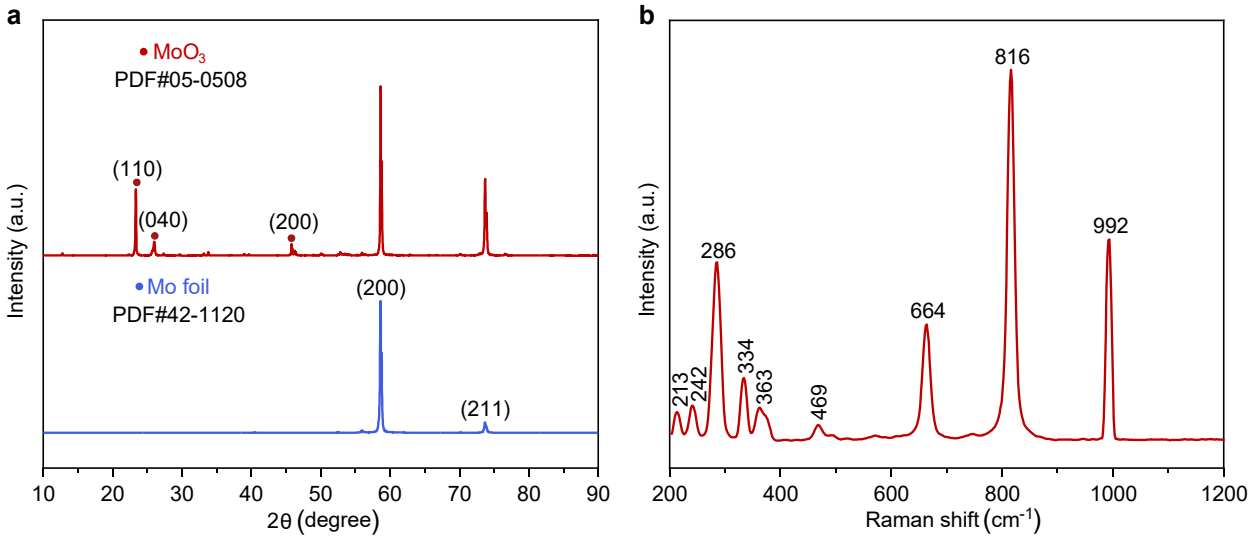


**Supplementary Fig. 9 | X-ray diffraction (XRD) and Raman analysis of the Mo/$MoO_x$ electrodes. a**, XRD pattern of the Mo foil and Mo/$MoO_x$ (RE): Two intense peaks centered at 58.6 and 73.7 ° of the Mo foil can be indexed to the (200), and (211) planes of metallic Mo (PDF#42-1120), respectively. Three additional peaks centered at 23.3 °, 26.0 ° and 45.8 ° of the Mo/$MoO_x$ electrode can be indexed to the (110), (040) and (200) planes of α-$MoO_3$ (PDF#05-0508), respectively. **b**, Raman spectrum of the Mo/$MoO_x$ electrode: The bands at 992 $cm^{-1}$ and 816 $cm^{-1}$ correspond to the asymmetrical and symmetrical stretching vibrations of Mo=O bonds, while the band at 664 $cm^{-1}$ is attributed to the asymmetrical stretching vibration of O-Mo-O bonds. Raman shift peaks correspond to O=Mo=O wagging (286 $cm^{-1}$), O-Mo-O bending (334 $cm^{-1}$) and scissoring (363 $cm^{-1}$) vibration modes for α-$MoO_3$. Peak identification is based on previous reports [1, 2].

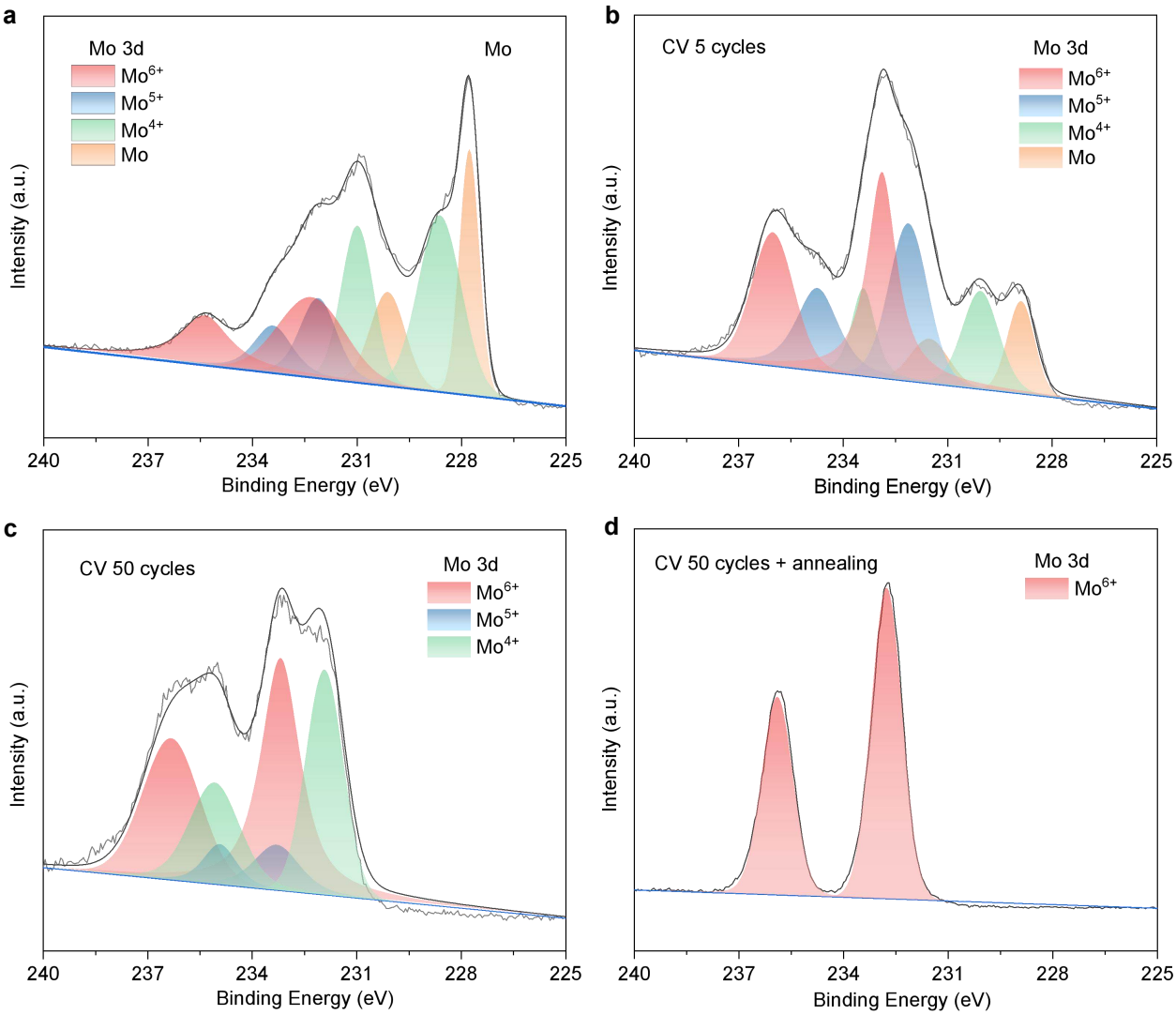


**Supplementary Fig. 10 | XPS spectra of the Mo/$MoO_x$ electrode. a**, XPS analysis on the Mo foil. The spectra exhibit peaks of Mo in the 0-valence state, with two peaks measured at 227.8 eV ($3d_{5/2}$) and 230.1 eV ($3d_{3/2}$), alongside other valence states of Mo, indicating the presence of native surface oxides. **b**, After electro-anodization through 5 cycles of CV, the spectrum shows the most intense duplet located at 232.9 eV ($3d_{5/2}$) and 236 eV ($3d_{3/2}$), corresponding to the binding energies of the $Mo^{6+}$ . Six minor peaks of Mo 3d spectrum originate from lower oxidation states of Mo, which are ascribed to $Mo^{5+}$ (232 and 234.75 eV), $Mo^{4+}$ (230.1 and 233.4 eV), and metallic $Mo^{0}$ (228.9 and 231.6 eV). **c**, After electro-anodization through 50 cycles of CV, prominent peaks are observed at 233.2 eV ($3d_{5/2}$) and 236.35 eV ($3d_{3/2}$), corresponding to the binding energies of the $Mo^{6+}$ state, while peaks corresponding to Mo in the 0-valence state disappear, indicating thicker $MoO_x$ layer. **d**, Following electro-anodization and thermal annealing, remaining peaks located at 232.8 eV and 235.9 eV is well matched with Mo $3d_{5/2}$ and Mo $3d_{3/2}$ in the $Mo^{6+}$ oxidation state. Peak identification is based on previous reports [1, 3].

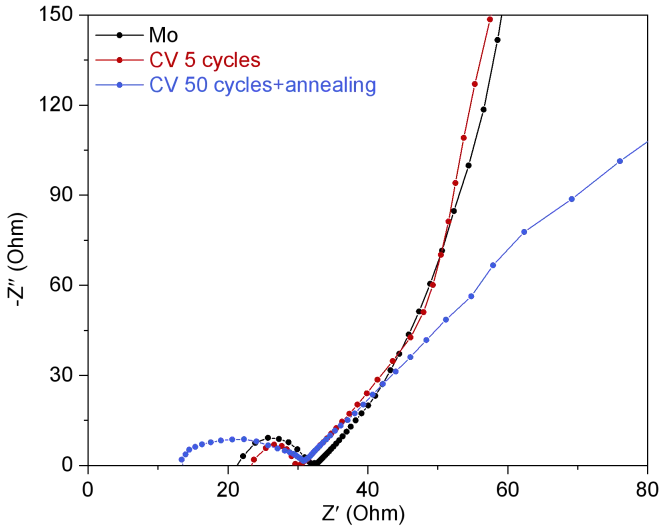


**Supplementary Fig. 11 | Electrochemical impedance spectroscopy (EIS) measurements of the Mo foil and Mo/$MoO_x$ electrodes in PBS.**

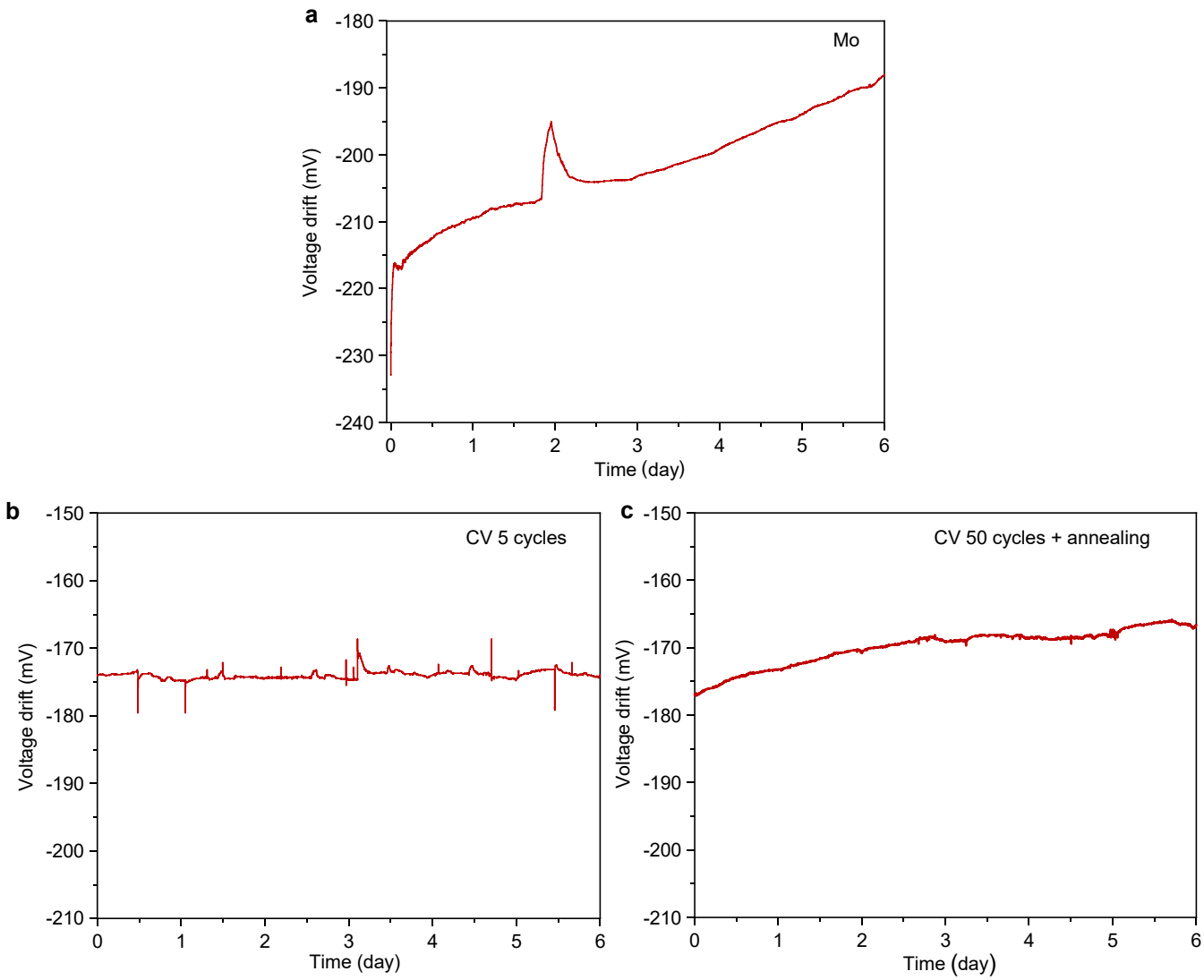


**Supplementary Fig. 12 | Long-term evaluation of electrochemical stability based on open circuit potential (OCP) measurement. a**, Mo foil. **b**, Mo/$MoO_x$ after 5 CV cycles. **c**, Mo/$MoO_x$ after 50 CV cycles followed by thermal annealing. OCP is measured in PBS over 6 days against a commercial Ag/AgCl RE. The OCP change of the Mo/$MoO_x$ electrodes (~ 11 mV) over 6 days is significantly smaller than that of the Mo electrode (~ 45 mV), indicating improved electrochemical stability by the $MoO_x$ coating.

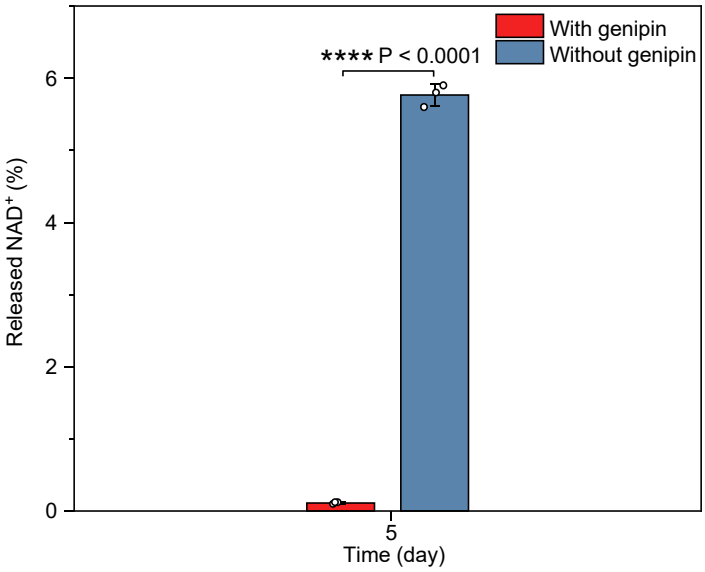


**Supplementary Fig. 13 | $NAD^+$ release from the PVA/chitosan hydrogel layer on the working electrode, with and without genipin crosslinker, after immersion in PBS at 37 °C for 5 days.** The statistical analysis is based on the t-test of independent samples (two-sided). ****P < 0.0001. n = 3 independent samples and data are presented as mean ± SD.

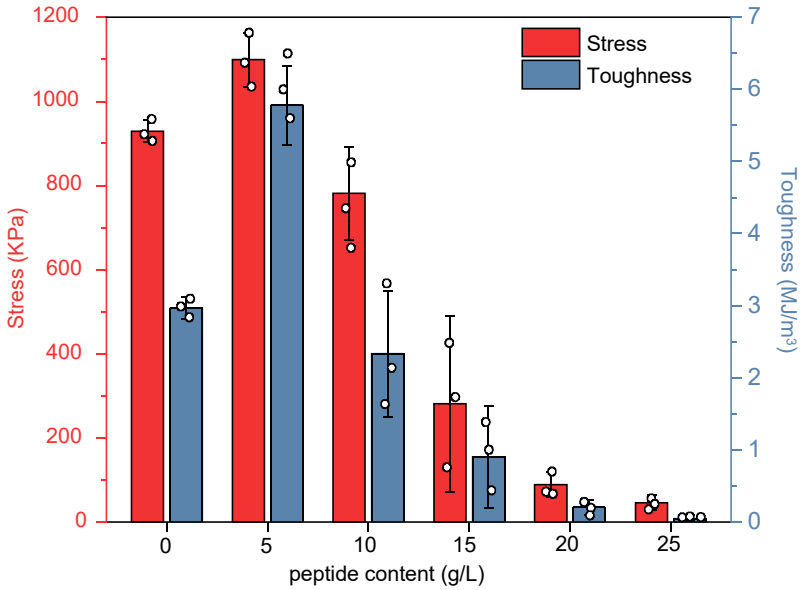


**Supplementary Fig. 14 | Tensile stress and toughness of the PEGDA/peptide hydrogel with different peptide concentrations.** n = 3 independent samples and data are presented as mean ± SD.

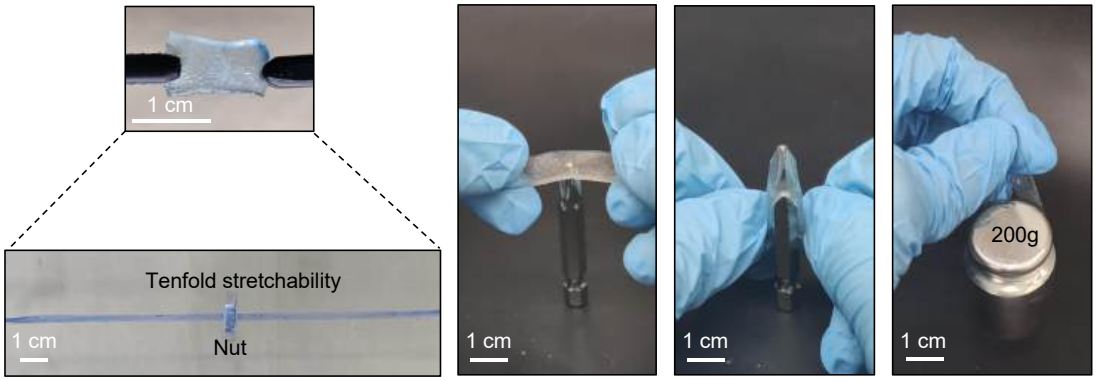


**Supplementary Fig. 15 | Exhibition of excellent mechanical properties of PEGDA/peptide hydrogel, including stretching, stabbing and loading.**

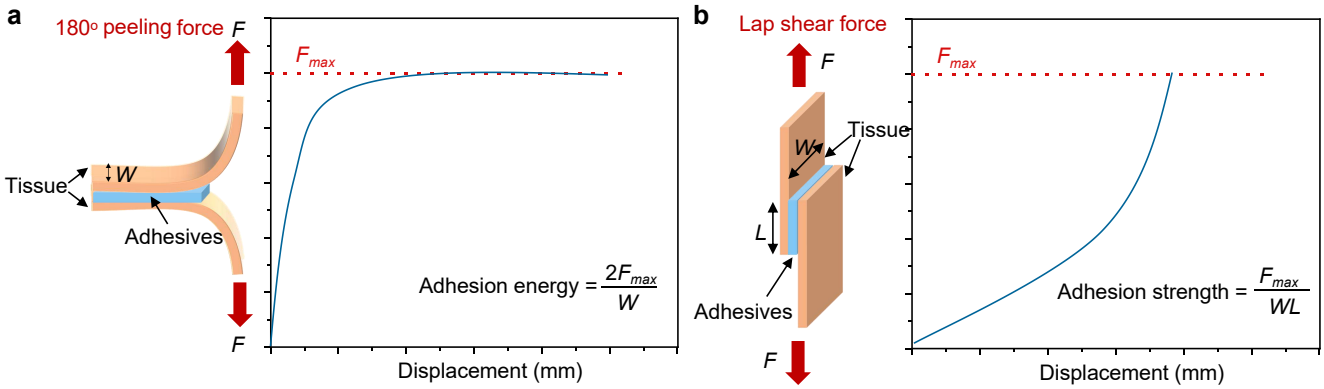


**Supplementary Fig. 16 | Schematic illustration of tissue-hydrogel-tissue sandwich structure for 180° peeling and lap shear measurements.** One side of the tissues is glued to a rigid plastic film as a backing layer and two free arms of the sandwich structure are stretched with an Instron machine to evaluate adhesion energy and strength. **a**, Adhesion energy is defined as twice the plateau force per unit width required for extension during steady-state crack propagation (red dashed line). **b**, Adhesion strength is defined as the maximum force per unit area required for extension, measured up to the point where a preexisting crack begins to propagate. The evaluation methods of adhesion energy and adhesion strength through 180° pealing tests and lap shear tests are similar to previous reports [4].

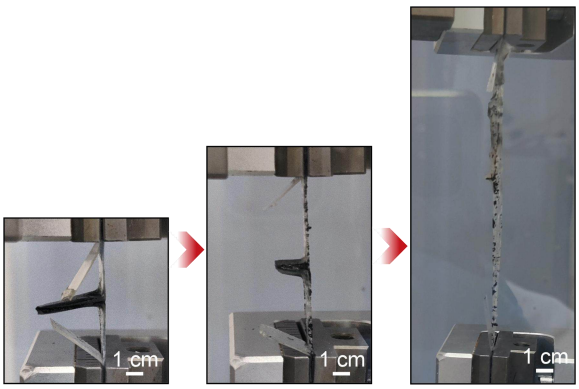


**Supplementary Fig. 17 | The 180° peeling tests of the adhered PEGDA/peptide hydrogel with bridging agents.** Wet adhesion between hydrogel/hydrogel interfaces is performed by spreading a chitosan-based bridging polymer solution with genipin onto the hydrogel surface, followed by the application of another hydrogel film.

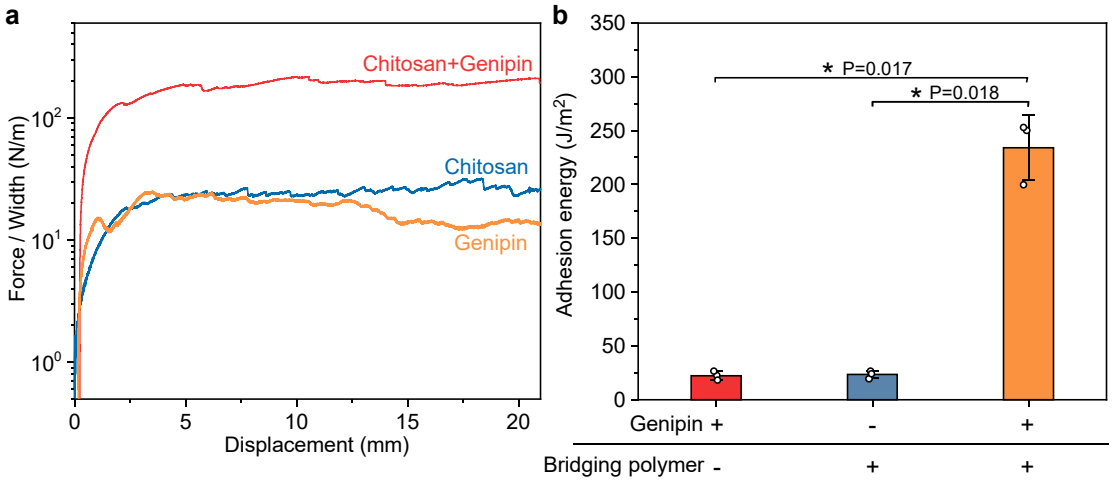


**Supplementary Fig. 18 | Effects of bridging polymer chitosan and genipin on adhesion energy.** Chitosan and genipin were used as the bridging polymer and coupling reagents, respectively. Adhesion energy was calculated based on the average value of force/width at the plateau. **a**, Force-extension curves of peeling tests. **b**, Measured adhesion energy between two PEGDA/peptide hydrogels. The use of genipin or bridging polymer alone yields adhesion energies of 22.3 ± 4.1 J $m^{-2}$ and 23.3 ± 3.5 J $m^{-2}$, respectively, which is much smaller than that of the use of both genipin and chitosan 234.3 ± 30.0 J/$m^2$. n = 3 independent samples and data are presented as mean ± SD. In **b**, the statistical analysis is based on the one-way ANOVA and Tamhane post-hoc comparison (two-sided). *P < 0.05. n = 3 independent samples and data are presented as mean ± SD.

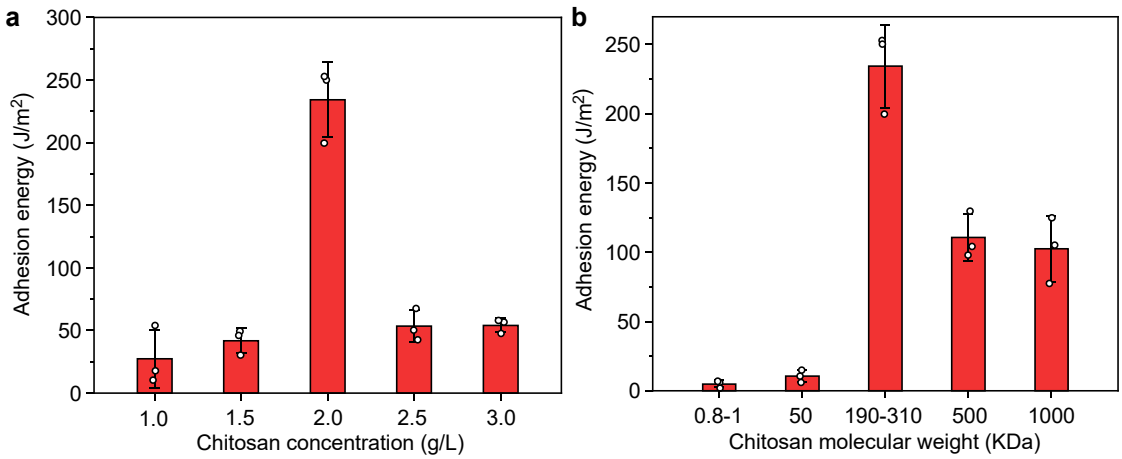


**Supplementary Fig. 19 | Effects of concentration and molecular weight of chitosan on adhesion energy.** Bridging polymer (chitosan) is applied onto a PEGDA/peptide hydrogel, followed by 180° peeling tests. **a**, Effects of chitosan concentration on adhesion energy. **b**, Effects of molecular weight of chitosan on adhesion energy. Moderate increases in concentration raise bridging density, boosting adhesion, whereas excessive concentrations cause chain entanglement at the hydrogel surface, hindering polymer diffusion and reducing adhesion. Medium-viscosity chitosan (190 – 310 kDa) achieves the highest adhesion by balancing diffusion and bridging. Low-viscosity chitosan penetrates too readily into the hydrogel, diminishing bridging, while high-viscosity chitosan forms surface entanglements that impeded diffusion. n = 3 independent samples and data are presented as mean ± SD.

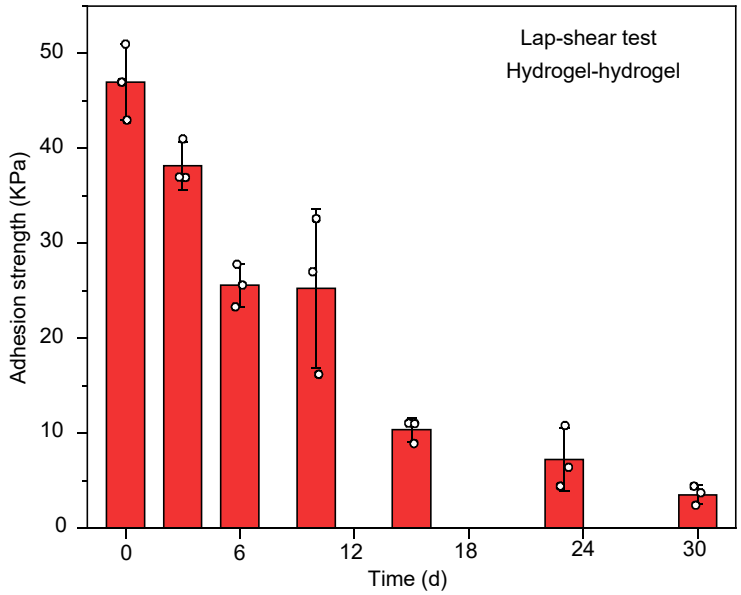


**Supplementary Fig. 20 | Adhesion strength of PEGDA/peptide hydrogels. a**, Adhesion strength between two hydrogels with a bridging polymer in DI water at room temperature over time. n = 3 independent samples and data are presented as mean ± SD.

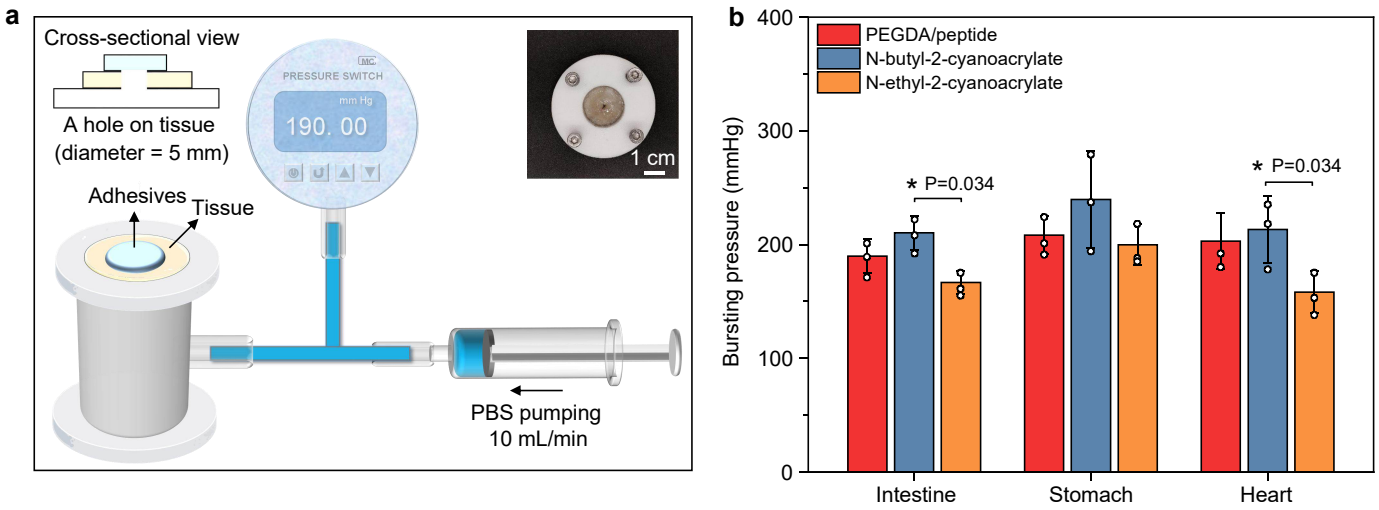


**Supplementary Fig. 21 | Evaluation of bursting pressure.** **a**, Schematic illustration of the experimental set-up for measuring bursting pressure. **b**, Bursting pressure of intestine, stomach and heart sealed by different adhesives. Tissues sealed with PEGDA/peptide hydrogel exhibit bursting pressure comparable to that of commercial biomedical adhesives. For **b**, the statistical analysis is based on the one-way ANOVA and LSD (least significant difference) post-hoc comparison (two-sided). *P < 0.05. n = 3 independent samples and data are presented as mean ± SD.

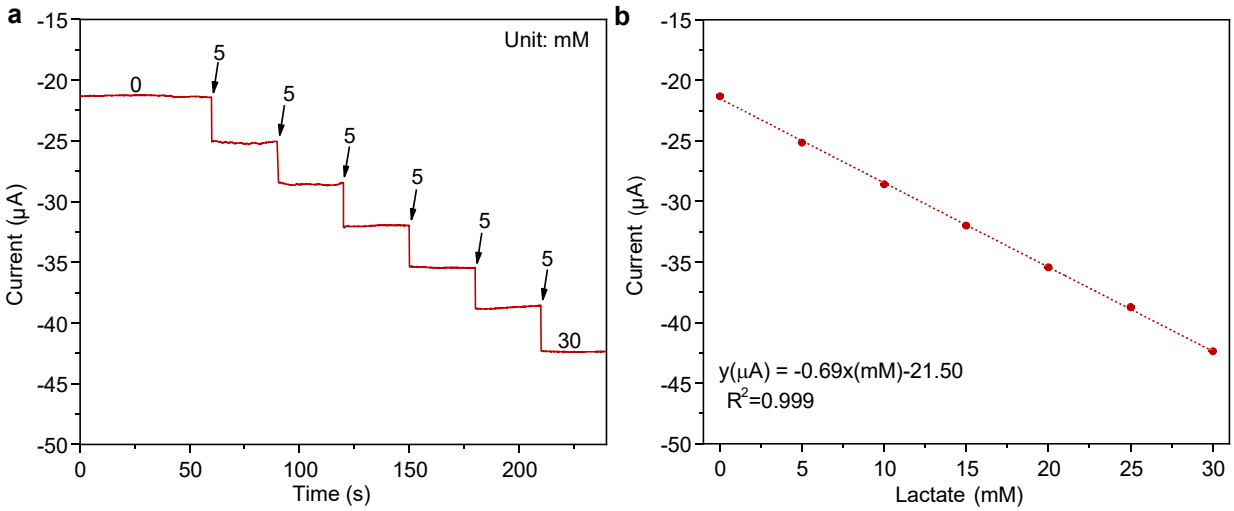


**Supplementary Fig. 22 | Quantification of the bioresorbable lactate sensor. a**, Time-dependent current response of the lactate sensor at different lactate concentrations (detection range: 0–30 mM), at a bias voltage of -0.65 V. **b**, Calibration curve: linear relationship between response currents and lactate concentrations (0–30 mM).

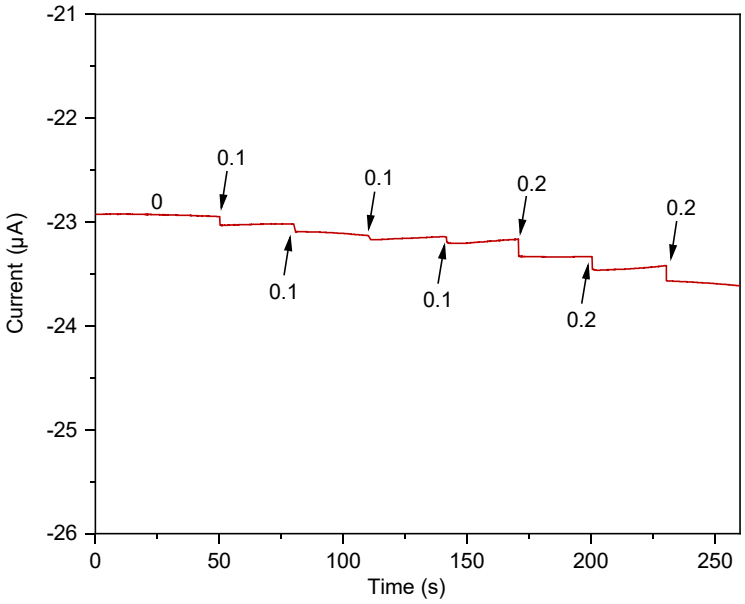


**Supplementary Fig. 23 | Quantification of the bioresorbable lactate sensor.** Time-dependent current response of the lactate sensor at different lactate concentrations (detection range: 0–1 mM), at a bias voltage of -0.65 V.

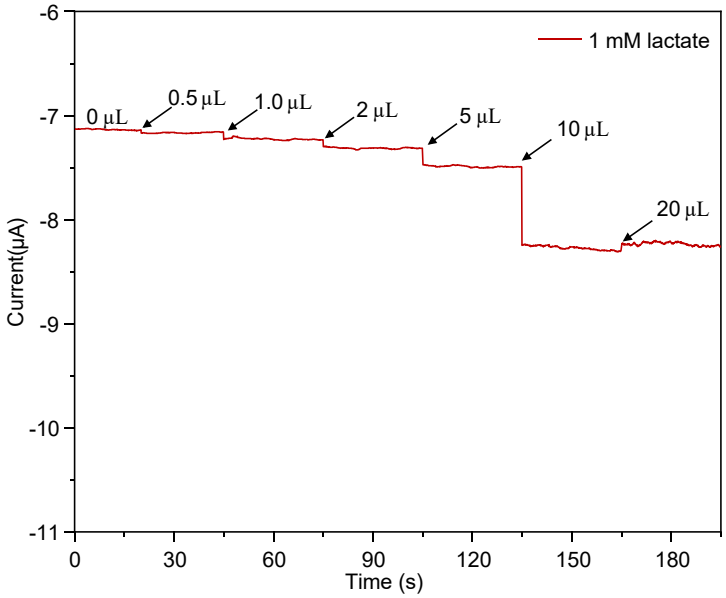


**Supplementary Fig. 24 | Current response of the bioresorbable lactate sensor to different volumes of 1 mM lactate solution.**

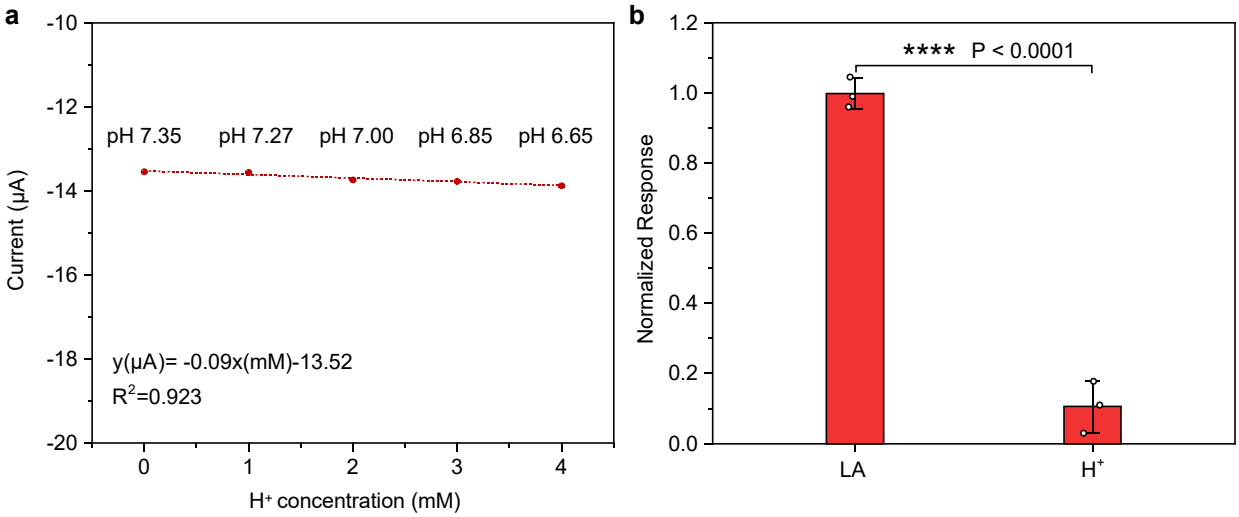


**Supplementary Fig. 25 | The influence of pH on the current response of the bioresorbable sensor. a**, Calibration curve: linear relationship between the response current and $H^+$ concentrations. **b**, Normalized current response of the lactate sensor, with the addition of lactate (1 mM) and hydrochloric acid (HCl) (1 mM). The statistical analysis is based on the t-test of independent samples (two-sided). ****P < 0.0001. n = 3 independent samples and data are presented as mean ± SD.

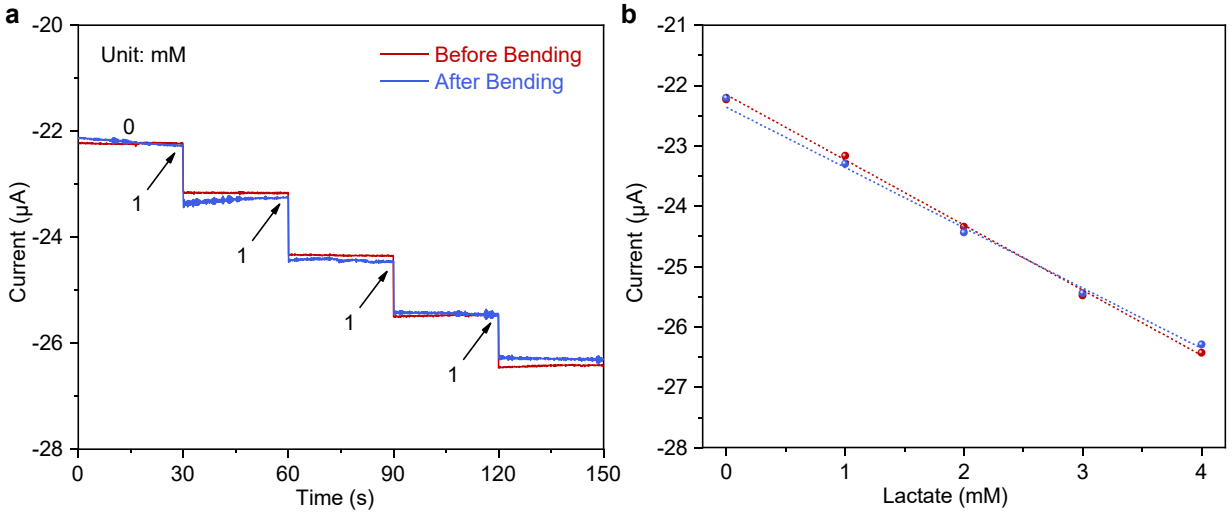


**Supplementary Fig. 26 | Mechanical robustness of the bioresorbable lactate. a**, Time-dependent current response of the lactate sensors (before and after bending) at different lactate concentrations (detection range: 0 – 4 mM), at a bias voltage of -0.65 V. **b**, Calibration curve: linear relationship between the sensor ' s response currents (before and after 300 bending cycles) and lactate concentrations.

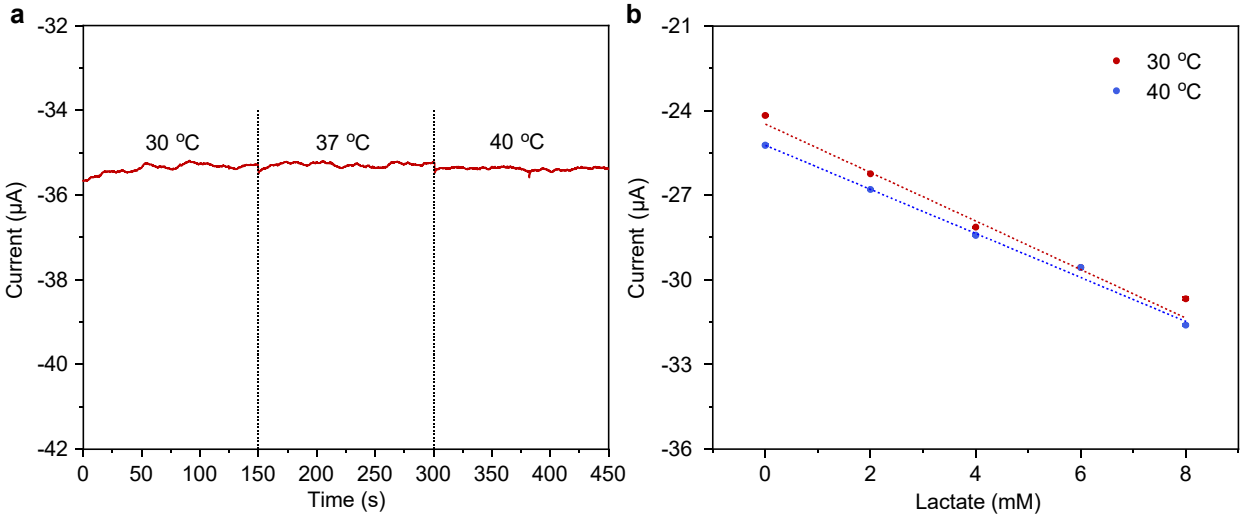


**Supplementary Fig. 27 | The influence of temperature on the current response of the bioresorbable sensor. a**, Current response to lactate (1 mM) measured at 30 °C, 37 °C and 40 °C. **b**, Calibration curve: linear relationship between the response current and lactate concentration at 30 °C and 40 °C.

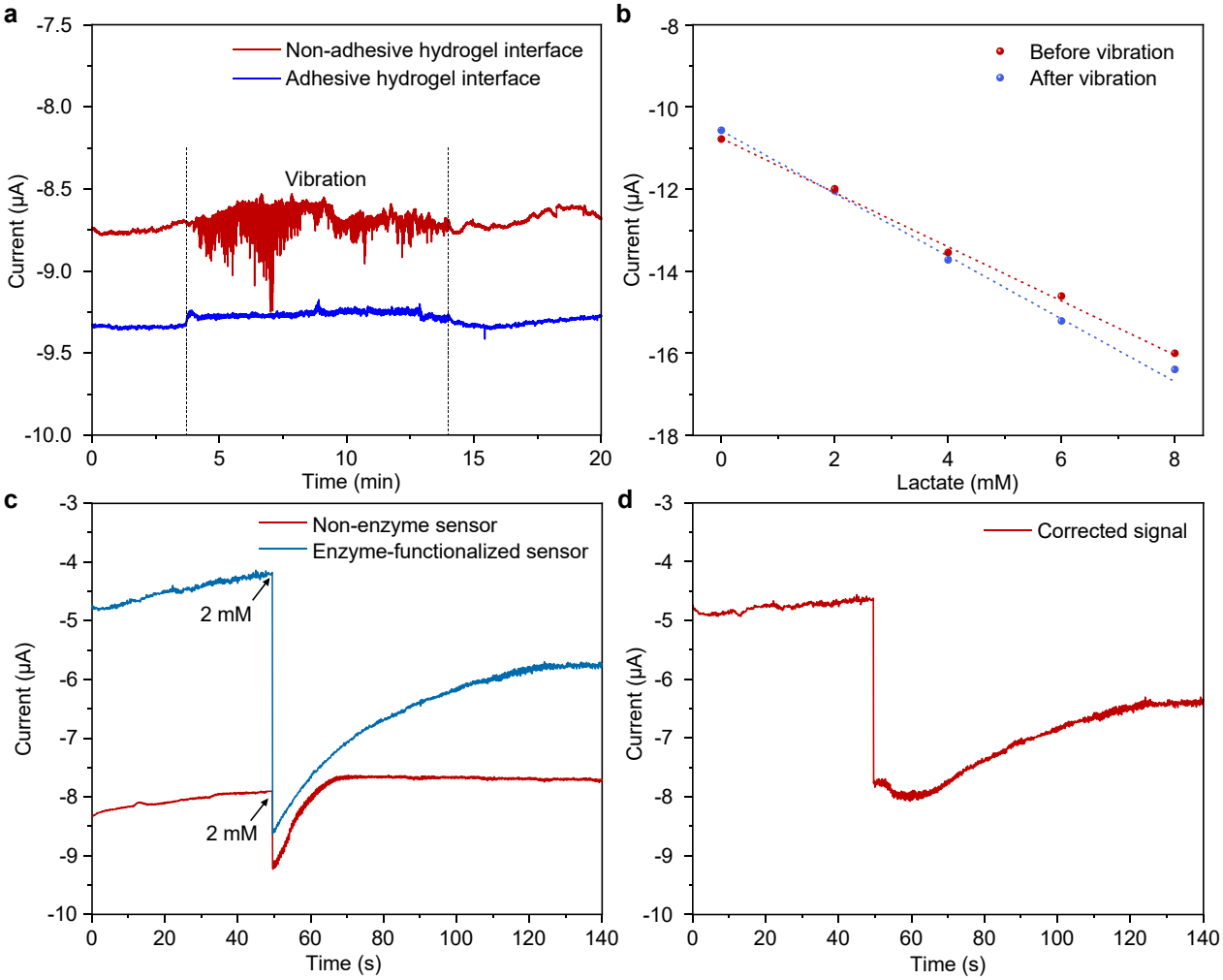


**Supplementary Fig. 28 | The influence of mechanical motion on the current response of the bioresorbable sensor. a**, Influence of motion on the base current response of the bioresorbable lactate sensor. An in vitro heart-motion simulator is used to introduce vibration. The adhesive hydrogel interface incorporating chitosan–genipin bridging polymers exhibits lower noise than the non-adhesive hydrogel interface. **b**, Calibration curve: linear relationship between the response current and lactate concentration before and after 10000 cycles of vibration. **c**, Current responses to lactate (2 mM) of non-enzyme and enzyme-functionalized sensors. **d**, Corrected current signal by referencing the enzyme-functionalized (LDH/$NAD^+$) sensor to the non-enzyme functionalized sensor, which can further reduce the influence of motion artifacts and improve signal specificity.

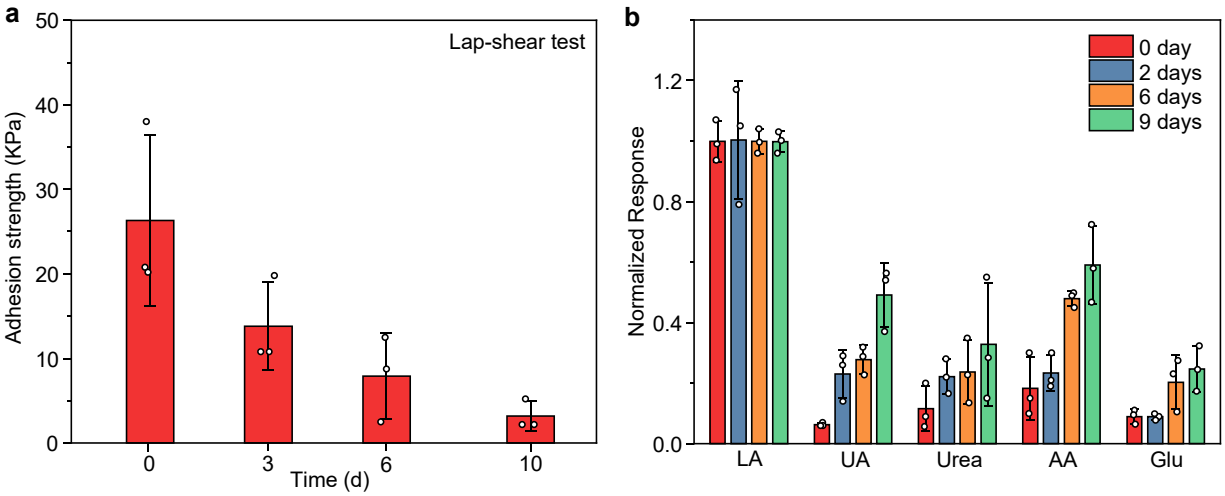


**Supplementary Fig. 29 | a,** Adhesion strength between the lactate sensor with an adhesive hydrogel substrate and pig heart tissues over varying soaking times in deionized (DI) water at 25 °C, using chitosan and genipin as the bridging polymers. **b,** Stability of the lactate sensor: selectivity measurement from day 0 to day 9 in PBS at 37 °C.

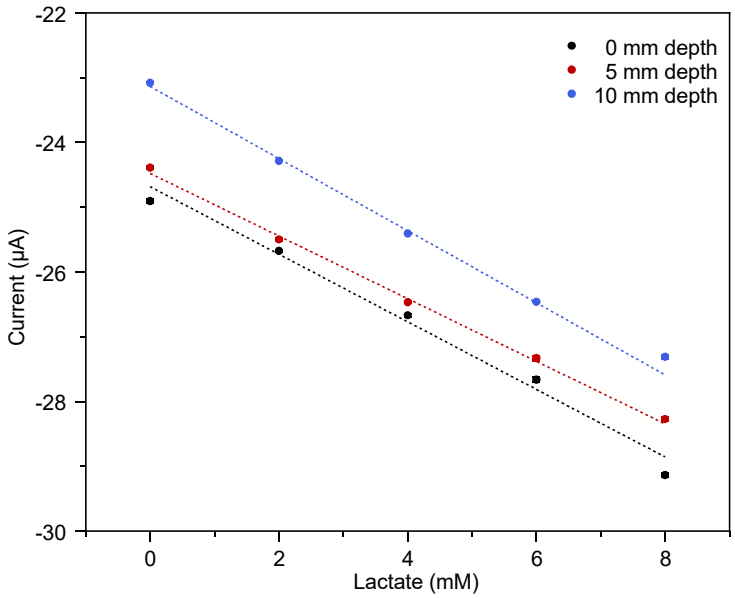


**Supplementary Fig. 30 | Calibration curve: linear relationship between the response current and lactate concentration at tissue depth of 0, 5 and 10 mm.**

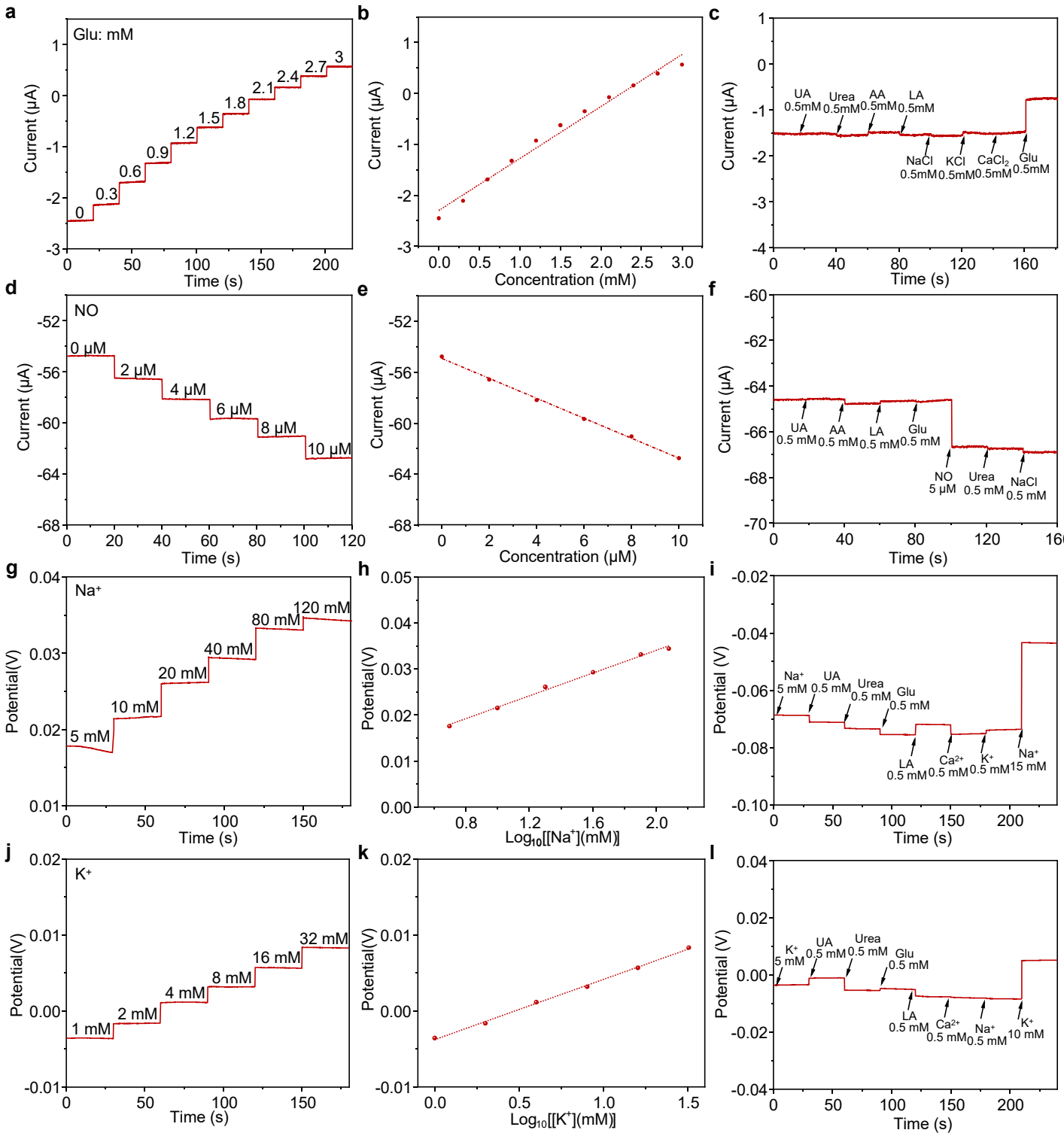
a
Glu: mM
0
0.3
0.6
0.9
1.2
1.5
1.8
2.1
2.4
2.7
3
Current (μA)
Time (s)
b
Current (μA)
Concentration (mM)
c
UA 0.5mM
Urea 0.5mM
AA 0.5mM
LA 0.5mM
NaCl 0.5mM
KCl 0.5mM
CaCl2 0.5mM
Glu 0.5mM
Current (μA)
Time (s)
d
NO
0 μM
2 μM
4 μM
6 μM
8 μM
10 μM
Current (μA)
Time (s)
e
Current (μA)
Concentration (μM)
f
UA 0.5 mM
AA 0.5 mM
LA 0.5 mM
Glu 0.5 mM
NO 5 μM
Urea 0.5 mM
NaCl 0.5 mM
Current (μA)
Time (s)
g
Na+
5 mM
10 mM
20 mM
40 mM
80 mM
120 mM
Potential(V)
Time (s)
h
Potential(V)
Log10[[Na+](mM)]
i
Na+ 5 mM
UA 0.5 mM
Urea 0.5 mM
Glu 0.5 mM
LA 0.5 mM
Ca2+ 0.5 mM
K+ 0.5 mM
Na+ 15 mM
Potential (V)
Time (s)
j
K+
1 mM
2 mM
4 mM
8 mM
16 mM
32 mM
Potential(V)
Time (s)
k
Potential(V)
Log10[[K+](mM)]
l
K+ 5 mM
UA 0.5 mM
Urea 0.5 mM
Glu 0.5 mM
LA 0.5 mM
Ca2+ 0.5 mM
Na+ 0.5 mM
K+ 10 mM
Potential (V)
Time (s)

**Supplementary Fig. 31 | The bioresorbable sensing strategy based on Mo/$MoO_x$ electrodes can be extended to other analytes with appropriate functionalization.** **a**, Time-dependent current response of the bioresorbable glucose sensor with PEGDE/TH/GDH-FAD sensing layer at different glucose concentrations (detection range: 0−3 mM), at a bias voltage of 0 V. **b**, The corresponding calibration plots of the glucose sensor. **c**, Selectivity measurement of the glucose sensor. **d**, Time-dependent current response of the nitric oxide (NO) sensor with CHI/Hemoglobin/PVA/BSA sensing layer at different NO concentrations (detection range: 0−10 μM), at a bias voltage of -0.9 V. **e**, The corresponding calibration plots of the NO sensor. **f**, Selectivity measurement of the NO sensor. **g**, OCP responses of the $Na^+$ sensor with Na ionophore X/Na-TFPB/PVC/DOS/THF ion-selective membrane (ISM) at different $Na^+$ concentrations (detection range: 5–120 mM). **h**, The corresponding calibration plots of the $Na^+$ sensor. **i**, Selectivity measurement of the $Na^+$ sensor. **j**, OCP responses of the bioresorbable $K^+$ sensor with valinomycin/NaTPB/PVC/DOS/THF ISM at different $K^+$ concentrations (detection range: 1–32 mM). **k**, The corresponding calibration plots of the $K^+$ sensor. **l**, Selectivity measurement of the $K^+$ sensor.

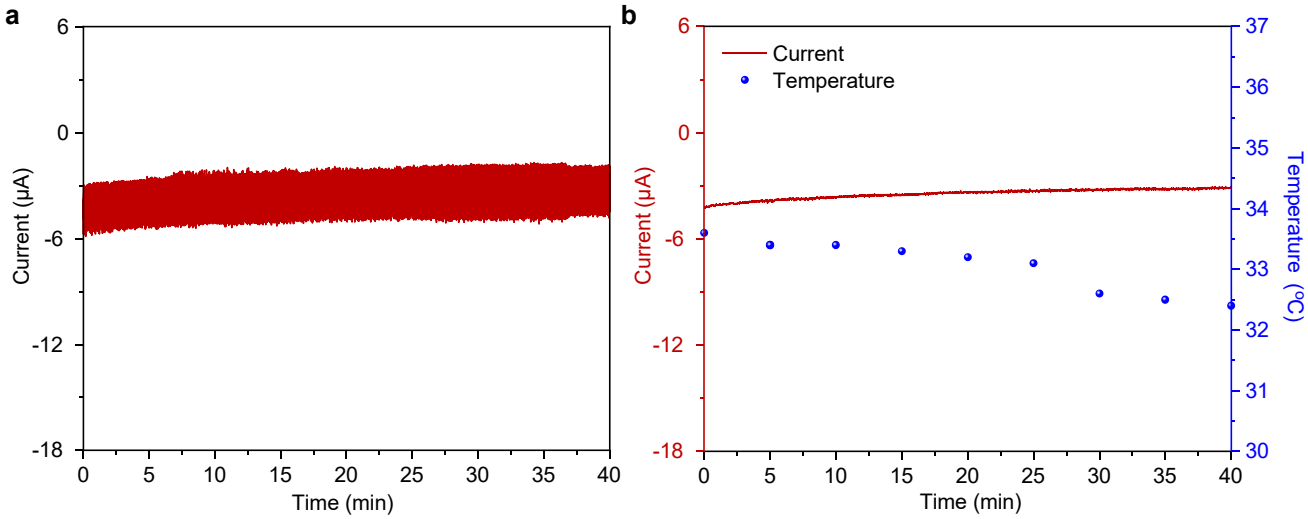


**Supplementary Fig. 32 | The influence of temperature on the current response of the bioresorbable sensor. a**, Original base current signals measured at the pericardial cavity of New Zealand rabbits, demonstrating potential noise arising from heartbeats. **b**, Filtered base current signals using low-pass filtering and LOWESS smoothing and recorded in vivo temperature over time. The level of motion artifacts depends on the intimacy of the device-tissue interface and the beating amplitude, and application of low-pass filtering and LOWESS smoothing effectively attenuates motion artifacts. Signal drift due to heart motion is not significant.

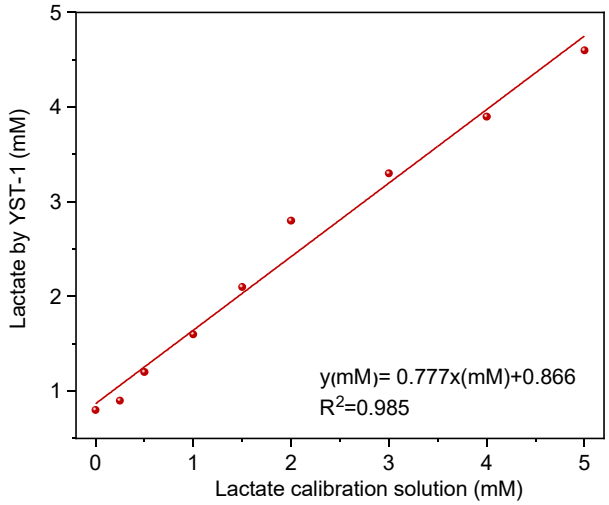


**Supplementary Fig. 33 | Calibration curve: linear relationship between lactate concentrations measured by commercial lactate detector (YST-1) and lactate calibration solution (0–5 mM).**

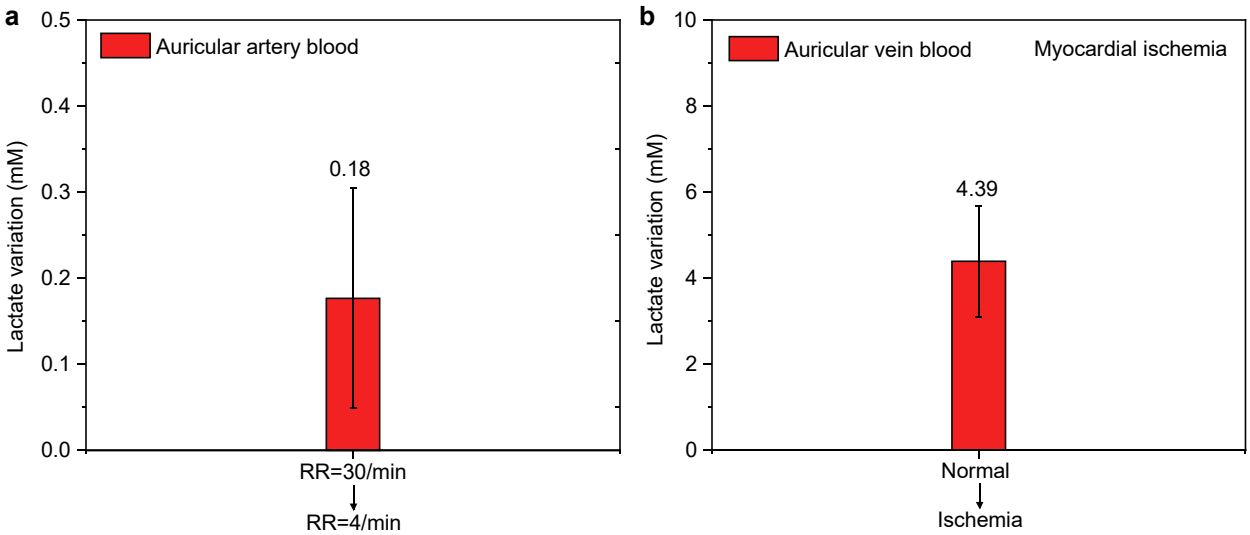


**Supplementary Fig. 34 | Lactate variation of New Zealand rabbits measured by the blood gas analyzer (300-G). a**, Recorded lactate levels in the auricular artery at varying respiration rates (RR). **b**, Recorded lactate levels in the auricular artery during myocardial ischemia. In **a**–**b**, n = 3 independent samples and data are presented as mean ± SD.

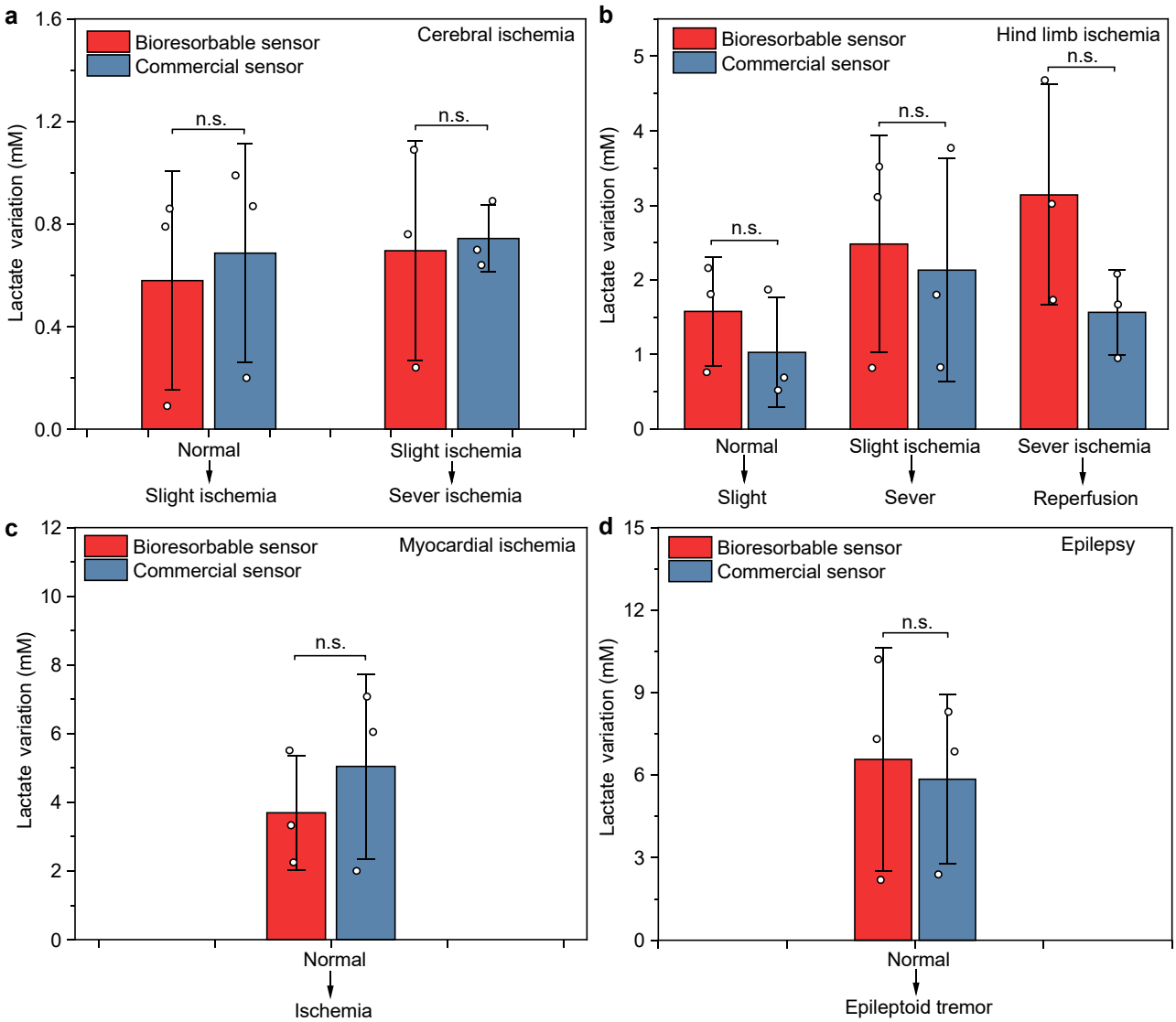


**Supplementary Fig. 35 | Comparison of lactate variation measured by the bioresorbable lactate sensor and the commercial lactate sensor (YST-1) during ischemia and epilepsy.** **a**, Measurement on the dura mater during cerebral ischemia. **b**, Measurement on the thigh muscle during hindlimb ischemia. **c**, Measurement in the pericardial cavity during myocardial ischemia. **d**, Measurement on the cortical surface during epilepsy. In **a**–**d**, the statistical analysis is based on the t-test of independent samples (two-sided). n.s. (not significant). Data are presented as mean ± SD.

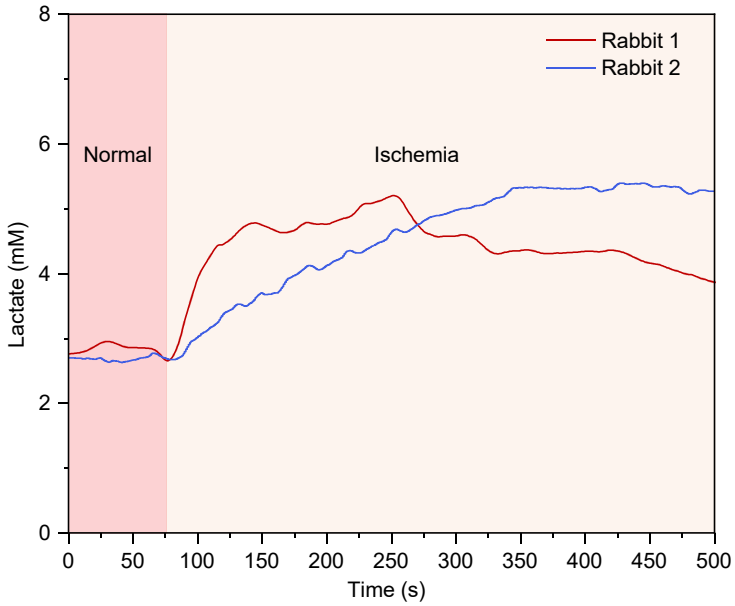


**Supplementary Fig. 36 | Real-time current response of pericardial lactate during myocardial ischemia.** Recorded current by two different bioresorbable lactate sensors on two New Zealand rabbits. The trace in Fig. 3m is included as Rabbit 1 to illustrate variability across animals.

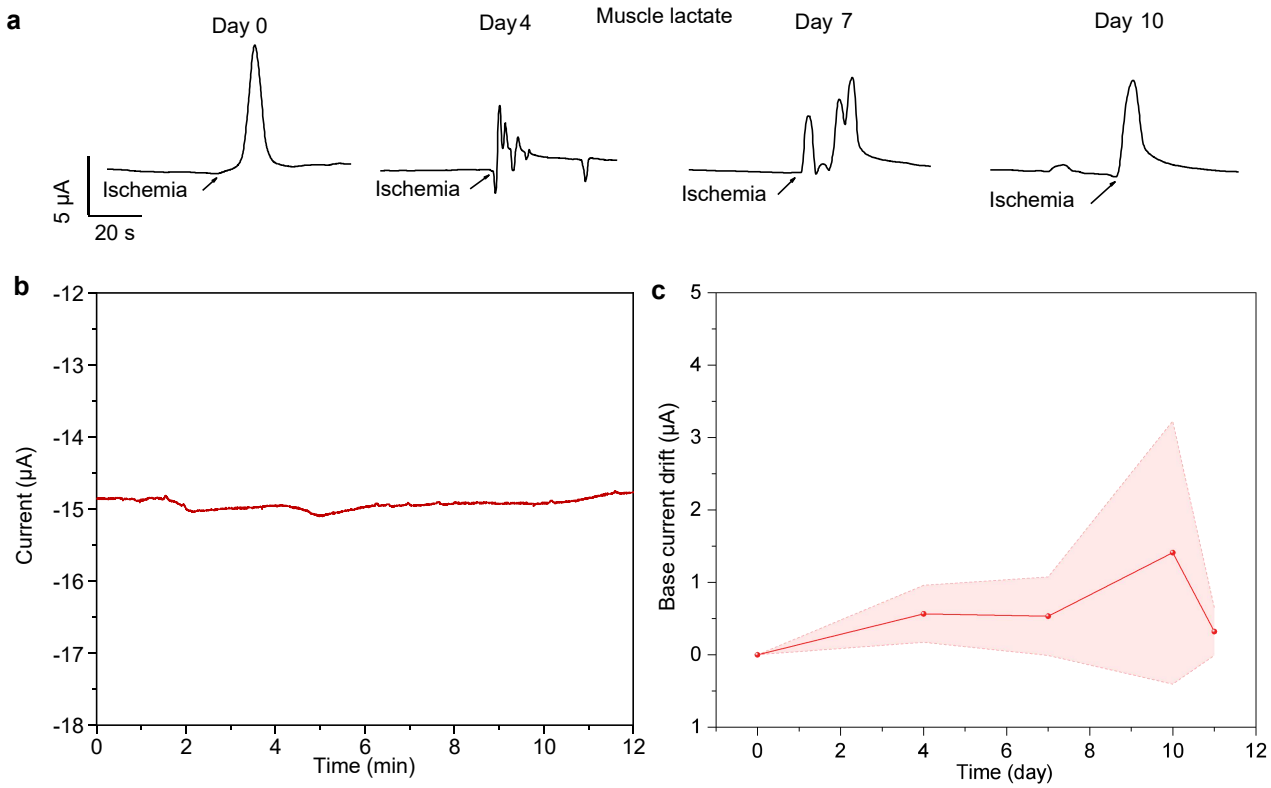


**Supplementary Fig. 37 | Lactate sensing in the thigh muscle of SD rats using a bioresorbable sensor. a**, Lactate current response of rats during hind limb ischemia on days 0, 4, 7 and 10. Current spikes are associated with ligation procedure and rapidly returns to a stable level thereafter, revealing the underlying lactate dynamics. **b**, Base current monitored over a 12-min period. **c**, Base current drift monitored over 11 days of implantation. In **a–c**, n = 3 independent experiments.

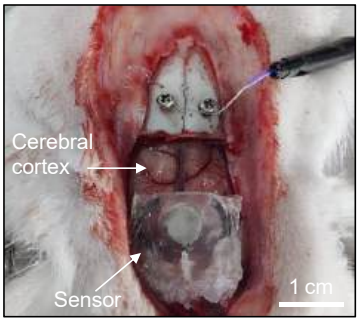


**Supplementary Fig. 38 | Surgical operation of sensor implantation on the rabbit brain.**

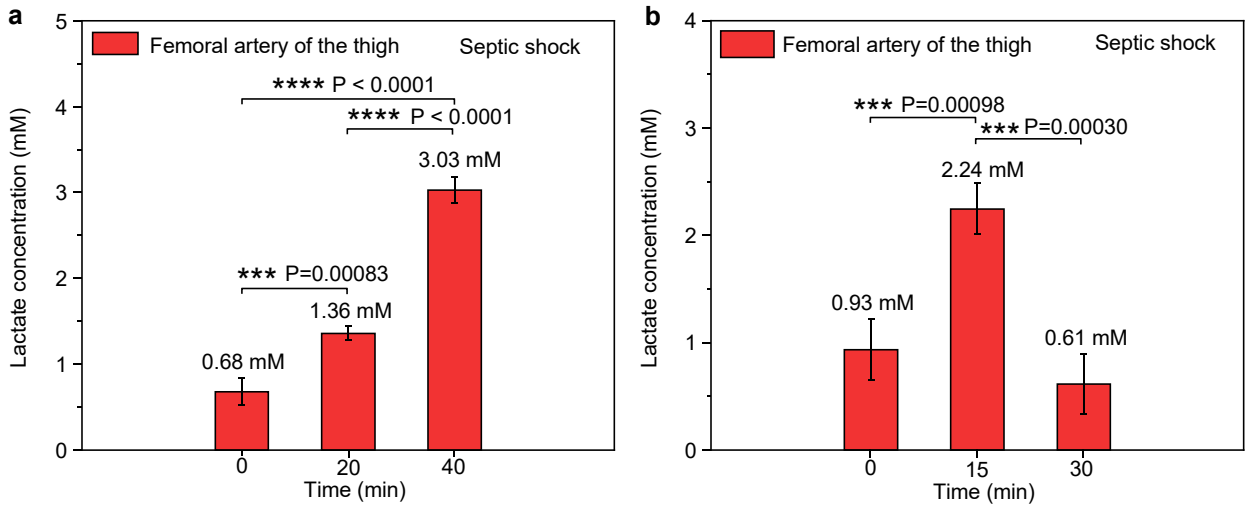


**Supplementary Fig. 39 | Lactate concentration of New Zealand rabbits measured by the blood gas analyzer (300-G). a**, Recorded lactate levels in the femoral artery of the thigh during septic shock without fluid resuscitation (FR). Lactate levels are obtained by calibrating with blood lactate baseline. **b**, Recorded lactate levels in the femoral artery of the thigh during septic shock, with FR initiated after a 25% decrease in mean arterial pressure (MAP). For **a** and **b**, the statistical analysis is based on the one-way ANOVA and LSD (least significant difference) post-hoc comparison (two-sided). ***P < 0.001, ****P < 0.0001. In **a**–**b**, n = 3 independent samples and data are presented as mean ± SD.

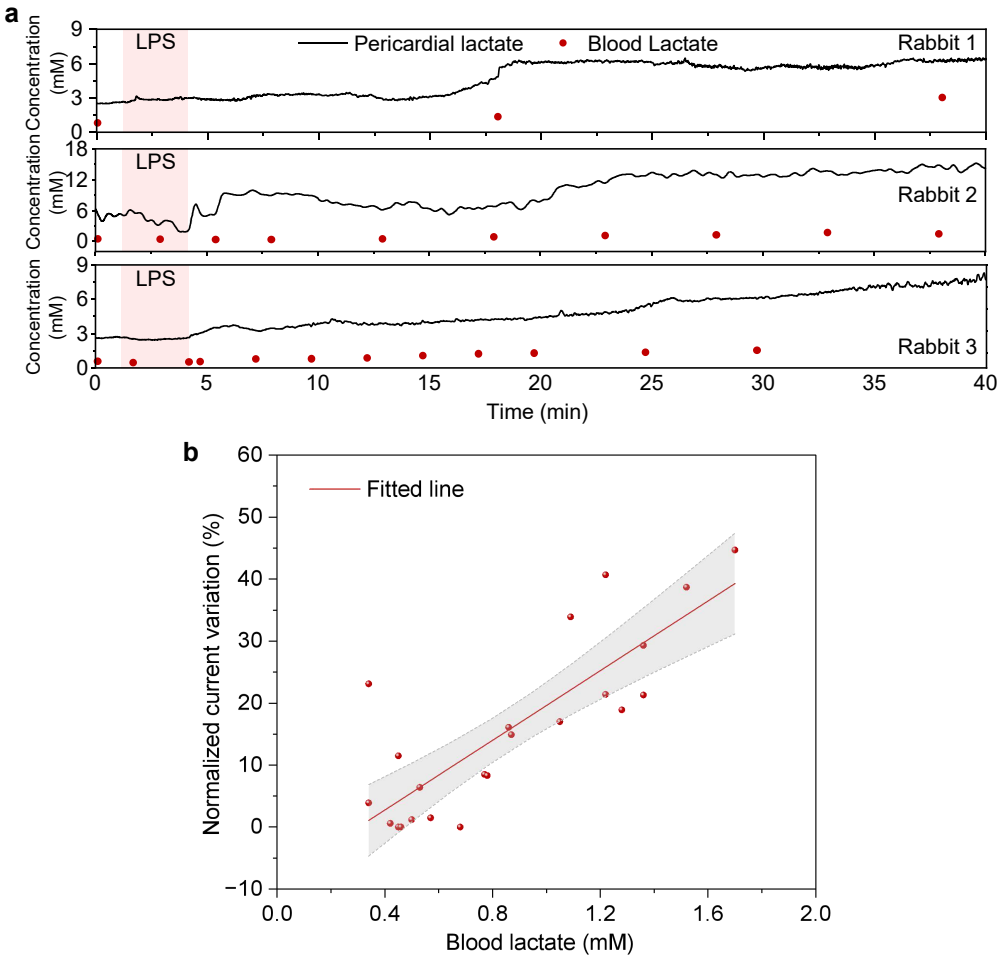


**Supplementary Fig. 40 | a**, Real-time monitoring of pericardial lactate of rabbits measured by the bioresorbable sensor, and corresponding sampled blood lactate from femoral artery during septic shock. The trace in Fig. 5b is included as Rabbit 1 to illustrate variability across animals. **b**, Correlation between the normalized current variation and blood lactate concentration from the rabbits. Pearson correlation coefficient, r = 0.82. The grey region within the dashed grey lines denotes the 95% confidence interval, and the fitted red line illustrates the linear trend. In **a** – **b**, n = 3 independent experiments.

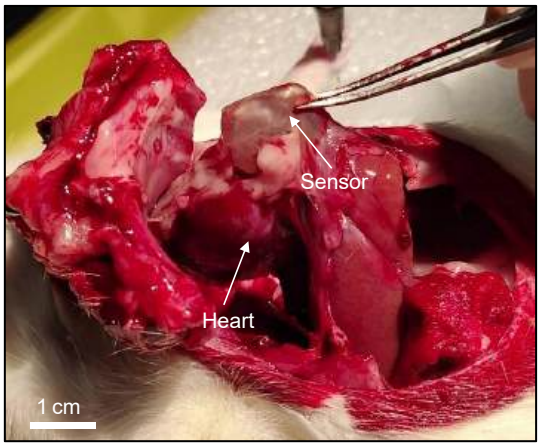


**Supplementary Fig. 41 | The lactate sensor remains adhered to the rat heart after 4 weeks of implantation.**

| Composition | Testing tissues | Lap shear strength | Biocompatibility | Biodegradability | Stability | Ref. |
|---|---|---|---|---|---|---|
| PEI/PAA | Chicken skin | 74.6 kPa | Low cytotoxicity | No | 12 h | 5 |
| PEGDA/TA | Porcine skin | 128.6 kPa | Yes | No | 5 days | 6 |
| Gelatin-Tea polyphenols-Urea | Porcine skin | 152.9 kPa | Yes | Yes | 14 days | 7 |
| P(AAm-*co*-MAEP-*co*-DMA) + P(AAM-*co*-APMA) | Bovine bone | 120 kPa | Low cytotoxicity | No | 4 months | 8 |
| PEGDA/peptide | Pig heart | 105.3 kPa | Yes | Yes | 6 months | This work |

**Supplementary Table 1 | Comparison of wet adhesion of hydrogel with biological tissues from previously reported work and the current work.**

| | Glucose (mM) | Uric acid (mM) | Urea (mM) | Ref. |
|---|---|---|---|---|
| Rabbit | 4.2–8.9 | 0.06–0.083 | 9.1–25.5 | 9 |
| Rat | 2.8–7.5 | - | - | 10 |
| Human | 4.1–5.9 | 0.24–0.51 (males)<br>0.16–0.43 (females) | 1.2–3 | 11 |

**Supplementary Table 2 | Representative concentration of glucose, uric acid and urea in physiological environments of healthy rabbits, rats, and adult humans.** Note: Ascorbic acid is not typically included among standard reference physiological indicators because of its relatively low blood concentration (<100 μM) and high stability.

| Working electrode | Sensing Layer | Counter electrode and reference electrode | Fabrication Method | Linear dynamic range | Detection limit | Sensitivity | Degradation | In vivo demonstration | In vivo testing period | Selectivity | Ref. |
|---|---|---|---|---|---|---|---|---|---|---|---|
| CFM | Pt/Nafion®-Lox/PU/M-PD | Two-electrode system (Ag/AgCl) | Electrodeposition/ Dip coating | 0.05–0.5 mM | 0.05 mM | 4.27 nA/mM | No | Status epilepticus | Short-term | AA, DA, UA | 12 |
| Pt wire | O-PD/PEG/BSA/ CHT-LOx-Pt-Ceria-$AO_x$ | Pt wire and Ag/AgCl | Electrodeposition/ Dip coating | 100 pM-15.5 mM 0.5-15.5 mM | 100 pM | 83.7 nA/mM | No | Brain hypoxia | 120 min | AA | 13 |
| Pt | CSA-$LO_x$ | Pt/Ag | Cross-linking/ Filling | 0–4 mM | - | 10 nA/mM | No | Atrium monitoring | 240 min | - | 14 |
| NiAu | CB-LDH/CA | Gold and Ag/AgCl | Drop-casting | 0.1–2 mM | 66 μM | 1.25 μA/mM | No | Ex vivo bone infection | 3 days | APAP | 15 |
| CNT fiber | NiCo-LDH | Two-electrode system (Ag/AgCl) | Drop-casting | 6–16 mM | - | 4.68 μA/mM | No | Intrauterine hypoxia | 7 days | Pyr, Glu, NaCl, KCl | 16 |
| Carbon Fiber | Pt/PPD/$LO_x$/ PU | Two-electrode system (Ag/AgCl) | PVD/ Electropolymerization | - | 1.16 μM | 0.20 nA /(μM·mm$^2$) | No | Mouse brain | ~80 min | 5-HT | 17 |
| CFM | PtNP-NPG/LOx/ Nafion/PU/m-PD | Pt wire and Ag/AgCl | Electrodeposition/ Dip coating/ Electropolymerization | 0-1 mM | 13 μM | 7.8 nA/mM | No | Mouse brain | Short-term | AA, DA, UA | 18 |
| gCPE | Pt/m-PD/$LO_x$ | Stainless steel and Ag/AgCl | Electrodeposition/ Dip coating | - | 19 μM | 2.63 nA/mM | No | Mouse brain | Short-term | - | 19 |
| Plastic Carbon Film | DH/MG-SWNT/BSA-LDH-$AO_x$ | Stainless steel and Ag/AgCl | Drop-casting | 50-1000 μM | 1 μM | 0.14 nA/mM | No | In vitro microdialysates | - | AA, DA, UA | 20 |
| Mo/Cr/ Au/AuNPs | PB/LOD/BSA/ glutaraldehyde /PU | Pt and Ag/AgCl | Sputtering/ Electrodeposition/Dip coating/Drop-casting | 0-20 mM | - | 0.025 μA/mM | Triggered dissolution and disintegration under overpotentials of 1.95-2.5 V | Rat kidney Ischemia | 80 min | Glu, UA, $CaCl_2$, VC, NaCl, KCl | 21 |
| **Mo/$MoO_x$** | **PVA/CS-LDH/$NAD^+$** | **Mo/$MoO_x$** | **Laser ablation/electro-anodization/drop casting** | **0.1–30 mM** | **0.1 mM** | **0.78 μA/mM** | **Complete biodegradation through dissolution and hydrolysis** | **Limb, brain, heart hypoxia Epilepsy Septic shock** | **11 days** | **$H^+$, AA, UA, Urea, Glu** | **This work** |

**Supplementary Table 3 | Comparison of the performance of implantable lactate sensors from the previously reported work and the current work**

| Distance | Received Signal Strength Indication | | Packet Loss Rate/10 |
|---|---|---|---|
| | Minimum | Maximum | |
| 0.5 m | -41 dB | -50 dB | 0 |
| 1.0 m | -78 dB | -54 dB | 0 |
| 2 m | -78 dB | -63 dB | 0 |
| 3 m | -78 dB | -63 dB | 0 |
| 5 m | -83 dB | -63 dB | 0 |
| 8 m | -83 dB | -76 dB | 1.86 |

**Supplementary Table 4 | Received signal strength indication (RSSI) and packet loss rate of the wireless module.**

1. Sheng, H. *et al.* A thin, deformable, high-performance supercapacitor implant that can be biodegraded and bioabsorbed within an animal body. *Sci. Adv.* **7** (2021).

2. Yang, X. *et al.* Hydrothermal synthesis of $MoO_3$ nanobelt-graphene composites. *Cryst. Res. Technol.* **46**, 1195-1201 (2011).

3. *NIST X-ray Photoelectron Spectroscopy Database,* https://srdata.nist.gov/xps/QueryByElmType/Mo/PE

4. Yuk, H. *et al.* Dry double-sided tape for adhesion of wet tissues and devices. *Nature* **575**, 169-174 (2019).

5. Peng, X. *et al.* Ultrafast self-gelling powder mediates robust wet adhesion to promote healing of gastrointestinal perforations. *Sci. Adv.* **7**, eabe8739 (2021).

6. Chen, K. *et al.* An all-in-one tannic acid-containing hydrogel adhesive with high toughness, notch insensitivity, self-healability, tailorable topography, and strong, instant, and on-demand underwater adhesion. *ACS Appl. Mater. Interfaces* **13**, 9748-9761 (2021).

7. Su, X. *et al.* Strong underwater adhesion of injectable hydrogels triggered by diffusion of small molecules. *Mater. Horiz.* **8**, 2199-2207 (2021).

8. Shao, H., Bachus, K. N. & Stewart, R. J. A water‐borne adhesive modeled after the sandcastle glue of P. californica. *Macromol. Biosci.* **9**, 464-471 (2009).

9. Van Praag E. Complete blood count and biochemistry reference values in rabbits. Medirabbit URL: http://www medirabbit com/EN/Hematology/blood_chemistry htm, 2023.

10. Grant K. A Layman's Guide to Health, Medication Use, Breeding, and Responsible Care of Pet Rats. Rat Guide URL: https://ratguidecom/health/basics-health/vital_statistics_in_ratsphp, 2003.

11. Farinde A. Lab values, normal adult: Laboratory reference ranges in healthy adults. URL: https://emedicine.medscape.com/article/2172316-overview. 2025.

12. Fernandes, E., Ledo, A., Gerhardt, G. A. & Barbosa, R. M. Amperometric bio-sensing of lactate and oxygen concurrently with local field potentials during status epilepticus. Talanta **268**, 125302 (2024).

13. Sardesai, N. P., Ganesana, M., Karimi, A., Leiter, J. C. & Andreescu, S. Platinum-doped ceria based biosensor for in vitro and in vivo monitoring of lactate during hypoxia. *Anal. Chem.* **87**, 2996-3003 (2015).

14. Baker, D. A. & Gough, D. A. A continuous, implantable lactate sensor. *Anal. Chem.* **67**, 1536-1540 (1995).

15. Gil, B. *et al.* Wireless implantable bioelectronics with a direct electron transfer lactate enzyme for detection of surgical site infection in orthopaedics. *Biosens. Bioelectron.* **263**, 116571 (2024).

16. Li, Q. *et al.* Interface‐Stabilized Fiber Sensor for Real‐Time Monitoring of Amniotic Fluid During Pregnancy. *Adv. Mater.* **36**, 2307726 (2024).

17. Chatard, C. et al. Minimally Invasive Microelectrode Biosensors Based on Platinized Carbon Fibers for in Vivo Brain Monitoring. ACS Cent. Sci. 4, 1751-1760 (2018).

18. Regiart M, et al. Highly sensitive and selective nanostructured microbiosensors for glucose and lactate simultaneous measurements in blood serum and in vivo in brain tissue. Biosens. Bioelectron. 199, 113874 (2022).

19. Booth, MA. et al. Fiber-Based Electrochemical Biosensors for Monitoring pH and Transient Neurometabolic Lactate. Anal. Chem. 93, 6646-6655 (2021).

20. Lin, Y. et al. Physiologically relevant online electrochemical method for continuous and simultaneous monitoring of striatum glucose and lactate following global cerebral ischemia/reperfusion. Anal. Chem. 81, 2067-2074 (2009).

21. Li, X. et al. A programmable bioresorbable electrochemical microneedle sensor array for perioperative monitoring of organ health. Nat. Biomed. Eng. 1-18 (2026).

## Description of Additional Supplementary File

**Supplementary Movie 1**

Long-term adhesion of PEGDA/peptide hydrogel on porcine intestine over 6-month. The blue color results from spontaneous reaction of genipin with amino groups and serves as an indicator of crosslinking.

**Supplementary Movie 2**

Sealing of a perforated porcine stomach with PEGDA/peptide hydrogel.